More Powerful Twistron Carbon Nanotube Yarn Mechanical Energy Harvesters

*Zhong Wang, Tae Jin Mun, Fernando M. Machado, Ji Hwan Moon, Shaoli Fang,
Ali E. Aliev, Mengmeng Zhang, Wenting Cai, Jiuke Mu, Jae Sang Hyeon, Jong Woo Park,
Patrick Conlin, Kyeongjae Cho, Enlai Gao, Gang Wan, Chi Huynh, Anvar A. Zakhidov,
Seon Jeong Kim,* and Ray H. Baughman**

Stretching a coiled carbon nanotube (CNT) yarn can provide large, reversible electrochemical capacitance changes, which convert mechanical energy to electricity. Here, it is shown that the performance of these "twistron" harvesters can be increased by optimizing the alignment of precursor CNT forests, plastically stretching the precursor twisted yarn, applying much higher tensile loads during precoiling twist than for coiling, using electrothermal pulse annealing under tension, and incorporating reduced graphene oxide nanoplates. The peak output power for a 1 and a 30 Hz sinusoidal deformation are 0.73 and 3.19 kW kg^{-1}, respectively, which are 24- and 13-fold that of previous twistron harvesters at these respective frequencies. This performance at 30 Hz is over 12-fold that of other prior-art mechanical energy harvesters for frequencies between 0.1 and 600 Hz. The maximum energy conversion efficiency is 7.2-fold that for previous twistrons. Twistron anode and cathode yarn arrays are stretched 180° out-of-phase by locating them in the negative and positive compressibility directions of hinged wine-rack frames, thereby doubling the output voltage and reducing the input mechanical energy.

1. Introduction

Improved means for converting mechanical energy to electricity are needed for diverse applications, from harvesting ocean wave energy to power cities to using body motion to power sensors and energy-storage devices in and on the human body.[1–6] Recently described coiled carbon nanotube (CNT) yarns, called twistrons,[7] use stretch-induced changes in electrochemical capacitance to generate higher peak electrical power per harvester weight than generated by any prior-art mechanical energy harvester for mechanical frequencies between 6 and 600 Hz.

The electrochemical capacitance changes that produce electricity result from mechanically generated changes in yarn twist. Increasing yarn twist increases yarn density, compressing and partially eliminating the electrochemical double

Z. Wang, F. M. Machado, S. Fang, A. E. Aliev, M. Zhang, W. Cai, J. Mu,
A. A. Zakhidov, R. H. Baughman
Alan G. MacDiarmid NanoTech Institute
University of Texas at Dallas
Richardson, TX 75080, USA
E-mail: ray.baughman@utdallas.edu
T. J. Mun, J. H. Moon, J. S. Hyeon, J. W. Park, S. J. Kim
Center for Self-Powered Actuation
Department of Biomedical Engineering
Hanyang University
Seoul 04763, South Korea
E-mail: sjk@hanyang.ac.kr
F. M. Machado
Technology Development Center
Federal University of Pelotas
Pelotas, RS 96010-610, Brazil

W. Cai
School of Chemistry
Xi'an Jiaotong University
Xi'an, Shaanxi 710049, China
P. Conlin, K. Cho
Department of Materials Science and Engineering
University of Texas at Dallas
Richardson, TX 75080, USA
E. Gao
Department of Engineering Mechanics
School of Civil Engineering
Wuhan University
Wuhan, Hubei 430072, China
G. Wan
Department of Mechanical Engineering
Stanford University
Stanford, CA 94305, USA
C. Huynh
Nano-Science and Technology Center
Lintec of America
Richardson, TX 75081, USA

**ADVANCED
SCIENCE NEWS**

www.advancedsciencenews.com

**ADVANCED
MATERIALS**

www.advmat.de

layers of CNTs, and twist release reverses this. These twist changes result from either twisting a noncoiled CNT yarn or stretching a torsionally tethered coiled yarn, thereby reversibly converting the twist of coiling to yarn twist. While high-performance non-electrochemical capacitance-based dielectric harvesters typically use thousand-volt-scale applied voltages,[8–10] twistrons can harvest without an externally applied bias voltage,[7] since the used electrolytes inject either electrons or holes into the CNTs. Such self-biasing was deployed for self-powered strain sensors that generate a voltage between opposite ends of a stretched coiled CNT yarn.[11]

We here report various new methods for dramatically increasing twistron harvesting, which are primarily based on increasing mechanically induced changes in electrochemical capacitance. These improvements were achieved by incorporating conducting nanosheets in twistron yarn corridors, optimizing the alignment of precursor CNT forests, plastically stretching the precursor twisted yarn, applying much higher tensile loads during pre-coiling twist than for coiling, and using our incandescent tension anneal process (ITAP) for electrothermal pulse annealing under tension. In our previous work on using ITAP to improve the mechanical properties of twisted and coiled CNT yarns, we found that the strength and modulus were both optimized when high twist densities were inserted and a very high tensile stress (≈200 MPa) was applied during ITAP.[12] In contrast, we presently find that harvester performance is optimized when ITAP was applied to a low twist yarn (with a bias angle of about 22°) when the yarn was under a relatively low tensile stress (34 MPa).

Using these improvements, the energy conversion efficiency of twistrons was increased over 7-fold and the peak power output reached values that are 12-fold those reported for previous materials-based technologies for key frequency ranges. These powerful twistrons were integrated into hinged wine-rack frames and Scotch yokes to harvest tensile and torsional mechanical energy and used as self-powered strain sensors for recognizing sign language.

2. Results and Discussion

2.1. Harvester Fabrication

In our cone spinning process,[7] highly elastic fully coiled yarn harvesters were obtained by inserting extreme twist into cylindrically configured forest-drawn CNT sheets[13,14] while they were under tensile load (**Figure 1**a). These coiled yarns were untwisted by 8% of the total inserted twist,[7] which reduces twist-induced densification without causing coil loss, thereby improving harvesting by increasing the electrochemically accessible area and the reversible tensile strain range. Yarns that are twisted and not coiled and both twisted and coiled are called twisted yarns and coiled yarns, respectively.

Unless otherwise described for isobaric self-coiling, the twisted yarn's diameter before coiling onset was 60–90 µm, the stress applied during twist insertion was about 30 MPa (when normalized to the yarn's cross-sectional area immediately before coiling onset), and the coiled yarn's spring index was

about 0.45. A typical harvester characterization used a coiled twistron working electrode, a high-capacitance CNT-sheet-wrapped Pt mesh counter electrode, and an Ag/AgCl reference electrode (Figure 1a, right). The electrolyte was 0.1 M aqueous HCl and the applied strain was sinusoidal, unless otherwise noted.

2.2. Optimizing Harvesting by Using Forest Selection to Tune CNT Alignment

Since increasing the density of active catalyst particles on the growth substrate increases forest density, which typically increases CNT alignment in a forest[15,16] and in forest-derived sheets and yarns, the CNT alignment that optimizes twistron performance was obtained by tuning catalyst density. Additionally, twisted yarns were mechanically stretched to provide plastic deformation that increases CNT alignment. CNT alignment was quantified by the Herman's orientation factor (HOF), which was obtained from fast Fourier transforms of scanning electron microscopy images of CNT sheets[17] (Figures S1 and S2, Supporting Information). The HOF ranged from about 0.49–0.75 for sheets drawn from high-density forests (Figure 1c), where HOFs of 0 and 1 correspond to random and perfect orientation, respectively. Figure 1b shows the large change in open-circuit potential (OCP vs Ag/AgCl) and short-circuit current (SCC) that results from sinusoidally stretching (by 35% at 1 Hz) a coiled twistron made from a sheet having a high orientation factor (0.64).

The peak OCV, peak power, and energy per cycle for coiled twistrons initially increase with increasing HOF, reach approximate plateaus for a HOF between 0.62 and 0.68, and decrease for further HOF increase (Figure 1c). A peak OCV, peak power, and energy per cycle of 274 mV, 210 W kg^{-1}, and 65 J kg^{-1} were achieved for a twistron made from a sheet with a HOF of 0.64. The large initial increase in harvester performance with increasing HOF arises because the electrochemical double-layers of poorly aligned CNTs interact over the small regions where CNT bundles intersect and these capacitance-changing areas increase with increasing CNT alignment[18] (Figure S3, Supporting Information). Further increasing forest density, which yields forest-drawn sheets with a HOF above 0.7, decreases energy harvesting due to the large bundle diameters resulting from very high CNT alignment, and correspondingly decreased gravimetric surface area and capacitance. The above peak power and output energy per cycle at 1 Hz for an optimally aligned twistron are 5.1 and 5.4 times, respectively, the values previously reported for sinusoidal stretch of a twistron harvester at 1 Hz.[7]

This performance increase, by optimizing the alignment of the precursor CNT sheets, is also evident in energy harvesting by isometric twist insertion and removal from noncoiled CNT yarns (Figures S4–S6, Supporting Information). Figure 1d shows the dependence of the OCP and capacitance on inserted twist for a twisted yarn fabricated from a highly aligned sheet, with a HOF of 0.64. Increasing bundle alignment from 0.52 to 0.64 increases twist-induced decreases in capacitance and yarn resistance (Figure 1e), which increases the peak OCV and the harvested energy.
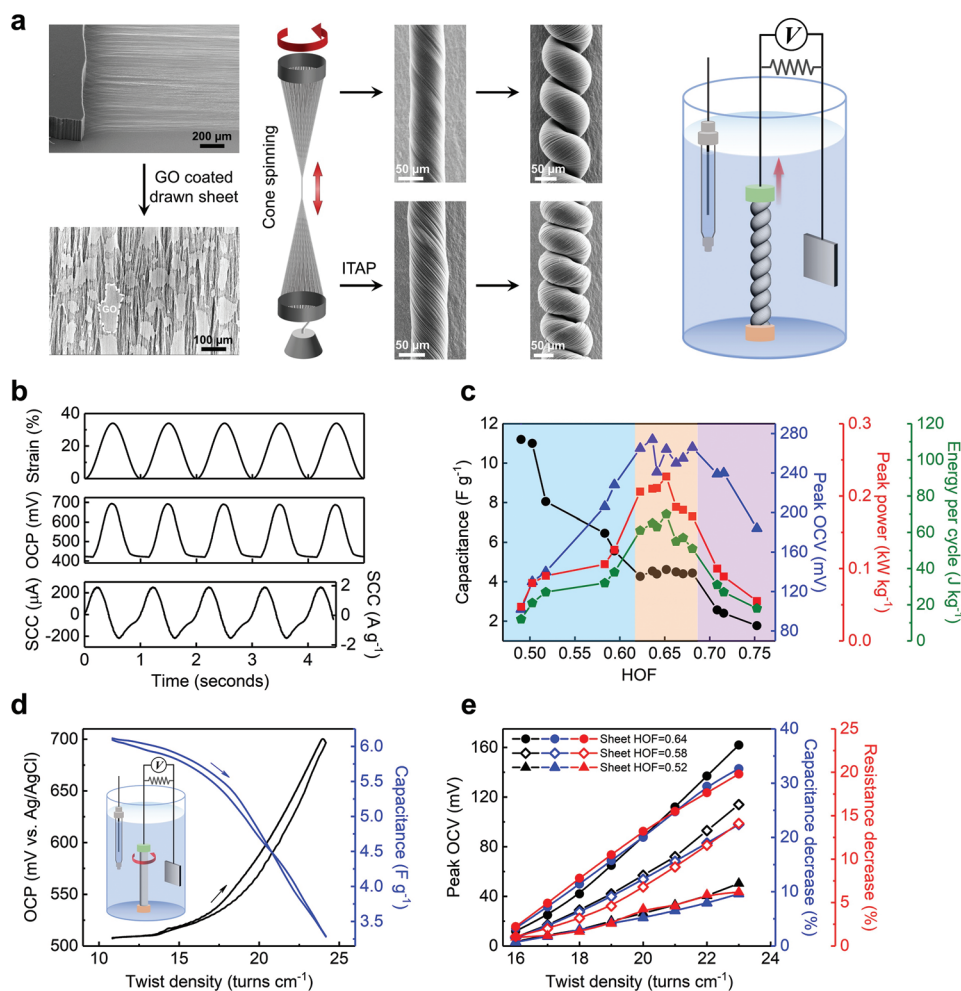
Figure 1. Twistron fabrication, structure, and characterization, and the effects of CNT orientation on energy harvesting in 0.1 M aqueous HCl by using a 1 Hz, 35% sinusoidal stretch. a) SEM images and illustration of cone spinning for fabricating twisted and coiled neat CNT yarns from forest-drawn CNT sheets (top), and its modification for making rGO@CNT yarns (bottom). (Right) Illustration of the electrochemical cell used for characterizing coiled harvester yarns. b) The time dependencies of applied tensile strain and resulting changes in open-circuit potential (OCP vs Ag/AgCl reference) and short-circuit current (SCC) for a coiled harvester. c) The dependencies of the pre-stretch capacitance, peak OCV, and peak electrical power of coiled CNT twistrons on the HOF of the precursor forest-drawn CNT sheets. d) For a noncoiled, 30 mm long, 100 μm diameter CNT yarn being twisted and untwisted at 3.33 turn cm^{-1} s^{-1}, the dependencies of the capacitance and OCP on isometric twist and untwist. (Inset) Experimental apparatus. e) The peak OCV and percent capacitance and resistance decreases (relative to their values at 12 turns cm^{-1}) as a function of twist density during isometric twist for noncoiled yarns made from CNT sheets having different values of HOF. A precursor CNT sheet with a HOF of 0.64 was used for (b) and (d).

Irreversibly stretching the twisted yarn prior to isobaric coiling increases harvester performance to above that obtained by optimally aligning the precursor forest (**Figure 2**a,b). By keeping the precursor twisted yarn at an applied tensile strain until the applied force becomes constant, the degree of irreversible stretch was measured for each applied strain (Figure 2a). With increasing applied strain up to close to the fracture strain of 4.25% (Figure S7a, Supporting Information), the HOF of the twisted yarn and the harvester performance of the coiled yarn monotonically increased, while the coiled yarn's capacitance was little effected (Figure 2a inset). The 2.74% irreversible stretch of the precursor twisted yarn increased the reversible peak OCV, peak power, and harvested energy per cycle of the coiled yarn by factors of 1.3, 1.7, and 1.6, respectively, during 1 Hz harvesting to 35% strain. Figure 2b shows the frequency

dependence of the enhanced performance resulting from this plastic deformation of the precursor yarn.

2.3. Increasing Harvesting by the Incandescence Tension Anneal Process (ITAP)

Harvesting was increased by our incandescence tension anneal process (ITAP), wherein an electric pulse heats in vacuum a mechanically loaded, torsionally tethered, twisted yarn[12] (Figure 2c). For the below use of ITAP at ≈3000 °C, the precursor CNT sheets had a HOF of 0.59. Figure S9 (Supporting Information) micrographs show structural evolution as a function of electric pulse time for a twisted yarn (with a bias angle of 22°) that was twist inserted and ITAP treated under 34 MPa stress. CNT

**ADVANCED
SCIENCE NEWS**

www.advancedsciencenews.com

**ADVANCED
MATERIALS**

www.advmat.de
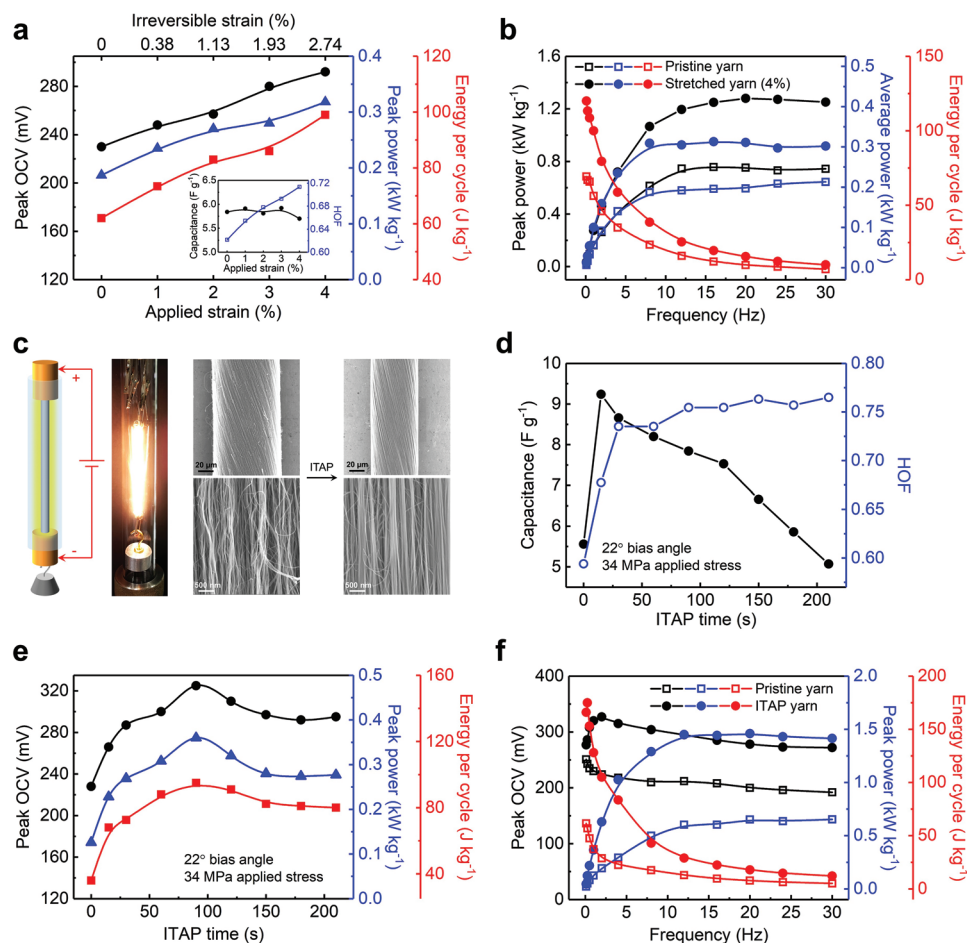
Figure 2. Using irreversible stretch and ITAP for increasing harvesting in 0.1 M aqueous HCl. a) The dependencies of peak OCV, peak power, and energy per cycle for a 1 Hz, 35% stretch of coiled twistrons on the applied strain and the strain of irreversible stretch for the precursor twisted yarn. Inset: The dependencies of coiled yarn capacitance and the surface HOF for twisted yarns on the applied strain resulting in irreversible stretch. b) The frequency dependencies of peak power, average power and energy per cycle for coiled twistron harvesters undergoing the above stretch, before and after using a 4% applied strain to provide irreversible stretch of the precursor twisted yarn. c) (Left) Illustration and photograph of a CNT yarn during ITAP. (Right) SEM images of a CNT yarn before and after ITAP. d) The dependence of coiled yarn capacitance and the surface HOF of precursor twisted yarn on ITAP time. e,f) The dependencies of peak OCV, peak power, and energy per cycle of coiled twistrons for a 45% stretch on e) ITAP time (for a 1 Hz stretch) and f) stretch frequency (before and after a 90 s ITAP).

alignment and bundle size increase after ITAP (Figure 2c and Figure S9, Supporting Information). The yarn's HOF abruptly increased from 0.59 to 0.74 during 30 s of ITAP, and then gradually increased to 0.77 over the next 180 s of ITAP (Figure 2d). The capacitance of the coiled twistron yarns increased from 5.56 to 9.24 F g^{-1} after 15 s of ITAP and then decreased with further increased ITAP time, likely because of CNT bundling increases and CNT welding (Figure S13, Supporting Information). The ITAP was most usefully deployed for twisted yarn with a bias angle of about 22°, rather than for highly twisted or coiled yarns. This is because ITAP partially freezes the ability of highly twisted or coiled yarns to untwist,[12] likely because of ITAP-produced welding between nanotubes, which also decreases ITAP-produced CNT orientation for the highly twisted yarn.

Figure 2e shows the dependence of coiled yarn harvesting on ITAP time for the precursor twisted yarns. Insertion of the ITAP (annealing at ≈3000 °C for 90 s under 34 MPa) increased the peak OCV, peak power and energy per cycle for a 1 Hz stretch

from 228 mV, 126 W kg^{-1}, and 36 J kg^{-1} to 325 mV, 360 W kg^{-1}, and 95 J kg^{-1}. These peak power and energy per cycle are 8.7 and 7.9 times, respectively, values reported at this frequency for previous twistron yarns.[7] For a 12 Hz stretch, the peak power and average power increased from 604 and 156 W kg^{-1}, respectively, for the pristine yarn to 1451 and 348 W kg^{-1}, respectively, for the ITAP yarn, and plateaued with further frequency increase (Figure 2f and Figure S8, Supporting Information).

2.4. Performance Increases by Varying the Tensile Stress During Twistron Fabrication

Since high-work-capacity artificial muscles were previously made by both twisting and coiling under the same tensile load,[19,20] this method was previously used to make self-coiled twistrons. However, we now discovered that the tensile load during twist insertion should be much higher than the 35 MPa

previously used for making twistrons[7] and the load applied during subsequent coiling should be much lower than 35 MPa (Figures S14 and S17, Supporting Information). We call this new fabrication method the "tension optimization process" (TOP).

Figures S15 and S16 (Supporting Information) show the major performance increases resulting from the high stress applied during the precoiling TOP process for energy harvesting by twistrons coiled at low stress. These results show that the peak and average power increase with increasing load during twist insertion until the twist-increased value of yarn HOF exceeds 0.69. This is similar to the performance advantage (Figures 1c and 2a, and Figure S10, Supporting Information) resulting from increasing orientation by using precursor forest-drawn sheets having a high HOF and by introducing stretch-induced alignment for a low-twist precursor yarn.

The peak and average power at 1 Hz reached 305 and 75 W kg^{-1} (Figure S15b, Supporting Information), respectively, compared with 80 and 22 W kg^{-1}, respectively, at this frequency for an isobarically prepared twistron.[7] For frequencies above 10 Hz, a Pt-wire-wrapped TOP twistron provided plateau values of peak power and average power of 1350 and 318 W kg^{-1}, respectively (Figure S15e, Supporting Information). The maximum energy per cycle was 280 J kg^{-1} at 0.1 Hz, which provided an energy conversion efficiency of 4.66% for a total strain of 58% (Figure S18, Supporting Information). For comparison, the maximum efficiency for twist insertion and removal from a fully coiled TOP yarn was 4.89% (Figure S19, Supporting Information). The peak and average power (157 and 52 W kg^{-1}) of the TOP twistron were maintained for over 30 000 cycles to 60% total strain at 1 Hz (Figure S15f, Supporting Information).

2.5. The Performance Advantage of Biscrolled rGO@CNT Harvesters

Harvesting was greatly increased by putting high surface area, conducting nanoplates between neighboring CNT yarn layers by biscrolling.[21] This improved performance results from the dramatically increased interactions between 1D nanotube bundles and 2D nanosheets compared with those between nanotube bundles, which increased the capacitance change from 54% for an ITAP-treated CNT twistron to 65% for an ITAP-treated rGO@CNT twistron. This guest was deposited on the upper surface of each CNT sheet, and trapped between CNT yarn layers when a stack of sheets was cone spun. Since large diameter graphene oxide (GO) platelets (10–25 µm) are easily dispersed in water[22,23] and spray coated on individual CNT sheets, and later converted to reduced graphene oxide (rGO), they were used to make about 80 µm diameter biscrolled rGO@CNT yarns (Figure 1a and Figure S25, Supporting Information).

Twist was inserted into the GO-coated CNT sheet stack until a low twist-density GO@CNT yarn (with a bias angle of about 22°) was produced. ITAP (30 s at ≈3000 °C) was then applied to convert these GO@CNT yarns to rGO@CNT yarns (Figure S20, Supporting Information). X-ray diffraction results indicate this reduction, since the long interlayer spacing due to reacted oxygen disappears after ITAP (Figure 3b and Figure S24, Supporting Information). These results also show that the GO platelets in a pre-ITAP yarn and the rGO platelets in a post-ITAP

yarn are oriented parallel to the yarn axis and that these platelets increased the average separation between neighboring CNTs in a bundle from 8.07 to 8.38 nm (**Figure 3**a,b).

The harvesting of a coiled biscrolled rGO@CNT twistron was optimized when the amount of rGO was 29 wt%. A 48%, 1 Hz stretch produced a peak OCV of 380 mV, a peak power of 363 W kg^{-1}, and an energy per cycle of 112 J kg^{-1} (Figure 3c and Figure S22, Supporting Information). This OCV is 2 times the previous record for a twistron.[7] Upon increasing the HOF of the CNT sheet used for biscrolling from 0.54 to 0.59, the peak power and energy per cycle for a 45%, 1 Hz stretch was further increased to 545 W kg^{-1} and 182 J kg^{-1}, although the peak OCV decreased to 346 mV. This peak power and energy per cycle are over 10 times values previously reported at 1 Hz for a twistron (Figure 3d). Reduction of GO to rGO in the biscrolled yarn is essential for this remarkable performance. Without reduction, the coiled GO@CNT has only a peak OCV of 45 mV and a peak power of 7.4 W kg^{-1} during a 45%, 1 Hz stretch, which is 1.6% of that for the rGO@CNT twistron.

The frequency dependencies of peak power, average power and energy per cycle are shown in Figure 3d for this 29 wt% rGO@CNT twistron. With frequency increase, the peak power increased to 2.07 kW kg^{-1} at 16 Hz and then plateaued. The plateau in peak power, as well as average power, provides a major advantage over low-strain resonant harvesters, such as piezoelectrics, whose output power drastically decreases if the vibration frequency slightly differs from the resonance frequency.[24] Coiling a 25 µm diameter Pt wire with a 29 wt% rGO@CNT twistron increased the maximum peak power and energy per cycle to 3.22 kW kg^{-1} and 304 J kg^{-1}, when ignoring the Pt wire's weight (Figure 3d and Figures S26 and S27, Supporting Information). This wire increased the average output electrical power for a 16 Hz sinusoidal deformation from 0.58 to 0.85 kW kg^{-1}. Hence, 2 mg of a twistron yarn harvester would provide the power needed[25] to transmit a 2 kB packet of data over a 100 m radius every 10 s for the Internet of Things. The peak power and average power (184 and 71 W kg^{-1}) of a rGO@CNT twistron were largely maintained for 10 000 cycles to 27% strain at 1 Hz in 0.1 M HCl (Figure S23, Supporting Information).

Figure 3e,f and Table S1 (Supporting Information) compare the peak power output and peak power output divided by frequency for thereby improved twistrons with the performance of previously investigated mechanical energy harvesters of all types. For deformation frequencies between 0.1 and 600 Hz, the peak power and frequency-normalized peak power of our twistron harvester are higher than for any other material-based mechanical energy harvesting technologies. The peak power at 2 Hz and at 30 Hz were 1.05 and 3.19 kW kg^{-1}, respectively. This peak power at 30 Hz was over 12-fold that of other prior-art mechanical energy harvesters for frequencies between 0.1 and 600 Hz. As shown by the results of Table S2 (Supporting Information), the twistron harvesters provide a higher average gravimetric power output than for any other self-powered harvester. While dielectric elastomer harvesters in this table provide a higher average output power for frequencies at or below 0.54 Hz than do our twistrons, this low frequency advantage of the dielectric elastomer harvesters will likely disappear when the weight of the power source needed to generate their thousand-volt or higher bias voltage is included in the harvester's
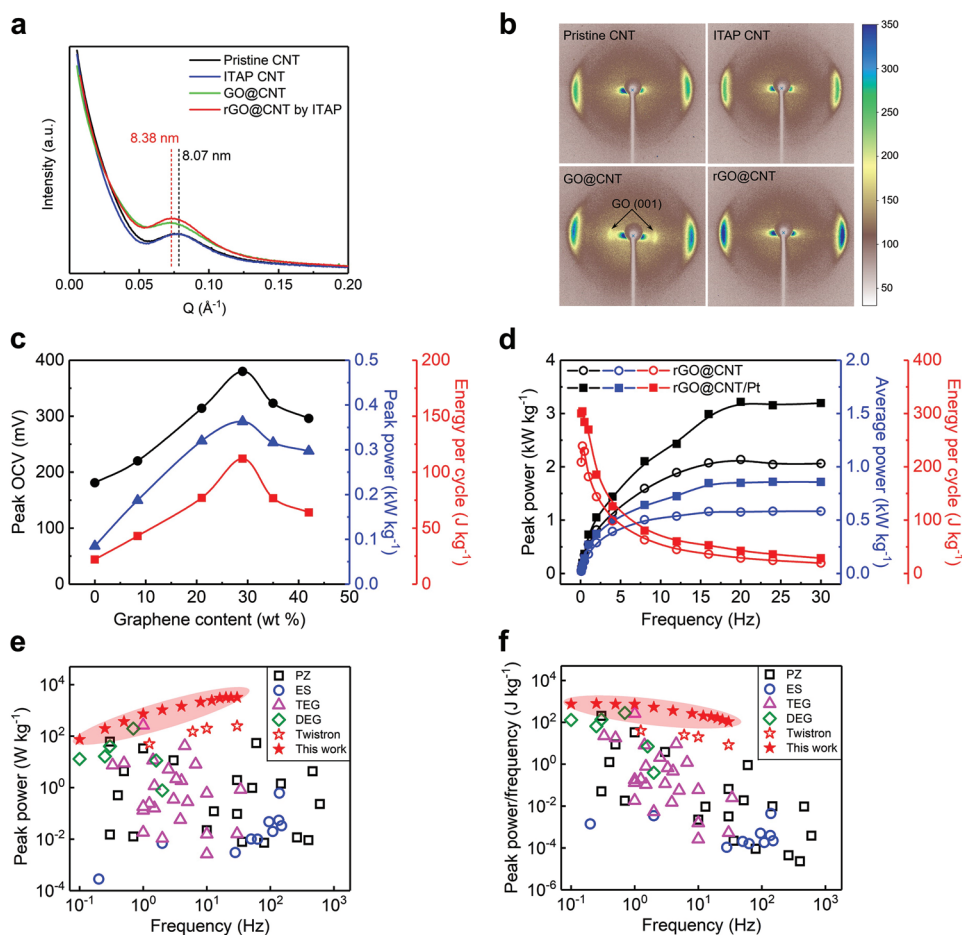
Figure 3. Harvesting by a biscrolled coiled rGO@CNT twistron in 0.1 M aqueous HCl. a) The small-angle X-ray scattering intensity as a function of scattering vector and b) the 2D wide-angle X-ray scattering patterns for the twisted pristine yarn, 30 s ITAP-treated CNT yarn, GO@CNT yarn, and 30 s ITAP-treated rGO@CNT yarn. The diffraction peak corresponding to the interlayer separation in GO is marked by arrows in (b). Due to the difficulty in precisely aligning the direction of the twistron with respect to the X-ray beam, there is no meaning to the deviation between equatorial and horizontal directions for images in (b). c) The dependencies of peak OCV, peak power, and energy per cycle on graphene content for a 1 Hz, 45% stretch of rGO@CNT harvesters. d) The frequency dependencies of peak power, average power and energy per cycle before and after including a Pt wire current collector. e) Peak power and f) frequency-normalized peak power versus frequency for present twistrons and prior-art twistrons, piezoelectric (PZ), electrostatic (ES), triboelectric (TEG), and dielectric elastomer (DEG) electricity generators.

weight. This record performance at low frequencies requires biaxial stretching of the dielectric elastomer harvesters, which provides additional complexity and weight.

The rGO@CNT twistron yarns can generate an intrinsic bias voltage of ≈0.6 V (the difference between the OCP and the pzc at 0% strain) in 0.1 M HCl because of charge injection from the electrolyte[7] (Figures S11, S12, and S21, Supporting Information). For a sinusoidal stretch of 46% at 0.25 Hz, applying an external bias voltage of 0.4 V increased the net energy harvested per cycle from 140 to 285 J kg^{-1} (Figure S28, Supporting Information). Further bias voltage increase decreased the net energy harvested, due to increased electrolytic losses. Since an electrolyte of 0.1 M LiBF$_4$ in acetonitrile has lower electrolytic losses, the bias voltage that optimized the net energy harvested could be increased to 0.6 V (Figures S38 and S39, Supporting Information). Cycling of a rGO@CNT twistron yarn at 0.25 Hz to 48% strain in 0.1 M HCl resulted in an energy conversion efficiency of 3.89% (Figures S29 and S30, Supporting Information). Applying a 0.4 V bias voltage increased

this efficiency to 4.85% (Figure S31, Supporting Information), compared to 1.05% for the previously reported CNT twistron harvesters.[7] Further optimization is possible without using a bias voltage, since Figure S32 (Supporting Information) shows that the energy conversion efficiency for a 7.5%, 0.25 Hz sinusoidal cycle increases with increasing initial strain until this strain exceeds 15%. A higher energy conversion efficiency was obtained for twist insertion and removal from a noncoiled, twisted rGO@CNT twistron (7.6%) when no bias voltage was applied (Figure S33, Supporting Information).

2.6. Performance Increases by Tuning the Tensile Strain Profile During a Mechanical Cycle and the Time Between Successive Mechanical Energy Pulses

Since the shape of the strain-versus-time curve during a mechanical energy delivery cycle and the cycle frequency can be mechanically transformed, we wondered what strain

**ADVANCED
SCIENCE NEWS**

www.advancedsciencenews.com

**ADVANCED
MATERIALS**

www.advmat.de

profile would optimize energy harvesting. For both TOP (Figures S41b, S42, and S43, Supporting Information) and rGO@CNT twistrons (Figure S44d, Supporting Information), we found that a square-wave strain provides a higher peak and average electrical power output than a sinusoidal strain for deformation frequencies between 0.2 and 4 Hz. The maximum ratio of harvested energy per cycle for the square wave to that for the sinusoidal wave is at the same frequency (1 Hz) and has nearly the same value for the TOP twistron (2.1) and the rGO@CNT twistron (1.7). At higher frequencies, both deformations provide nearly the same harvested energy per cycle, because this is partially determined by internal deformation times of the twistron, such as those for the extrusion and reabsorption of electrolyte. Figure S41e (Supporting Information) shows the powering of a 100 mW green light-emitting diode by one square-wave 0.2 Hz stretch of a TOP twistron weighing only 1.04 mg, which is possible because the peak power for the square wave is 9.7 times that for the sinusoidal wave at this frequency (Figure S41b, Supporting Information).

For many applications, there will be time delays between successive mechanical deformations, and latches can be used to temporarily maintain stretched states. We next show that harvesting during these time delays can increase the energy harvested from mechanical energy pulses, as well as the efficiency of mechanical energy harvesting (Figure S34, Supporting Information). Figure S35a (Supporting Information) shows that the electrical energy per cycle during continuous sinusoidal deformation dramatically decreases with increasing frequency for a rGO@CNT twistron. However, the total harvested energy per cycle increases and becomes essentially frequency independent for frequencies up to 20 Hz when sinusoidal stretch and stretch release are separated by 2 s intervals (Figure S35b, Supporting Information), during which harvesting occurs but no external mechanical deformation. By including this extra 2 s of energy harvesting for a Pt-wire-wrapped rGO@CNT twistron, the energy conversion efficiency at 0.1 and 0.25 Hz increased from 5.3% and 5.5% to 6.4% and 7.6% (Figures S36 and S37, Supporting Information). Allowing this extra time enables structural relaxation that enhances harvesting. The need for this extra harvesting time is most clearly seen by noticing that the twistron buckles during high-frequency stretch-release, rather than merely contracting.

2.7. Application Demonstrations

For potential use of these improved twistrons for harvesting ocean wave energy,[26] rGO@CNT twistrons were tested in 0.6 M aqueous NaCl, a typical seawater concentration. A 725 W kg^{-1} plateau in peak power was observed for a 46% sinusoidal deformation above 12 Hz (**Figure 4**a). Harvesting was little changed for temperatures from 0 to 60 °C (Figure S40, Supporting Information), which is important for use in varying temperature oceans. Figure 4b shows the power output of a 400-µg rGO@CNT ocean-wave harvester for a simulated wave frequency of ≈0.8 Hz that provided 20% to 30% stretch in 0.6 M NaCl. This rGO@CNT harvester generated an average output power of 11.8 W kg^{-1}, which was 7.1 times that obtained in the ocean for our previous twistron harvester[7] for about the

same strain (25%) and frequency (0.9–1.2 Hz). Operating in the ocean, our TOP twistron provided an average output power of 10.7 W kg^{-1} for ocean wave frequencies between 0.5 and 1 Hz when the tensile deformation was mechanically limited to below 50% (Figure S52c, Supporting Information).

It is useful for many applications to eliminate the weight, volume, and cost of a nonharvesting electrode, as well as to fully utilize the recoverable part of the mechanical energy that is introduced into twistrons during stretch. We found that identical twistron yarns can be linearly configured as anode and cathode to provide about the same average output electrical power per total twistron weight at all frequencies as a single twistron harvester, thereby eliminating the need for a nonharvesting counter electrode. This was demonstrated by using our rGO@CNT (Figure S53, Supporting Information) and TOP twistrons (Figures S49 and S50, Supporting Information) in a seesaw configuration, in which identical, mechanically connected, torsionally tethered anode and cathode twistrons are deformed 180° out-of-phase by axially translating the mechanical junction between these twistrons. Since the initially inserted strain energy in one twistron is released as the strain energy in the other twistron is increased, the mechanical energy input is correspondingly decreased. Since both electrodes provide opposite potential changes, the peak-to-peak open circuit voltage was doubled to 0.59 V by using the seesaw, although the short-circuit current was little changed (Figure S53, Supporting Information).

To realize the benefits of the seesaw structure, while reducing interelectrode diffusion distances and enabling upscaling, opposing twistron electrodes were located in the negative and positive linear compressibility directions[27,28] of hinged wine-rack frames (Figure 4e and Figure S52d inset, Supporting Information). Ten 1.7 cm long twistrons, each weighting 80 µg, were placed parallel in the negative and positive compressibility directions of four wine-rack cells (Figure 4c,d). During harvesting, the structure morphs between two equivalent structures (Figure 4e), in which the twistrons in the short and long diagonal directions are simultaneously stretched and stretch-release, respectively. Each wine-rack cell provided a peak OCV of 306 mV and SCC of 1.97 mA, and a peak and average power of 76 and 23 W kg^{-1} when stretched 35% at 1 Hz. When the four cells were connected in series and in parallel, the output OCV and SCC increased to 1.09 V and 7.31 mA (Figure S52d, Supporting Information), even though the total twistron weight was only 6.4 mg. Since rotary mechanical energy is available from wind or water turbines, and our highest electrical power densities are for tensile harvesters, we also demonstrated twistron harvesters that use Scotch yokes[29] to scalably convert input rotational energy to tensile energy (Figure S51, Supporting Information).

Since eliminating the electrolyte bath is important for many applications, we devised a new type of solid-state twistron harvester, in which a solid-electrolyte-coated twisted CNT yarn is coiled around a solid-electrolyte-coated homochiral yarn (Figure 4f inset). In-phase stretch of the anode and cathode twistrons usefully generates 180° out-of-phase voltages, since one twistron is homochiral and the other is heterochiral (Figure S45, Supporting Information). The resulting solid-state harvester generated a peak OCV of 188 mV when stretched 38%
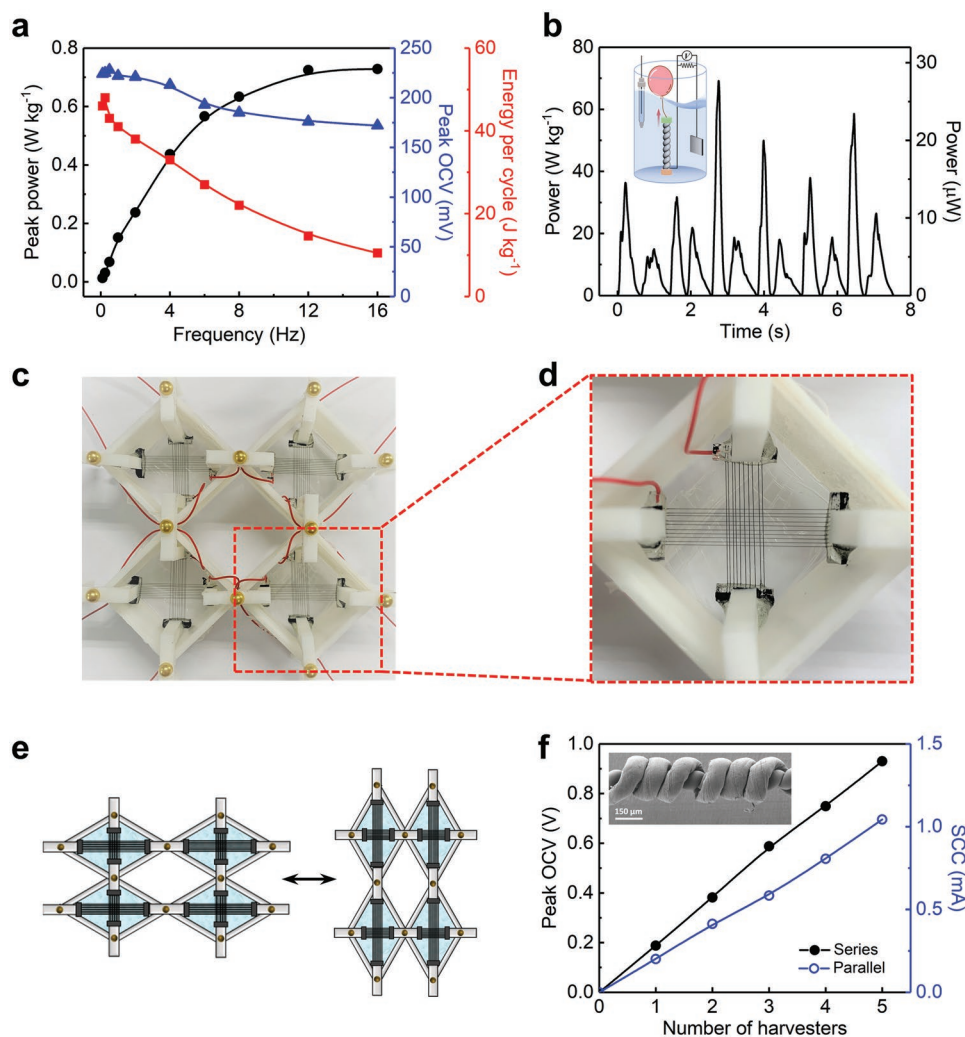
Figure 4. Application results. a) The frequency dependencies of peak power, peak OCV, and energy per cycle for a coiled rGO@CNT harvester undergoing 46% stretch in 0.6 M aqueous NaCl. b) The gravimetric and absolute power outputs of a 400 µg rGO@CNT ocean-wave harvester for mimic wave frequencies of ≈0.8 Hz, providing 20% to 30% twistron stretch in 0.6 M NaCl. (Inset) Schematic of the harvester's configuration. c,d) Optical images of the high-volume-state of a wine-rack frame twistron harvester. In each of the four wine-rack cells, 10 TOP twistron harvester yarns under 17.5% tensile strain were suspended in both the horizontal and vertical directions as opposing twistron electrodes. Each twistron yarn was 1.7 cm long and weighed 80 µg. e) Illustration of the morphing of a wine-rack twistron harvester between equivalent structures having rhombic angles of 81.7° and 98.3°. The negative and positive linear compressibility directions (with 35% and 0% tensile strain, respectively) switch between horizontal and vertical in going between these structures. f) The peak OCV and SCC at 1 Hz and 38% strain for series (black circles) and parallel (blue empty circles) connected solid-state harvesters. The rGO@CNT homochiral harvester yarn was coated with a 10 wt% PVA/0.1 M HCl gel electrolyte and heterochirally wrapped with a gel-electrolyte-coated CNT harvester yarn. (Inset) SEM image of the solid-state harvester, without the needed gel coatings.

at 1 Hz and can provide arbitrarily high voltages or currents if multiple harvesters are connected in-series or in-parallel, respectively[30] (Figure 4f; Figures S46 and S54, Supporting Information). This harvester was used as a self-powered strain sensor that usefully provides quasi-linear changes in the OCV and capacitance with applied strain (Figure S47, Supporting Information). These solid-state harvesters were sewn into a glove as self-powered strain sensors for recognizing sign language. Figure S48 (Supporting Information) compares American sign language hand gestures with the OCV profiles these gestures generated. Different letters and phrases can be easily differentiated by the output OCV profiles, which is promising for applications like sign-to-speech translation.[11,31,32]

3. Conclusion

We have found that CNT alignment importantly determines twistron performance and have correspondingly developed a host of twistron fabrication methods that importantly increase harvesting. These methods include selecting highly aligned precursor forests, applying plastic deformation, and using our ITAP and TOP processes. We also found that the output voltages and electrical power and energy are simultaneously increased by biscrolling conducting rGO nanoplates into CNT yarns. The peak and average output power for a 30 Hz sinusoidal deformation were 3.19 and 0.86 kW kg^{-1}, respectively, which are over 12- and 3-fold that of the highest values

reported for other prior-art mechanical energy harvesters for frequencies between 0.1 Hz and 600 Hz. The maximum energy conversion efficiency obtained by our interrupted deformation process was 7.2-fold that for previous twistrons. These powerful twistrons were integrated into hinged wine-rack frames and Scotch yokes to harvest tensile and torsional mechanical energy and used as self-powered strain sensors for recognizing sign language.

Although the CNT twistrons can deliver much higher electrical power densities over broad frequency ranges than prior-art technologies, an important problem remains before they can be used for large-scale applications. While many companies are working on upscaling CNT yarn production, none are yet offering kg quantities for public sale. Hence, we are presently limited to the km-length CNT yarns that can be produced in our laboratory, which typically weigh less than a gram. For harvesting scarce mechanical energy instead of abundant energy, like in ocean waves, another need is to increase the energy conversion efficiency above the presently demonstrated 7.6% maximum.

4. Experimental Section

Fabrication of Twistron Harvesters: Carbon multiwalled nanotube (MWNT) sheets, which were drawn from MWNT forests grown by chemical vapor deposition (CVD) on silicon wafers, were used to fabricate the twistron harvesters. Twistron harvester yarns were fabricated by cone-spinning, which is illustrated in Figure 1a. In an exemplary experiment, five layers of forest-drawn MWNT sheet were assembled into a ≈5 cm wide, ≈20 cm long sheet stack in which the MWNTs alignment direction was along the sheet length. Two pieces of adhesive carbon tape were attached to each end of this MWNT sheet stack, and the ≈5 cm wide sheet stack was manually rolled into a ≈1.6 cm diameter cylinder. The top of the cylinder was connected to a rotary motor. The cylinder's bottom was attached to a torsionally tethered weight that provided a stress of ≈30 MPa (when normalized to the cross-sectional area of the yarn immediately before the onset of coiling for the applied load used for coiling). Using a twist insertion speed of 100 rpm, twist was inserted about the central axis of this cylinder, which deformed into two symmetrical cones, thereby forming a dense yarn between these cones. Inserting ≈40 turns cm^{-1} of twist (normalized to the initial sheet length), while applying the above ≈30 MPa stress, produces a ≈75 μm diameter twisted yarn that was just below the twist level where coiling starts at this load. A twisted yarn was converted into the coiled yarn used for twistron harvesters by self-coiling, which means that twist was further inserted to produce a completely coiled yarn. The coiled yarn's spring index (the ratio of the difference in outer coil diameter and the fiber diameter to the fiber diameter) was about 0.45, when coiling was conducted isobarically (using the same load for twist insertion and coiling). The resulting coiled yarns were untwisted by 8% of the total inserted twist. This untwist reduces twist-induced densification without causing coil loss, which increases the electrochemical accessible area and the reversible tensile strain range, thus improving harvester performance.

Electrochemical Characterization of Harvester Performance: Unless otherwise described, three-electrode experiments were conducted using a twistron yarn as working electrode, a high-capacitance counter electrode (a Pt mesh covered with CNT sheets or graphene), and an Ag/AgCl reference electrode for aqueous electrolytes and a Pt wire reference electrode for organic electrolytes. The counter electrode had a sufficiently high capacitance, relative to the twistron electrode, that the cell capacitance was mainly determined by the capacitance of the twistron electrode. The open-circuit potential (OCP) of the twistron electrode was relative to the reference electrode, and the open-circuit voltage (OCV) and short-circuit current (SCC) were between the twistron electrode and the counter electrode. Unless otherwise mentioned, capacitance measurements were made using cyclic voltammetry (CV) curves for potentials between 0.3 and 0.6 V (vs Ag/AgCl) at a potential scan rate of 50 mV s^{-1}. Electrical power and energy output were measured by connecting an external load resistor between the twistron harvester electrode and the counter electrode, and recording the resulting voltage or current for this load resistor during mechanical deformation. Electrical power and energy output were optimized by varying the external load resistor. Unless otherwise mentioned, the reported gravimetric capacitance, peak power, and output electrical energy per cycle are normalized to the weight of the dry harvester yarn. Tensile mechanical energy harvesting was performed by stretching and releasing a coiled twistron yarn that was torsionally tethered to prohibit irreversible yarn untwist (Figure 1b). Unless otherwise indicated, the strain applied to a coiled twistron harvester before the beginning of harvesting was sufficient to prevent the yarn from snarling. Torsional mechanical energy harvesting was performed by isometrically (constant length) twisting and untwisting a twisted, noncoiled twistron yarn (Figure 1d). The energy conversion efficiency was calculated from the ratio of the electrical energy harvested to the net mechanical energy inputted (from force-displacement curves or torque-angle curves) during a deformation cycle.

Supporting Information

Supporting Information is available from the Wiley Online Library or from the author.

Acknowledgements

Conflict of Interest

Z.W., R.H.B., M.Z, W.C., S.F., S.J.K., T.J.M., and J.H.M. are the inventors of provisional U.S. patent application no. 63/235,023, submitted jointly by the Board of Regents, the University of Texas System (for the University of Texas at Dallas), and the Industry-University Cooperation Foundation of Hanyang University, that covers the design, fabrication, performance, and applications of twistron mechanical energy harvesters.

Author Contribution

R.H.B. and Z.W. conceived and initiated the project. All authors contributed to experimental design, planning, and execution; data analysis; and manuscript writing.

Data Availability Statement

The data that support the findings of this study are available from the corresponding author upon reasonable request.

Keywords

[1] Z. L. Wang, T. Jiang, L. Xu, *Nano Energy* **2017**, *39*, 9.

[2] A. T. Liu, G. Zhang, A. L. Cottrill, Y. Kunai, A. Kaplan, P. Liu, V. B. Koman, M. S. Strano, *Adv. Energy Mater.* **2018**, *8*, 1802212.

[3] V. Vallem, Y. Sargolzaeiaval, M. Ozturk, Y. C. Lai, M. D. Dickey, *Adv. Mater.* **2021**, *33*, 2004832.

[4] W. Xu, H. Zheng, Y. Liu, X. Zhou, C. Zhang, Y. Song, X. Deng, M. Leung, Z. Yang, R. X. Xu, Z. L. Wang, X. C. Zeng, Z. Wang, *Nature* **2020**, *578*, 392.

[5] Z. Zhang, X. Li, J. Yin, Y. Xu, W. Fei, M. Xue, Q. Wang, J. Zhou, W. Gou, *Nat. Nanotechnol.* **2018**, *13*, 1109.

[6] F. Yang, J. Li, Y. Long, Z. Zhang, L. Wang, J. Sui, Y. Dong, Y. Wang, R. Taylor, D. Ni, W. Cai, P. Wang, T. Hacker, X. Wang, *Science* **2021**, *373*, 337.

[7] S. H. Kim, C. S. Haines, N. Li, K. J. Kim, T. J. Mun, C. Choi, J. Di, Y. J. Oh, J. P. Oviedo, J. Bykova, S. Fang, N. Jiang, Z. Liu, R. Wang, P. Kumar, R. Qiao, S. Priya, K. Cho, M. Kim, M. S. Lucas, L. F. Drummy, B. Maruyama, D. Y. Lee, X. Lepro, E. Gao, D. Albarq, R. Ovalle-Robles, S. J. Kim, R. H. Baughman, *Science* **2017**, *357*, 773.

[8] R. Pelrine, R. D. Kornbluh, J. Eckerle, P. Jeuck, S. Oh, Q. Pei, S. Stanford, *Proc. SPIE* **2001**, *4329*, 148.

[9] S. Chiba, M. Waki, R. Kornbluh, R. Pelrine, *Proc. SPIE* **2008**, *6927*, 692715.

[10] S. Shian, J. Huang, S. Zhu, D. R. Clarke, *Adv. Mater.* **2014**, *26*, 6617.

[11] M. Li, J. Qiao, C. Zhu, Y. Hu, K. Wu, S. Zeng, W. Yang, H. Zhang, Y. Wang, Y. Wu, R. Zang, X. Wang, J. Di, Q. Li, *ACS Appl. Electron. Mater.* **2021**, *3*, 944.

[12] J. Di, S. Fang, F. A. Moura, D. S. Galvao, J. Bykova, A. Aliev, M. Jung de Andrade, X. Lepro, N. Li, C. Haines, R. Ovalle-Robles, D. Qian, R. H. Baughman, *Adv. Mater.* **2016**, *28*, 6598.

[13] M. Zhang, S. Fang, A. A. Zakhidov, S. B. Lee, A. E. Aliev, C. D. Williams, K. R. Atkinson, R. H. Baughman, *Science* **2005**, *309*, 1215.

[14] R. Malik, N. Alvarez, M. Haase, B. Ruff, Y. Song, B. Suberu, D. Shereen, D. Mast, A. Gilpin, M. Schulz, V. Shanov, *Nanotube Superfiber Materials* (Eds: M. J. Schulz, V. N. Shanov, Z. Yin), William Andrew Publishing, Norwich, NY, USA **2014**, Ch. 13.

[15] M. Xu, D. N. Futaba, M. Yumura, K. Hata, *ACS Nano* **2012**, *6*, 5837.

[16] S. Esconjauregui, R. Xie, M. Fouquet, R. Cartwright, D. Hardeman, J. Yang, J. Robertson, *J. Appl. Phys.* **2013**, *113*, 144309.

[17] E. Bandley, E. Greenhalgh, M. Shaffer, Q. Li, *Carbon* **2018**, *137*, 78.

[18] M. Zhang, S. Fang, J. Nie, P. Fei, A. E. Aliev, R. H. Baughman, M. Xu, *Adv. Funct. Mater.* **2020**, *30*, 2004564.

[19] C. S. Haines, M. D. Lima, N. Li, G. M. Spinks, J. Foroughi, J. D. W. Madden, S. H. Kim, S. Fang, M. Jung de Andrade, F. Goktepe, O. Goktepe, S. M. Mirvakili, S. Naficy, X. Lepro, J. Oh, M. E. Kozlov, S. J. Kim, X. Xu, B. J. Swedlove, G. G. Wallace, R. H. Baughman, *Science* **2014**, *343*, 868.

[20] M. D. Lima, N. Li, M. Jung de Andrade, S. Fang, J. Oh, G. M. Spinks, M. E. Kozlov, C. S. Haines, D. Suh, J. Foroughi, S. J. Kim, Y. Chen, T. Ware, M. K. Shin, L. D. Machado, A. F. Fonseca, J. D. W. Madden, W. E. Voit, D. S. Galvao, R. H. Baughman, *Science* **2012**, *338*, 928.

[21] M. D. Lima, S. Fang, X. Lepro, C. Lewis, R. Ovalle-Robles, J. Carretero-Gonzalez, E. Castillo-Martinez, M. E. Kozlov, J. Oh, N. Rawat, C. S. Haines, M. H. Haque, V. Aare, S. Stoughton, A. A. Zakhidov, R. H. Baughman, *Science* **2011**, *331*, 51.

[22] C. Xiang, C. C. Young, X. Wang, Z. Yan, C. C. Hwang, G. Cerioti, J. Lin, J. Kono, M. Pasquali, J. M. Tour, *Adv. Mater.* **2013**, *25*, 4592.

[23] R. Jalili, S. H. Aboutalebi, D. Esrafilzadeh, R. L. Shepherd, J. Chen, S. Aminorroaya-Yamini, K. Konstantinov, A. I. Minett, J. M. Razai, G. G. Wallace, *Adv. Funct. Mater.* **2013**, *23*, 5345.

[24] C. Wei, X. Jing, *Renewable Sustainable Energy Rev.* **2017**, *74*, 1.

[25] W. R. Heinzelman, A. Chandrakasan, H. Balakrishnan, in *Proc. 33rd Hawaii Int. Conf. on System Sciences*, IEEE, Piscataway, NJ, USA **2000**, p. 8020.

[26] Z. L. Wang, *Nature* **2017**, *542*, 159.

[27] R. H. Baughman, S. Stafström, C. Cui, S. O. Dantas, *Science* **1998**, *279*, 1522.

[28] X. Zhou, L. Zhang, H. Zhang, Q. Liu, T. Ren, *Phys. Status Solidi B* **2016**, *253*, 1977.

[29] J. X. Tao, N. Y. Viet, A. Carpinteri, Q. Wang, *Energy Struct.* **2017**, *133*, 74.

[30] H. Wang, Y. Sun, T. He, Y. Huang, H. Cheng, C. Li, D. Xie, P. Yang, Y. Zhang, L. Qu, *Nat. Nanotechnol.* **2021**, *16*, 811.

[31] Z. Zhou, K. Chen, X. Li, S. Zhang, Y. Wu, Y. Zhou, K. Meng, C. Sun, Q. He, W. Fan, E. Fan, Z. Lin, X. Tan, W. Deng, J. Yang, J. Chen, *Nat. Electron.* **2020**, *3*, 571.

[32] T. He, Q. Shi, H. Wang, F. Wen, T. Chen, J. Ouyang, C. Lee, *Nano Energy* **2019**, *57*, 338.

ADVANCED MATERIALS

Supporting Information

More Powerful Twistron Carbon Nanotube Yarn Mechanical Energy Harvesters

Zhong Wang, Tae Jin Mun, Fernando M. Machado, Ji Hwan Moon, Shaoli Fang, Ali E. Aliev, Mengmeng Zhang, Wenting Cai, Jiuke Mu, Jae Sang Hyeon, Jong Woo Park, Patrick Conlin, Kyeongjae Cho, Enlai Gao, Gang Wan, Chi Huynh, Anvar A. Zakhidov, Seon Jeong Kim,* and Ray H. Baughman*

Supporting Information

More powerful twistron carbon nanotube yarn mechanical energy harvesters

Zhong Wang[1], Tae Jin Mun[2], Fernando M. Machado[1,3], Ji Hwan Moon[2], Shaoli Fang[1], Ali E. Aliev[1], Mengmeng Zhang[1], Wenting Cai[1,4], Jiuke Mu[1], Jae Sang Hyeon[2], Jong Woo Park[2], Patrick Conlin[5], Kyeongjae Cho[5], Enlai Gao[6], Gang Wan[7], Chi Huynh[8], Anvar A. Zakhidov[1], Seon Jeong Kim[2†], Ray H. Baughman[1†]

[1] Alan G. MacDiarmid NanoTech Institute, University of Texas at Dallas, Richardson, TX 75080, USA.

[2] Center for Self-Powered Actuation, Department of Biomedical Engineering, Hanyang University, Seoul 04763, Korea.

[3] Technology Development Center, Federal University of Pelotas, Pelotas, RS 96010-610, Brazil.

[4] School of Chemistry, Xi'an Jiaotong University, Xi'an, Shaanxi 710049, China.

[5] Department of Materials Science and Engineering, University of Texas at Dallas, Richardson, TX 75080, USA.

[6] Department of Engineering Mechanics, School of Civil Engineering, Wuhan University, Wuhan, Hubei 430072, China.

[7] Department of Mechanical Engineering, Stanford University, Stanford, CA 94305, USA.

[8] Nano-Science and Technology Center, Lintec of America, Richardson, TX 75081, USA.

†Corresponding author. Email: sjk@hanyang.ac.kr (S.J.K.); ray.baughman@utdallas.edu (R.H.B.)

Table of Contents

1. Materials and Methods

1.1 The fabrication and structure of twistron harvesters

Carbon multiwalled nanotube (MWNT) sheets, which were drawn from MWNT forests[1], were used to fabricate our twistron harvesters. These MWNT forests were grown by chemical vapor deposition (CVD) on silicon wafers that were coated by ~3-nm-thick catalytic iron nanoparticles. Forests with different volumetric densities and degrees of CNT alignment were grown by tuning the areal density of the iron catalyst that was deposited on silicon wafer growth substrates. For typically used forests, scanning electron microscopy (SEM) and transmission electron microscope (TEM) images show that the forest height is ~300 µm and the MWNTs have an outer diameter of ~9 nm, contain ~6 walls and aggregate into irregularly shaped large bundles. Thermogravimetric analysis (TGA) in air shows that the weight of non-combustible materials in the drawn MWNT sheets was below 1%.

MWNT twistron harvester yarns were fabricated by cone-spinning, which is illustrated in Figure 1a. In an exemplary experiment, five layers of forest-drawn MWNT sheet were assembled into a ~5-cm-wide, ~20-cm-long sheet stack in which the MWNTs alignment direction was along the sheet length direction. Two pieces of adhesive carbon tape were attached to each end of this MWNT sheet stack, and the ~5-cm-wide flat sheet stack was manually rolled into a ~1.6-cm-diameter cylinder. The top of the cylinder was connected to a rotary motor. The cylinder's bottom was attached to a torsionally tethered weight that provided a stress of ~30 MPa (when normalized to the cross-sectional area of the yarn immediately before the onset of coiling for the applied load used for coiling). Using a twist insertion speed of 100 rpm, twist was inserted about the central axis of this cylinder, which deformed into two symmetrical cones, thereby forming a dense yarn between these cones. Inserting ~40 turns cm^{-1} of twist (normalized to the initial sheet length), while applying the above ~30 MPa stress, produces a ~75-µm-diameter twisted yarn that was just below the twist level where coiling starts at this load. Twist insertion into a planar MWNT ribbon can provide similar performance as a cone-spun yarn if the applied stresses on the ribbon are uniform, so that the twist-spun yarn has a Fermat structure. However, small deviations from stress uniformity results in a yarn having a dual-Archimedean structure. The resulting oppositely directed twist insertion directions for opposite sides of the dual-Archimedean structure partially cancels the capacitance change that drives energy harvesting[2].

A twisted yarn was converted into the coiled yarn used for twistron harvesters by self-coiling, which means that twist was further inserted to produce a completely coiled yarn. The coiled yarn's spring index (the ratio of the difference in outer coil diameter and the fiber diameter to the fiber diameter) was about 0.45, when coiling was conducted isobarically (using the same load for twist insertion and coiling). The resulting coiled yarns were untwisted by 8% of the total inserted twist. This untwist reduces twist-induced densification without causing coil loss, which increases the electrochemical accessible area and the reversible tensile strain range, thus improving harvester performance[2].

Twistrons with stretch-enhanced alignment were fabricated by irreversibly stretching the twisted yarn prior to isobaric coiling, which increased the performance of the self-coiled yarn. Twisted yarns with an initial bias angle of 22° and an inserted twist of 16 turns cm^{-1} were mechanically stretched until targeted engineering strains were achieved. The irreversible mechanical stretching was conducted using an Instron 5848 Microtester at a strain rate of 0.2 mm min^{-1}. A yarn gauge length of 80 mm was used, and both ends of the yarn were bound to strips of paper by Gorilla super glue to avoid stress concentration. The degree of irreversible stretch was

measured for each of the maximum applied strains by keeping the yarn at this strain until the applied force becomes constant. After stretching, the clamped regions were discarded, and further twist was inserted to produce a completely coiled yarn.

ITAP twistrons were fabricated by our incandescence tension anneal process (ITAP), which was conducted within a vertically placed cylindrical quartz tube under 10^{-6} to 10^{-7} bar vacuum[3]. During ITAP, ultrahigh temperatures (~3000 ℃, measured spectroscopically using black body radiation and confirmed by extrapolation of the measured temperature dependence of resistance at low temperatures to obtain the temperatures corresponding to the measured resistance at high temperatures) were applied by incandescently heating the twisted yarn while under load. An approximately 8-cm-long twisted yarn was connected to two electrodes and an electrical current was applied to reach the desired temperature through Joule heating. A small current was applied to remove surface adsorbed oxygen before heating the yarn to incandescent temperatures. Tensile stress was applied during heating by hanging various loads on the bottom end of the yarn. The applied current was abruptly terminated after the desired annealing time was achieved, and the yarn automatically rapidly cooled to room temperature in vacuum. After ITAP, these yarns were coiled, just like for other twistron yarns.

Twistrons containing nanoplatelets of graphene oxide (GO) were made by our biscrolling process[4], using GO (with lateral size of 10-25 μm) synthesized by the method described in Section 1.2. During biscrolling, the GO was dispersed in water by stirring to make a 0.2 to 1 mg mL^{-1} aqueous solution (depending upon the targeted GO content). This dispersion was sprayed on a forest-drawn CNT sheet (on a glass substrate) using an airbrush, and then the resulting bilayer sheet stack was peeled from the glass substrate and twist was inserted until a twisted, non-coiled yarn was obtained. The low-twist-density GO@CNT yarn made by the above process, which had a bias angle of 22º, was reduced in vacuum by electrical heating to about 3000 °C under mechanical load for 1-2 minutes. The resulting rGO@CNT yarn was twist inserted, under the same load used for the initial twist insertion, until fully coiled. Unless otherwise mentioned, 29 wt % GO@CNT was used to produce the described rGO@CNT yarns (which optimized the energy harvesting performance). Silver nanowire biscrolled twistron yarns were made by a similar biscrolling process[5], using a 0.2 mg mL^{-1} aqueous dispersion solution for the spray coating.

The above described twistron fabrication used the same applied load for both yarn twist and yarn coiling. We discovered that the performance of twistron harvesters can be improved by using a much higher load during pre-coiling twist insertion than applied during the twist insertion that results in coiling. We call this our tension optimization process (TOP). In this process, the peak and average power output of the coiled CNT twistron harvester were approximately optimized by applying a stress of about 140 MPa during pre-coiling twist insertion. Using the above-described cone-spinning process, 40 turns cm^{-1} of twist per sheet length was inserted under the initial twist insertion load and then the load used for coiling was applied while keeping the twisted yarn torsionally tethered. Here and elsewhere, this stress was calculated by using the diameter of the yarn (under the coiling load) immediately before the onset of coiling. Twist was inserted under the coiling load until the yarn completed coiling. For an initial twisting load of 140 MPa and a 3.2 MPa load applied during coiling, the pre-coiling twist under high load and the twist needed to complete coiling under the low load were 40 and 55 turns cm^{-1}, respectively, when normalized to the initial sheet length. Unless otherwise noted, these load conditions were used during twist insertion to produce coiling. More generally, the coiling stress that optimized harvesting was about 2.3% of the stress applied during the pre-coiling twist insertion process.

Depending upon the desired direction of potential change upon stretch, mandrel-coiled homochiral and heterochiral yarns (where yarn twist and yarn coiling had either the same or opposite chirality, respectively) were made by wrapping highly twisted yarns (twisted to immediately before the onset of coiling) around a 1-mm-diameter rubber core, which was pre-stretched by 200%. The highly twisted yarn was compactly wrapped around the mandrel core. The chirality of coil wrapping was the same as the yarn twist chirality for a homochiral yarn and was opposite for a heterochiral yarn (Figure S45). This use of a rubber mandrel core during energy harvesting provided a lower bound on coil diameter, which prevented coil collapse and permanent twist cancellation of the oppositely directed yarn twist and yarn coiling for the heterochiral yarn. Unlike the case for a mandrel-free, self-coiled homochiral yarn, mandrel coils supported on a rubber core will more substantially decrease diameter during stretch (depending upon the rubber fiber's high Poisson's ratio of about 0.5), which increases stretch-torsional coupling for heterochiral coils, but decreases this coupling for homochiral coils. The energy harvesting performance of the homochiral rubber-core twistron was correspondingly decreased compared with that for a mandrel-free, self-coiled homochiral twistron.

Solid-state, dual-electrode twistron harvesters were also made in which a homochiral self-coiled twistron (working electrode) was wrapped with a heterochiral mandrel-coiled twistron (counter electrode) and mechanically coupled by an electronically separating poly(vinyl alcohol) gel electrolyte (comprising 10 wt % PVA/0.1 M HCl), thereby eliminating the need for an electrolyte bath (Figure 4f). The gel was fabricated by heating the PVA powder in a stirred aqueous HCl solution for 30 minutes at 80 °C. The thereby obtained gel electrolyte was deposited on both the working electrode and counter electrode, so that it both coats and ionically interconnects these electrodes, while providing electronic inter-electrode insulation. These dual-electrode twistrons were sewn into a glove using a straight/running stitch for use as a self-powered sensor of finger movement (Figure S48).

1.2 Source and nature of materials

The following materials were from MilliporeSigma: (1) poly(vinyl alcohol), PVA, with an average molecular weight of ~145,000, (2) an aqueous dispersion of silver nanowires, with 35 nm (±5 nm) diameter and 25 μm (±5 μm) length, (3) lithium tetrafluoroborate ($LiBF_4$), and acetonitrile (ACN).

Large lateral size (10-25 μm) GO platelets were synthesized as follows[6]. Dry, sulfuric acid-intercalated expandable graphite flakes (3772, Asbury Graphite Mills USA) were first thermally treated in air at 1050 °C for 15 seconds. The expanded graphite (5 g) was then mixed and stirred in 1 L of sulfuric acid for 24 hours. Potassium permanganate ($KMnO_4$, 50 g) was then slowly added to the mixture while the mixture was in an ice bath. Deionized water (DI water, 1 L) and 250 mL of hydrogen peroxide (H_2O_2, 3%) were slowly poured into the stirred mixture, causing the solution to become a light brown color. The solution containing GO was further stirred for 30 minutes and then centrifuged and washed with dilute hydrochloric acid (~3 wt % HCl). It was then washed with DI water until the pH of the solution reached 5 to 6. The resulting large GO nanoplatelets were dispersed in DI water by gentle shaking.

1.3 Methods and apparatus for characterizations

A Zeiss SUPRA 40 SEM was used for scanning electron microscope (SEM) imaging. The mechanical properties of twistron yarns were measured on a Instron 5848 Microtester using a 5-N load cell, a 0.1-mm per minute stretch rate, and a 13-mm gauge length. The reported specific strengths were calculated from the tensile force normalized with respect to the linear density of the unstrained yarn. A microbalance (UMX2, Mettler Toledo) was used for measuring the mass

of twistron yarns. Raman spectra were obtained on a Horiba Jobin Yvon LabRam HR Micro-Raman Spectrometer, using a 632.8 nm wavelength (1.96 eV) laser excitation line with 3 mW power and a 100X objective lens. Spectra were acquired from 100 to 3500 cm^{-1} using a 950 gr/mm grating, which provides a resolution of 1 cm^{-1}.

Electrochemical measurements were performed using a Gamry 3000 potentiostat. Unless otherwise described, three-electrode experiments were conducted using a twistron yarn as working electrode, a high capacitance counter electrode (a Pt mesh covered with CNT sheets or graphene), and an Ag/AgCl reference electrode for aqueous electrolytes and a Pt wire reference electrode for organic electrolytes. The counter electrode had a sufficiently high capacitance, relative to the twistron electrode, that the cell capacitance was mainly determined by the capacitance of the twistron electrode. The open-circuit potential (OCP) of the twistron electrode was relative to the reference electrode, and the open-circuit voltage (OCV) and short-circuit current (SCC) were between the twistron electrode and the counter electrode. Unless otherwise mentioned, capacitance measurements were made using cyclic voltammetry (CV) curves for potentials between 0.3 and 0.6 V (vs. Ag/AgCl) at a potential scan rate of 50 mV s^{-1}. Electrical power and energy output were measured by connecting an external load resistor between the twistron harvester electrode and the counter electrode, and recording the resulting voltage or current for this load resistor during mechanical deformation. Electrical power and energy output were optimized by varying the external load resistor. Unless otherwise mentioned, the reported gravimetric capacitance, peak power, and output electrical energy per cycle are normalized to the weight of the dry harvester yarn. Tensile mechanical energy harvesting was performed by stretching and releasing a coiled twistron yarn that was torsionally tethered to prohibit irreversible yarn untwist (Figure 1b). Unless otherwise indicated, the strain applied to a coiled twistron harvester before the beginning of harvesting was sufficient to prevent the yarn from snarling. The tensile deformation was modulated by a home-made device that contains a step motor and a gear box that translate the rotation motion of a step motor to tensile deformation. Torsional mechanical energy harvesting was performed by isometrically (constant length) twisting and untwisting a twisted, non-coiled twistron yarn (Figure 1d). The energy conversion efficiency was calculated from the ratio of the electrical energy harvested to the net mechanical energy inputted (from force-displacement curves or torque-angle curves) during a deformation cycle.

We found for a sinusoidal stretch and release, at any frequency and for any stretch amount, that the harvested energy, as well as the peak power density, can be approximately maximized by selecting the load resistance so that it provides a peak-to-peak output voltage that is one-half of the harvesters open circuit voltage. For instance, Figure S22 shows that the peak power and energy-per-cycle was approximately maximized for a load resistance of between 275 and 325 ohms for harvesting at 1 Hz, which provided a peak-to-peak voltage drop across the load resistors of 168 and 176 mV, respectively. For comparison, one-half of the OCV at this frequency was 175 mV. Also, the peak power and energy-per-cycle in Figure S40 is maximized for a load resistance of between 350 and 400 ohms at 1 Hz. For these load resistances, the peak-to-peak voltage drop across the load resistors were 104 and 113 mV, respectively, as compared with one-half of the OCV (111 mV) at this frequency before harvesting. In contrast with the above results, Figure S44b (inset) shows that the resistance that maximizes the average power density and the peak power density for square-wave strain excitation differ, and both depend upon excitation frequency.

Small angle X-ray scattering (SAXS) measurements were performed on Beamline 1-5 at the Stanford Synchrotron Radiation Lightsource (SSRL) of the SLAC National Accelerator Laboratory. The X-ray energy was 15 keV and the sample-to-detector distance was calibrated using a silver behenate standard. The beam-spot size was 500 μm × 500 μm, and exposure time was 5 s. The scattered patterns were collected using a Mar charge-coupled device (CCD) area detector. The obtained 2D image were reduced and analyzed using Nika package[7]. Additional measurements were repeated on Beamline 33-ID of the Advanced Photon Source of the Argonne National lab. Wide angle X-ray scattering (WAXS) measurements were performed using a Bruker D8 Venture diffractometer with a Photon 100 Detector and Cu source (8.0478 keV). The exposure time was 60 s. The images obtained were analyzed using GSAS-II[8].

2. Optimizing harvester performance by tuning CNT alignment

2.1 Analysis of CNT alignment

High CNT alignment in a forest is needed for high sheet draw-ability from the forest, and the alignment in a drawn sheet increases with increasing CNT alignment in the precursor forest. The capacitance of the twistron yarn and its performance as a harvester are sensitive to the structural nature of the forest-drawn CNT sheets used as precursor for the cone spun yarns (Figure 1c). This sheet alignment was quantified by the Herman's Orientation Factor, HOF, which was obtained from fast Fourier transforms of SEM images of the CNT sheet[9]. The HOF ranged from about 0.49 to 0.75 for sheets that are drawn from our high-density forests, where HOFs of 0 and 1 correspond to a randomly oriented sheet and a perfectly oriented sheet, respectively. We used the same method to characterize HOF for the surfaces of twisted CNT yarns.

Figure S1 illustrates the method used to determine the HOF of CNT sheets. SEM images at different magnifications, which optimized the HOF calculation[9], were obtained using an accelerating voltage of 5 kV for the secondary electron detector and a working distance between 5 and 10 mm (Figure S1a). The magnifications were converted to pixels/nm. A two-dimensional fast Fourier transformation (FFT) power spectrum was calculated from the contrast-enhanced SEM images (8-bit grayscale) using the inbuilt FFT function in ImageJ software (Figure S1b). This Fourier transform sorts out repetitive elements in the original space domain image and manifests them in the frequency domain. If an array of fiber-like structures (such as the CNTs observed by SEM) are predominantly oriented in a given direction, the FFT power spectrum will be low in that direction and will be high in the perpendicular direction. The azimuthal distribution of intensity profile I(θ) was generated by summing the intensity radially for each angle θ (0 for the horizontal direction and $\frac{\pi}{2}$ for the vertical direction). This summed intensity profile was fitted to a generalized normal distribution[10]:

$$I(\theta) = a\ exp\left(-\left(\frac{|\theta - \mu|}{b}\right)^c\right),$$

where the coefficient a determines the peak amplitude, b determines the peak width, c determines the peak sharpness, and μ is the predominant orientation direction. This generalized normal distribution becomes a normal distribution when $c = 2$, and a Laplace distribution when $c = 1$. Figure S1c shows the high-quality fit of the generalized normal distribution to the experimental data. Finally, HOF was calculated using the following equation:

$$HOF = \frac{3cos^2\theta - 1}{2},$$

where

$$cos^2\theta = \frac{\int_0^\pi I(\theta)cos^2\theta sin\theta d\theta}{\int_0^\pi I(\theta)sin\theta d\theta},$$

and $I(\theta)$ is the intensity of the experimental data fitted generalized normal distribution.

Figure S1d shows the dependence of the calculated HOF on the SEM image magnification for five randomly selected areas in a forest-drawn CNT sheet. All used magnifications show small derivations between different areas and the HOF for the same area increases little with increasing magnification. These results agree with a literature report that HOF consistently falls in a narrow range when a resolution of 1-3 pixels/CNT diameter is used (*9*). Lower magnification will increase this deviation because individual CNT bundles will not be sufficiently resolved. At higher magnifications, additional details in the image (like surface texture, surface contaminants, and imaging noise), which are not related to CNT orientation, start to appear. Since the five randomly selected areas provide the best fit of HOF at a magnification of 0.173 pixels/nm, this magnification was used.

Figure S2 compares results for three forest-drawn CNT sheets having different alignment: their SEM images, corresponding FFT power spectrums, and azimuthal orientation distribution functions. CNT sheets with lower alignment have a more circular aspect power spectrum. CNT sheets with higher alignment have a more anisotropic power spectrum, with a strong signal in the horizontal direction, which corresponds to high alignment in the vertical direction in image space (Figures S2b, S2e, S2h). CNT sheets with higher alignment have narrower orientation distribution (peak width) compared with CNT sheets with lower alignment (Figures S2c, S2e, S2i).

2.2 The effect of the alignment of forest-drawn CNT sheets on tensile and torsional mechanical energy harvesting

Figure 1c and Figure S3 show the mechanical energy harvester performance during a 1 Hz sinusoidal deformation for a coiled twistron harvester, as well as the effect of stretch on capacitance. From these results, we found that CNT alignment in the precursor CNT sheets importantly determines twistron performance. With a similar spring index and strain range, a peak OCV, peak power, and energy per cycle of 274 mV, 210 W kg^{-1}, and 65 J kg^{-1} (Figures S3b, S3d) were achieved for a twistron made from a sheet with a HOF of 0.64, compared with 102 mV, 47 W kg^{-1}, and 12 J kg^{-1} (Figures S3a, S3c) for a twistron made from a sheet with a HOF of 0.49. This major performance difference is because of the higher effective surface area for interaction of highly aligned CNT bundles, compared with that for less aligned bundles, as demonstrated by the much larger stretch-induced capacitance change for the highly aligned CNTs (45%) than for the less aligned CNTs (19%) (Figures S3e, S3f). This performance enhancement exists even though the capacitance of the less aligned CNTs (11.2 F g^{-1}) is much larger than for the highly aligned CNTs (4.4 F g^{-1}).

This performance advantage, due to optimized alignment of the precursor CNT sheets, is also evident in torsional mechanical energy harvesting by isometric twist insertion and removal from non-coiled CNT yarns. Figures S4-S6 compare the torsional harvester performance (in 0.1 M aqueous HCl) of twisted yarns made using CNT sheets having HOFs of 0.64 (Figure S4), 0.58 (Figure S5), and 0.52 (Figure S6). For a twisting speed of 300 rpm, the peak OCV (210 mV) for the twistron yarn made from a CNT sheet with a HOF of 0.64 was much higher than that of 160 mV and 90 mV for twistrons made from CNT sheets with HOFs of 0.58 and 0.52, respectively. Similar electrical power and energy output advantages were observed for all twisting speeds for

9

twistron yarn made from the higher alignment precursor CNT sheets (Figures S4d, S5d, S6d). For a twisting speed of 900 rpm, a twistron made from a precursor sheet with a HOF of 0.64 had a peak power, average power and energy per cycle of 134.3 W kg^{-1}, 22.5 W kg^{-1}, and 105.1 J kg^{-1}, respectively. For the same twisting speed, much lower performance resulted for twistrons made from precursor sheets having HOFs of 0.58 (76.6 W kg^{-1}, 14.4 W kg^{-1}, and 68.6 J kg^{-1}, respectively) and 0.52 (16.2 W kg^{-1}, 3.3 W kg^{-1}, and 20.0 J kg^{-1}, respectively).

Twisted, non-coiled CNT yarns provided an ideal system for investigating the effects of precursor sheet alignment on twist-induced bundle interactions and resulting capacitance changes. Figure 1e shows that the twist dependence of peak OCV, capacitance change, and resistance change monotonically increase with increasing HOF of the precursor sheet. This similar trend of capacitance and resistance decrease with inserted twist for yarns made from different HOF precursor sheets provides further evidence that our twistron energy harvesting behavior originates from interactions between CNT bundles and that highly aligned CNT bundles have higher effective surface area for this interaction, which enables increased energy harvesting.

2.3 The use of stretch-induced CNT alignment to increase twistron performance

We next investigated the enhancement of coiled twistron performance by providing irreversible stretch-induced plastic deformation of the twisted yarn prior to coiling, which results in increased CNT alignment. Figure S7a shows the stress-strain curve for a twisted yarn with initial bias angle of 22° and an inserted twist of 16 turns cm^{-1}, which has a breaking strain of 4.25% and a specific strength of 0.84 GPa (g cm^{-3})$^{-1}$. Figure 2a and Figures S7b-S7f show that with increasing strain applied to the twisted yarn (up to close to the fracture strain of 4.25%), the HOF of the twisted yarn monotonically increased from 0.62 to 0.71 (because of the plastic deformation of the CNT yarn), while the coiled yarn's capacitance was little effected. This combination of an increased HOF with a well-maintained capacitance for stretch-induced alignment provides a major advantage compared with increased sheet alignment by increasing the CNT forest density. Figure 1c shows that twistron performance was maximized for sheets having HOFs between 0.60 and 0.68. Further increase of forest density, which yields forest-drawn sheets with a HOF higher than 0.7, decreases energy harvesting due to the large bundle sizes resulting from very high CNT alignment, and the resulting small accessible electrochemical area (and capacitance). The results of Figure 2a show that twistron energy harvesting during 1 Hz deformation was monotonically increased by increasing the applied irreversible strain on the precursor twisted yarns. More specifically, the peak OCV, peak power, and harvested energy per cycle were increased from 230 mV, 187 W kg^{-1}, and 62 J kg^{-1}, respectively, for the coiled yarn derived from the pristine twisted yarn to 292 mV, 318 W kg^{-1}, and 99 J kg^{-1}, respectively, for the coiled yarn derived from the 4% pre-strained twisted yarn.

Figure 2b shows the frequency dependence of performance enhancements that result from this partially irreversible yarn stretch in the twisted state during the preparation of a coiled twistron. The maximum peak power, average power, and energy per cycle were increased by 1.68, 1.48, and 1.74 times, respectively, from 0.76 kW kg^{-1}, 0.21 kW kg^{-1}, and 69 J kg^{-1}, respectively, for the pristine yarn to 1.28 kW kg^{-1}, 0.31 kW kg^{-1}, and 120 J kg^{-1}, respectively, for the 4% pre-strained yarn.

3. Increasing harvesting performance by using ITAP

3.1 The effect of the bias angle of the twisted yarn, the applied stress during ITAP, and the ITAP time on tensile energy harvesting

The incandescence tension anneal process (ITAP), where ultrahigh temperatures (above 2500 °C) are applied by incandescently heating the twisted yarn while under load, were next investigated to increase CNT alignment and dramatically increase twistron harvesting. The performance results described are for coiled twistrons prepared from ITAP treated twisted yarns. The ultrahigh applied temperature, along with the applied stress, facilitated CNT rearrangement that increased nanotube alignment. Figure S8a shows for tensile energy harvesting at 1 Hz that the peak OCV, peak power, and energy per cycle initially increase with increasing bias angle of the precursor twisted yarn during ITAP, and were maximized for a bias angle of 22˚. For these results, the applied stress during ITAP was 34 MPa, the ITAP time was 90 seconds, and the annealing temperature was ~3000 °C. Further increase of the twist density (and the corresponding bias angle) during ITAP resulted in a rapid decrease in the performance of the coiled twistron harvesters. This is likely because high inserted twist, and associated high inter-bundle stresses, limits the effects of ITAP on improving CNT orientation in the yarn or freezes the structural changes that result in twist-induced capacitance decreases.

Figure S8b shows that twistron harvesting was optimized when the applied stress during ITAP was 34 MPa, which is close to the load applied during twisting and coiling (~30 MPa). This is likely because low applied stresses cannot effectively facilitate CNT rearrangement, while very high applied stresses (and associated inter-bundle stresses) result in large bundle sizes that decrease the capacitance that is available for energy harvesting (Figure S8c).

Figure S9 shows structural evolution as a function of annealing time for a twisted yarn (with an initial bias angle of 22˚), when this yarn was thermally annealed during ITAP while under a 34 MPa stress. The nanotube alignment on the yarn surface increased from a HOF of 0.59 to 0.74 after 30 seconds of ITAP, and then more gradually increased with further increase of ITAP time. On the other hand, the capacitance of the coiled ITAP yarn increased from 5.56 to 9.24 F g^{-1} after 15 seconds of ITAP, and then decreased with further increased ITAP time, because of the capacitance decrease caused by increased bundling (Figure 2d). Twistron harvesting was optimized for an annealing time of 90 seconds, which maximized the capacitance change during harvesting by realizing as high alignment as possible without suffering from large increases in bundle diameter. With the combined effects of bias angle, applied stress, and ITAP time optimized, a peak OCV of 325 mV, a peak power of 360 W kg^{-1}, and an energy per cycle of 95 J kg^{-1} were obtained for a 1 Hz stretch (Figure 2e). This performance is much higher than obtained at this frequency when ITAP was not used: a peak OCV of 228 mV, a peak power of 126 W kg^{-1}, and an energy per cycle of 36 J kg^{-1}. The maximum values of peak power and average power in the plateau's frequency range were increased from 604 and 156 W kg^{-1}, respectively, for the pristine yarn to 1451 and 348 W kg^{-1}, respectively, for the ITAP yarn (Figure 2f and Figure S8d).

The benefits of applying ITAP to forest-selected yarns result from eliminating the decrease in OCV and average power output when HOF exceeds 0.65. The structural improvements resulting from forest-selection, pre-stretch, and ITAP cannot be solely described by the HOF, since pre-stretch and ITAP result in peak OCV and average output power values at 1 Hz that increase with HOF increases up to near the maximum observed HOF, but these parameters decrease with increasing HOF above 0.65 if only forest-selection was used (Figure S10).

3.2 The effect of ITAP treatment on twistron yarn capacitance, potential of zero charge (pzc), and mechanical properties

In order to understand the surprising increase in capacitance that results from using a short annealing time during ITAP (15 s), compared to the capacitance obtained when ITAP was not

used, twistron yarn capacitances were obtained from CV scans and from electrochemical impedance spectroscopy (EIS). EIS was measured for coiled twistron yarns over the frequency range from 50 mHz to 100 kHz and the potential range from -0.2 V to 0.8 V (versus an Ag/AgCl reference electrode), with a potential step of 0.1 V. For each used potential and frequency f, the gravimetric electrochemical double-layer capacitance (C_{EDL}) was calculated using the following equation:

$$C_{EDL} = \frac{|I_m(z)|}{2\pi f \left[\left(I_m(z)\right)^2 + \left(R_e(z)\right)^2\right] m} ,$$

where $I_m(z)$ and $R_e(z)$ are the imaginary and real parts of impedance, and m is the mass of the twistron yarn.

For a pristine CNT twistron yarn, Figure S11a shows the frequency dependence of capacitance for various applied potentials. As typical for materials, the capacitance was high at low frequencies and decreases with increasing frequency. At 50 mHz, which is the lowest measured frequency, the capacitances (8.93 and 9.58 F g^{-1}) from EIS for 0.4 V and 0.5 V applied potential were similar to the average capacitance calculated from CV scans between 0.3 V to 0.6 V at a scan rate of 50 mV s^{-1} (8.65 F g^{-1}, for an average potential of 0.45 V). Figure S11b shows the dependence of EIS-measured capacitance (at 50 mHz frequency) on the applied potential for various coiled twistrons. The pristine CNT yarn shows a minimum capacitance around 0 V, while the capacitance of the ITAP CNT yarn monotonically increased from 5.38 F g^{-1} at -0.2 V to 12.47 F g^{-1} at 0.8 V. The potential at which capacitance is minimized should approximately correspond to the pzc, which was measured versus Ag/AgCl for aqueous electrolytes[11]. The results in Figure S11b indicate that ITAP treatment shifts the minimum in the capacitances from about 0 V for the coiled pristine CNT yarn to about -0.2 V for the coiled ITAP yarn.

The exact pzc for pristine CNT and ITAP CNT coiled twistron yarns were next determined by using piezoelectrochemical spectroscopy (PECS)[2]. During PECS, a cyclic voltammetry (CV) scan is conducted while the yarn is sinusoidally stretched. The pzc is the potential at which the stretch-induced current change becomes zero. PECS shows that the pzc for the pristine yarn was at -80 mV and shifted to -210 mV for the ITAP yarn (Figure S12). Since the measured capacitance, either from a CV scan or from EIS, increases with increased injected charge, the capacitance should be minimized at the pzc. Consequentially, the higher capacitance for the ITAP yarn can be at least partially explained by the shift in pzc caused by ITAP. The results of Supplementary Figure S11b show that if the capacitance data for pristine coiled yarn is shifted negatively by 0.2 V (the difference in the pzc and the applied potential, both versus the reference electrode), the capacitance difference between a pristine coiled yarn and an ITAP coiled CNT yarn is decreased, but far from eliminated.

The effect of ITAP on the mechanical properties of twisted yarns are shown in Figure S13. The pristine CNT yarn has a specific strength of 1 GPa (g cm^{-3})$^{-1}$ and a specific modulus of 15.4 GPa (g cm^{-3})$^{-1}$. The ITAP CNT yarn shows a substantially increased specific strength of 1.2 GPa (g cm^{-3})$^{-1}$ and specific modulus of GPa (g cm^{-3})$^{-1}$, though the breaking strain of 3.18% was lower than the 6.51% for the pristine yarn. This increase in specific strength and modulus can be attributed to the increased CNT alignment and enhanced inter-nanotube connections resulting from ITAP[3].

4. Structure changes and performance improvements by using the TOP (tension optimization process) during twistron fabrication

Figure S14b shows that the CNT yarn that is fully twisted under a low load (top left) has much lower CNT alignment (a HOF of 0.59) than for a CNT yarn that is fully twisted under a high load (shown in the bottom left, with a HOF of 0.74). Also, the coiled yarn produced by the isobaric twist insertion process (top right) has a lower spring index (0.29) than does the coiled CNT yarn produced by the TOP process (0.79, shown in the bottom right). The calculated HOF as a function of applied twisting stress is shown in Figure S15a for the twisted yarn.

The above HOFs of the yarns were derived using the method exploited for determining the HOFs for forest-drawn sheets, except that the 2D-Fast Fourier Transforms (2D-FFT) were obtained from SEM images using MATLAB. The FFT images for a yarn twisted under a 3.3 MPa load and a 191 MPa load are shown in Figures S14c and S14d. The optimized domain size and magnification for calculating the HOF were 20 x 20 μm^2 and 2.22 (pixels/CNT diameter).

The peak power and average power at 1 Hz reached 305 and 75 W kg^{-1} (Figure S15b), respectively, compared with 80 and 22 W kg^{-1}, respectively, for harvesting at this frequency by previously reported isobarically prepared twistron[2]. While the peak power of the isobarically prepared twistron dramatically decreased for spring indices above 0.51, both the peak and average power of this TOP twistron increased with increasing spring index for the entire spring index range from 0.29 to 0.79 (Figure S15d). The reason is that an applied stress below 20.6 MPa is needed to obtain a spring index above 0.51 for isobarically prepared twistrons[2], which is insufficient to provide high CNT orientation during pre-coiling twist. On the other hand, the high stress applied during the twist insertion, pre-coiling part of the TOP generates this high CNT orientation (Figure S16). These results for TOP twistrons include the contribution from strains where snarling occurs, but Figure S17b shows that snarling contributes only about 10% of the total average power during harvesting, while it contributes about 30% to the total strain that can be used for harvesting (Figure S17a).

Figure S16b shows the strain dependence of the stress-induced volume change and capacitance change for a TOP yarn derived from a twisted yarn having a HOF of 0.69. Figure S16c shows the HOF dependence of the specific capacitance and specific volume for TOP yarns with 0% and 77 % total tensile strain. Using these results, Figure S16d shows the HOF dependence of the capacitance change and specific volume change in going from 0% to 77% total tensile strain. For these plots, the yarn volume and volume change were calculated from optical images of the coiled yarns. The less aligned yarns in Figures S16c and S16d had a higher specific volume and higher specific capacitance than highly aligned yarn. However, highly aligned yarn had a higher volume change and capacitance change than the less aligned yarn.

To investigate torsional energy harvesting by coiled twistrons without decrease of coiling, an 18.1-mm-length fully-coiled TOP CNT twistron was characterized in 0.1 M aqueous HCl electrolyte during isometric twist addition and untwist. The capacitance of the fully-coiled CNT twistron decreased by 20.63% when the inserted twist in the coiled yarn was increased by 11 turns cm^{-1} at a twist speed of 60 rpm. The OCV showed little variation when the twist speed was increased from 6 to 120 rpm, but the load resistance that maximized average power dramatically decreased from 15 to 1.42 kΩ, due to the decrease in capacitive impedance resulting from increased twist frequency.

The twist speed was optimized to maximize the torsional energy conversion efficiency for this coiled TOP CNT twistron. When the twist speed was increased from 6 to 120 rpm, the input mechanical energy reached a maximum of 2595 J kg^{-1} at a twist speed of 30 rpm, while the output electrical energy decreased from 101.1 to 30.7 J kg^{-1}. As a result, a maximum torsional energy conversion efficiency of 4.89% was obtained for a twist speed of 6 rpm (Figure S19a),

which was higher than obtained for sinusoidal stretch of a TOP twistron (Figure S18). However, the maximum electrical energy per cycle was higher for twistron stretch (213 J kg^{-1} for a 0.1 Hz sinusoidal stretch, without using a Pt wire current collector). Within the same twist speed range, peak power and average power for the coiled TOP CNT twistron reached a maximum of 3.41 and 1.53 W kg^{-1}, respectively, at a twist speed of 120 rpm, which were quite low because of the long times required for a twist cycle (Figure S19b), compared to a fast stretch cycle.

5. Biscrolled rGO@CNT harvesters

5.1 Raman and X-ray characterization

Figure S20 compares the Raman spectra of twisted pristine CNT yarn, 30 s ITAP-treated CNT yarn, GO nanoplates, GO@CNT yarn, and 30 s ITAP-treated rGO@CNT yarn. These results show the effects of processing conditions on the Raman I_G/I_D, which is the ratio of the Raman intensity of the G band (for the tangential vibrations of sp^2 carbons) to the intensity of the D band (due to disordered carbons). As a result of ITAP, the I_G/I_D ratio increases from 1.02 for the pristine yarn to 2.63 for the ITAP-treated yarn. Similarly, ITAP increases the I_G/I_D ratio from 0.93 for the GO@CNT yarn to 2.52 for rGO@CNT yarn. These increases in the I_G/I_D ratio caused by ITAP are consistent with the reduction of GO@CNT yarn and the removal of covalently bonded oxygen and amorphous carbon from the pristine CNT yarn, thereby increasing the perfection of the carbon phases[3]. The ITAP-produced pzc shifts are consistent with these results (from -80 mV for the pristine CNT yarn and above 300 mV for the GO@CNT yarn to about -210 mV for both ITAP-treated yarns (Figure S12).

The positive shift of the pzc for the neat MWNT yarn with respect to the pzc of the ITAP treated MWNT yarn is consistent with the existence of reacted oxygen on the surface of forest grown MWNTs, which is removed by ITAP. The presence of this oxygen has been established by previous x-ray photoelectron spectroscopy of sheets of forest-grown MWNTs[12], which deduced a total oxygen to carbon ratio of about 4%. A surface concentration of reacted oxygen could explain the 130 mV higher pzc for the neat yarn than for the ITAP yarn, since we have previously shown (*14*) that highly surface-oxidized MWNT yarns of forest-grown MWNTs (obtained by long nitric acid oxidation) have a large pzc (above 1 V vs. Ag/AgCl), as does the presently investigated 10 wt % GO@CNT yarn (above 0.3 V vs. Ag/AgCl). Since the pzc linearly depends on the work function, which is about equal for oxygen-free MWNTs and graphene[13], the nearly identical pzc for ITAP obtained rGO/MWNT and ITAP treated pristine yarn is consistent with ITAPs removal of oxygen from both. Taking 20% of the carbon in the MWNTs to be in the outer layers (from the average outer diameter and number of walls of the investigated MWNTs), the below quantum chemical calculations predict that a change in the surface O/C ratio by 1.05% to 1.11% would explain the pzc shift between the pristine and ITAP treated MWNTs (depending upon the exact ratio of epoxide to hydroxyl groups on the outer MWNT surfaces) (Figure S21). This is because loss of covalently bonded oxygen can provide the decrease in work function, which provides the negative shifts of pzc[14].

A bilayer graphene surface was used as the basis for all models because the work function of graphene is effectively identical to that of a large-diameter CNT[13]. Individual epoxy or hydroxyl groups were placed on the upper surface of the graphene bilayer in varying concentrations to provide the results shown in Figure S21. The work function for each model and oxygen concentration were calculated and compared to the pristine case. All calculations were performed using density functional theory (DFT), as implemented in the Vienna ab-Initio Simulation Package, using the projector augmented wave method. The Perdew-Berke-Ernzerhof

functional was used for the exchange-correlation functional, with a 520 eV cutoff for the plane-wave basis expansion. The surface functional groups were allowed to relax along with nearest neighbor carbon atoms, while the rest of the graphene surface was frozen. The interlayer spacing of the bilayer was fixed at 3.44 Å, which matches the measured value for MWNTs[15]. Electronic and ionic convergence criteria were set to 10^{-5} and 10^{-4} eV, respectively. DFT-D3 van der Waals correction[16] and surface dipole corrections were employed during all calculations.

The average nearest-neighbor inter-nanotube separation within a bundle was studied by SAXS. Figure 3a shows the SAXS patterns of the twisted pristine CNT yarn, 30 s ITAP-treated CNT yarn, GO@CNT yarn, and 30 s ITAP-treated rGO@CNT yarn. The scattering peak for a scattering vector (Q) of 0.078 Å^{-1} in the twisted pristine CNT yarn originates from the oriented CNTs and corresponds to an 8.07 nm separation between CNTs in a bundle. This distance between neighboring CNTs remains unchanged after 30 s of ITAP treatment. In GO@CNT yarn and 30 s ITAP-treated rGO@CNT yarn, there is a negative shift of the position of the SAXS peak, indicating that the existence of GO and rGO increases the average separation between neighboring CNTs in a bundle from 8.07 nm to 8.38 nm.

Figure 3b shows 2D images of WAXS results for the twisted pristine CNT yarn, 30 s ITAP-treated CNT yarn, GO@CNT yarn, and 30 s ITAP-treated rGO@CNT yarn. Consistent with SAXS observations, the CNT (002) peak shows that the CNTs are highly oriented for all of these samples. Figure S24 compares the WAXS patterns of GO@CNT yarn and 30 s ITAP-treated rGO@CNT yarn. The diffraction pattern for the GO@CNT yarn in Figure 3b, which shows the (001) peak from the GO platelets at 0.84 nm, indicates that the GO platelets are oriented parallel to the CNTs and to the axial direction of the twisted yarn. In the 30 s ITAP-treated rGO@CNT yarn, the GO (001) XRD feature disappears, indicating a complete reduction of GO by the 30 s ITAP treatment. Note that the (002) spacing for the rGO and CNTs overlap, so that separate peaks cannot be resolved.

5.2 The effects of decreasing twistron resistance on twistron performance

We discovered that twistron performance can be dramatically increased by biscrolling large lateral size graphene oxide (GO) platelets (Figure S25) between layers of neighboring CNT bundles and then reducing the GO to produce rGO. This improved performance results from the dramatically increased interactions between 1D nanotube bundles and 2D nanosheets compared with those between nanotube bundles (Figure 3c).

Further improvements in twistron performance result from the following considerations. The frequency dependence of output power can be described by a simplified *R-C* circuit. In this approximation[2], the total impedance of the harvester comprises the internal resistance of the yarn and the impedance of the yarn's double-layer capacitance ($Z_{harvester} = R_{internal} + 1/(j\omega C)$, where j is $\sqrt{-1}$ and ω is the angular frequency). Since the impedance due to capacitance inversely depends on frequency, it dominates at low frequencies, leading to the initial observed power output increase with increasing frequency (Figure 3d). For high frequency stretching, this capacitance impedance is negligible, and the internal resistance dominates, leading to a plateau in output power with further increased frequency.

Since the output power of a twistron harvester is limited by its impedance, incorporating a current collector with the coiled twistron yarn dramatically decreases its internal resistance, and thus increases the power and energy output (Figure 3d and Figure S22). Figure S26b compares EIS results for a rGO@CNT twistron and a rGO@CNT twistron wrapped with a 25-µm-diameter Pt wire current collector. The Nyquist plots of Figure S26b indicate that incorporating a Pt wire decreases the ohmic resistance and the charge transfer resistance. After incorporating the Pt wire

current collector, the maximum gravimetrical peak power and average power both increase by a factor of ~1.5, when ignoring the Pt wire's weight.

Similarly, biscrolling highly-conducting silver nanowires into a CNT twistron harvester reduces the internal resistance and increases the power and energy output. As shown in Figure S27, biscrolling 15 wt % of 35-nm-diameter Ag nanowires, increases the maximum peak power in the plateau region at high frequencies from 0.81 to 1.14 kW kg^{-1} and the maximum energy per cycle from 130 to 158 J kg^{-1} at 0.1 Hz.

5.3 The effect of applying an external bias voltage on twistron harvesting in 0.1 M HCl aqueous electrolyte

The ITAP shifts the pzc (relative to Ag/AgCl reference electrode) from -80 mV for the coiled pristine yarn to -210 mV for the coiled ITAP yarn. Since coiling part of this process does not significantly change the pzc, the shift is almost entirely due to ITAP. The pzc for the ITAP rGO@CNT coiled yarn (-215 mV) is similar to that of the coiled ITAP CNT yarn. The ITAP-produced shift in pzc increases the amount of charge injection that results from the self-biasing of the twistron by electrolyte doping. Partially as a consequence of this increased self-bias charging as a result of ITAP, the open circuit potential of the coiled rGO@CNT twistron yarn (vs. Ag/AgCl) increased with increasing strain from 0.40 V to 0.78 V during 46% stretch. An additional applied bias voltage (and the corresponding increased injected charge) can increase the net energy (output energy, reduced by the input energy required for electrical biasing) that can be harvested. Figure S28 shows the effect of applying an external bias voltage between the counter electrode and the coiled rGO@CNT twistron harvester working electrode while a 0.25 Hz sinusoidal stretch of 46% was applied. These results show that the per-cycle net output electrical energy increased from 140 J kg^{-1} for no externally applied bias to 285 J kg^{-1} when an external bias of 400 mV was applied. Further increase of the bias voltage decreased the net energy harvested, due to increased electrolytic losses, which limited the opportunity to more dramatically improve performance in this aqueous electrolyte.

5.4 Energy conversion efficiency of coiled rGO@CNT twistron harvesters

Simultaneous measurements of tensile mechanical energy input and electric energy output during cycling of a rGO@CNT twistron yarn at 0.1 Hz in 0.1 M HCl show that the energy conversion efficiency increases with increasing applied strain and reaches a peak of 3.55% at 44% strain (Figure S29). Increasing the cycling frequency to 0.25 Hz decreases the input mechanical energy compared with that for the same applied strain at 0.1 Hz. This increase in cycling frequency increases the energy conversion efficiency to 3.89% for a 48% strain (Figure S30). Further substantial increase of the stretch frequency results in increased hysteresis in the force-strain curve, which increases mechanical energy loss and decreases efficiency.

As discussed above, applying an external bias voltage can further increase the net energy harvested per cycle, and thus increase the mechanical-to-electrical energy conversion efficiency. Figure S31a shows that the net harvested energy monotonically increases with increasing applied strain when an inter-electrode voltage of 400 mV was applied. Figure S31b indicates that the energy conversion efficiency for this applied voltage initially increases with increasing applied strain, reaches a peak of 4.85% for 34% strain, and then plateaus with further increased applied strain.

5.5 rGO@CNT twistron harvester in an organic electrolyte (0.1 M LiBF$_4$ in acetonitrile)

Since organic electrolytes have broader electrochemical windows than do aqueous electrolytes, we wondered if further improvement in twistron harvester performance could be obtained by using an organic electrolyte and an applied bias voltage. Figure S38 shows a peak

OCV of 190 mV and a plateau of peak power of 340 W kg^{-1} (above 8 Hz), for a rGO@CNT twistron stretched to 48% in 0.1 M LiBF$_4$ in acetonitrile. The capacitance of a coiled rGO@CNT twistron harvester in 0.1 M LiBF$_4$/acetonitrile organic electrolyte (12.6 F g^{-1}, Figure S38a) is much larger for this harvester in 0.1 M HCl aqueous electrolyte (7.8 F g^{-1}). However, for the same applied strain (48%), the capacitance change in this organic electrolyte (22%) is much smaller than in the aqueous electrolyte (~65%). Hence, the peak OCV of 190 mV in this organic electrolyte (Figure S38b) is smaller than in the aqueous electrolyte (340 mV, Figure 3c). This low OCV, as well as the low ionic conductivity of the organic electrolyte, decreases the electrical power and energy output per cycle (Figure S38c) compared with that for the aqueous electrolyte. A maximum peak power of 340 W kg^{-1} at 8 Hz, and a maximum energy per cycle of 48 J kg^{-1} at 0.1 Hz were achieved for a rGO@CNT twistron stretched to 48% in 0.1 M LiBF$_4$ in acetonitrile (Figure S38d), which are much smaller than realized for the same yarn and the same stretch in 0.1 M HCl (Figure 3d). Applying a 600 mV bias voltage increased the net energy harvested per cycle from 47 to 179 J kg^{-1} during a 48% stretch at 0.25 Hz. However, further increase of the bias voltage decreased the net energy harvested, due to self-discharge losses (Figure S39).

5.6 rGO@CNT twistrons in 0.6 M NaCl aqueous electrolyte for ocean wave harvesting

For potential use of our twistrons for harvesting ocean wave energy, rGO@CNT harvesters were tested in 0.6 M NaCl solution, a typical salt concentration of seawater. Figure S40a shows the load resistance dependence of peak voltage, peak power, and energy per cycle for a coiled rGO@CNT twistron yarn for a 1 Hz, 48% sinusoidal stretch in this electrolyte. A maximum peak power of 169 W kg^{-1} and a maximum energy per cycle of 49 J kg^{-1} were obtained for this deformation and load resistances in the range of 350-400 ohm. In addition, harvester performance in 0.6 M NaCl varies little for temperatures between 0 to 60 °C (Figure S40b), which is important for the use of these harvesters in varying temperature oceans.

6. The effects on performance of tuning the tensile strain profile during a mechanical cycle

We found that we can increase the peak power and the average power for low frequency deformations (between 0.2 Hz and 4 Hz) by transitioning from a sinusoidal stretch-and-release to a square-wave stretch-and-release (Figure S41). We first focus on this effect for TOP yarns. The peak power (Figure S42) slightly decreases with increasing frequency in this range for square-wave deformation, because there is insufficient time for complete charge transfer when the transition occurs between yarn stretch and stretch-release. In contrast, due to decreased twistron impedance with increased sinusoidal frequency, the maximum peak power is obtained at high frequencies for a sinusoidally applied strain (Figure S42). At all frequencies, the load resistance that maximizes peak power and average power coincide for a sinusoidal stretch. However, for low frequencies, the load resistance that maximizes peak power is lower than the load resistance that maximizes average power for square-wave deformations. At these low frequencies, both of these resistances are lower than the load resistance that maximizes both peak power and average power for a sinusoidal stretch (Figure S41c).

Figure S43a shows that the peak voltage for both stretch and stretch-release increases with increasing applied strain for a 0.2 Hz square-wave stretch in 0.1 M aqueous HCl. The results of Figure S43b show that both the ratio of the peak voltage for stretching to the peak voltage for stretch-release and the ratio of average power for stretching to the average power for stretch-release quasi-monotonically increase with increasing strain. Figure S43c provides the dependence of the peak power and peak power optimizing load resistance on the applied strain.

Figure S44a shows that the open-circuit potential slightly decreases with time after square-wave stretch and requires time to return to the original unstrained potential after stretch-release. This time dependence corresponds to that required to extrude electrolyte during yarn elongation and suck electrolyte into the yarn when strain is removed, as well as the related time required for the electrolyte embedded yarns to equilibrate structure with the applied strain. Figure S44b shows that the peak OCVs for both sinusoidal and square-wave deformations rapidly decrease with increasing cycle frequency and that the peak OCV becomes lower for square-wave deformations than for sinusoidal deformations for frequencies above about 8 Hz. These results also relate to the time required for the yarns capacitance to fully decrease upon stretch. Figure S44c shows for 1 Hz deformations that the load resistance that maximizes peak power and average power (1000 ohm) is the same for sinusoidal deformations, and is lower for peak power (200 ohm) than for average power (500 ohm) for square-wave deformations. These lower resistances for the square-wave deformation than for the sinusoidal deformation result from the lower impedance of the twistron energy source for square-wave than for sinusoidal deformations of the same frequency. These results show that the peak power (1128 W kg^{-1}) and average power (212 W kg^{-1}) at 1 Hz are much larger than those at the same frequency for sinusoidal deformations (361 and 132 W kg^{-1}, respectively). Figure S44d shows that similar low frequencies (0.1 to 4 Hz) provide enhancements of peak power and average power for a rGO@CNT twistron when a sinusoidal stretch is changed to a square-wave stretch having the same frequency and strain (48%). The square-wave peak power increases with increasing frequency until reaching a maximum value at 1 Hz (996 W kg^{-1}), while the average power increases with increasing frequency. Hence, the peak power of a sinusoidal deformation becomes higher than for a square-wave deformation at frequencies above 4 Hz. The average power is also higher for a square-wave deformation than for a sinusoidal deformation for frequencies below 4 Hz. For frequencies above 4 Hz, the average power is similar for both the square-wave and sinusoidal deformations and only slightly increases with increasing deformation frequency.

7. Dual harvesting electrode twistrons, solid-state twistrons, and twistron applications

7.1 A dual-electrode twistron harvester comprising a mandrel-coiled homochiral yarn working electrode and a mandrel-coiled heterochiral yarn counter electrode

To produce harvesters that generate electricity from the deformation of both electrodes, we used mandrel-coiled homochiral and heterochiral yarns as working and counter electrodes. Figure S45a shows the capacitance and the peak open-circuit voltage versus strain for the homochiral and heterochiral twistron yarns that are coiled around a rubber fiber (as described in Section 1.1). Stretching a homochiral coiled yarn decreases yarn capacitance, thereby increasing the OCV with respect to a non-stretched counter electrode. Capacitance changes and voltage changes occur for a heterochiral yarn that are opposite to these results for a homochiral yarn. Figure S45b shows these potential changes when stretching a homochiral and heterochiral yarns at 1 Hz to 150% strain. The corresponding oppositely directed electrode potential changes enables a harvester comprising parallel, simultaneously stretched homochiral and heterochiral yarn electrodes, in which the output voltages are additive (Figure S45b).

7.2 A dual-electrode solid-state twistron harvester comprising a self-coiled rGO@CNT yarn working electrode and a mandrel-coiled heterochiral CNT yarn counter electrode

Except for harvesting the energy of ocean waves, or possibly harvesting energy within the human body, eliminating the electrolyte bath is important for many applications of our twistron harvesters. Ideally, both device electrodes should be twistron yarns that are combined in a single

yarn that is a solid-state harvester, like for the devices of Figure 4f and Figure S45b. As described in Section 1.1, homochiral and heterochiral electrodes in dual-electrode yarns were electronically insulated, while ionically connected, by overcoating and connecting these yarns with a 10 wt % PVA/0.1 M HCl gel electrolyte.

Figure S46 shows the performance (for a sinusoidal stretch to 38% strain at 1 Hz) of a dual-electrode solid-state twistron harvester that has a special structure, compared with our usual dual-electrode harvesters that consist of parallel homochiral and heterochiral rubber-mandrel-wrapped twistrons. A self-coiled rGO@CNT yarn working electrode is at the yarn center and a heterochiral CNT yarn counter electrode is coiled around this rGO@CNT yarn. This use of the homochiral yarn as the mandrel for the heterochiral yarn eliminates the need for a rubber mandrel to avoid twist cancellation in the heterochiral yarn. The direct benefit of such a configuration is that the energy consumed by stretching the rubber mandrel is eliminated. One single solid-state harvester of this type (with a total weight of 1.6 mg, including the electrolyte, and a total weight of 0.28 mg for the CNT and rGO) generates a peak OCV of 188 mV and SCC of 201 µA when sinusoidally stretched by 38% at 1 Hz. As shown in Figure S46, multiple harvesters of this type can be connected either in-series or in-parallel to provide arbitrarily high voltages and currents, respectively.

7.3 A solid-state twistron harvester as a self-powered tensile strain sensor for sign language recognition

The results of Figure S45b indicate that the stretch-induced change in OCV from a homochiral twistron is substantially larger than for a heterochiral twistron. Hence, most of the voltage output from the above dual-electrode solid-state harvesters originate from the homochiral electrode. Figure S47a shows that the OCP and capacitance for this electrode approximately linearly change with the applied strain. Figure S47b shows that the OCV for the dual-electrode harvester of Section 7.2 is also approximately linearly dependent upon the applied strain. This feature is useful for the application of these dual-electrode devices as self-powered strain sensors.

Figure S48 demonstrates the application of these dual-electrode solid-state harvesters as self-powered strain sensors. These sensors were sewn into a glove and used for recognizing sign language. Based on the output OCV profiles, different letters and phrases of American sign language hand gestures can be easily differentiate. This is promising for applications like sign-to-speech translation.

7.4 A one-body dual harvesting electrode twistron that uses a seesaw structure

Figure S49a shows the configuration of a one-body, dual-electrode harvester that uses seesaw-like deformations of two 10-mm-long twistrons in a linear twistron array to generate a higher output voltage than can a single stretched electrode twistron harvester. The one body comprises two twistron yarns having the same homochiral structure that are mechanically end-connected, but electronically separated. By applying a displacement in the yarn direction to the insulating segment that separates these two twistron yarns, while torsionally and translationally tethering the opposite ends of each twistron, one yarn is stretched and the other yarn expands, thereby providing opposite voltage changes.

Each harvester electrode was fabricated by cone spinning (using the TOP method) a coiled twistron yarn from a 40-mm-wide stack of three forest-drawn CNT sheets. By mechanically connecting the top and the bottom of each electrode yarn through an insulating 3-mm-long glass-tube, a one-body structure was formed that comprises two twistrons. During harvesting, the extreme ends of the one-body dual-twistron yarn were fully tethered. Moving the center of the one-body harvester causes one twistron electrode to contract in length, while the other twistron

19

yarn expands (Figures S49a and S49b, top). After a few cycles of training, both twistron electrodes have nearly identical snarled structures (corresponding to a strain of -23.1%) and identical lengths (1.3 cm) before displacement of the glass-tube interconnect that electronically separates and mechanically connects these twistrons. Hence, the OCVs of these electrodes are 180° out-of-phase, which optimizes energy harvesting. The electrolyte was 0.1 M aqueous HCl and a total strain of 123% was applied to each electrode by a 1 Hz sinusoidal deformation. Of this 123% total strain, -85% strain was for the strain range where snarling occurs. The output OCV was about two times higher than for the case where only one electrode was stretched, as shown in Figure S52a (inset).

Figure S49c shows parallel-connected one-body harvesters that use the seesaw structure. The centers of the two one-body harvesters were simultaneously stretched. By connecting two equivalent one-body harvesters in parallel, the peak-to-peak SCC was increased to twice that for a single one-body harvester, as shown in Figure S52a. Figure S49d shows the frequency dependencies of the peak power and the average power for a dual-electrode one-body harvester, and compares this output with that obtained for two parallel connected identical harvesters.

The benefit of reducing input mechanical energy can also be realized for a harvester that is driven by rotational input mechanical energy by using the Scotch yoke of Figure S51a, left. Rotation of plate of the scotch yoke structure changes the length of the twistrons (Figure S51a, right). These twistrons were fabricated by the TOP method, using a 192 MPa stress during twisting and a 6.7 MPa stress during coiling. The weight of each of the single CNT electrodes was 42 μg and the length and diameter of these electrodes were 12 mm and 47 μm. Before displacement that results in unequal lengths for harvester yarns of opposite electrodes, the applied tensile strain in these electrodes were 10%, and no snarling was produced as each electrode underwent 20% strain during rotation of the mechanical drive. The peak-to-peak open circuit voltage of the harvester was 239 mV. The results in Figure S51b show that peak power, average power, and load resistance versus frequency for the 10-sets of seesaw structure yarns that were connected in parallel. Note that the average power increasing with increasing rotation frequency until a plateau is reached at above 4 Hz.

7.5 The low sensitivity of twistron performance in a highly conducting electrolyte (0.1 M aqueous HCl) to the separation between opposite electrodes

The results in Figure S50 show that the peak power and average electrical power output of the above 10-mm-long twistron harvesters are insensitive to the lateral (Figure S50a, c) and longitudinal separation (Figure S50b, d) between a stretched twistron electrode and an identical non-stretched twistron counter electrode when a highly conducting electrolyte is used.

7.6 Use of a one-body seesaw structure dual harvesting electrode twistron to demonstrate that the weight of a non-stretched counter electrode can be ignored in obtaining gravimetric power densities

We have so far ignored the weight of a non-stretched counter electrode when deriving the power density of our twistron harvesters. Using our highest performing twistron harvesters, which are rGO@CNT yarns obtained by ITAP, we here show that a one-body seesaw structure provides the same gravimetric power density when counting the weights of both electrodes as does a single harvesting electrode harvester when counting only the weight of the stretched electrode. Figure S53a shows the configuration of the seesaw structure harvester, where the top twistron electrode is contracting as an equivalent twistron bottom electrode is elongating. We will compare the harvesting ability of this seesaw structure harvester with that of a single stretched electrode harvester that uses an identical single twistron electrode and a large

capacitance, non-stretched counter electrode. The results of Figures S53c and S53d show that the peak-to-peak open circuit voltage of the single electrode harvester (293 mV) is half that of the dual electrode seesaw structure harvester and that the short circuit current of the single electrode harvester (909 µA) is nearly the same as that of the dual electrode seesaw structure harvester. Most importantly, the results in Figure S53e for both devices show that at all frequencies the average gravimetric power output is essentially identical when only the weight of the harvesting electrode is counted.

7.7 Powering electronic devices using series connected ITAP CNT harvesters that charge a capacitor

These demonstrations show the practical importance of transitioning from our previously investigated CNT twistrons[2] to our new ITAP CNT twistron. Four 4.5-cm-long coiled ITAP CNT harvesters were connected in series and used to charge a 220 µF capacitor to 0.6 V using 30 stretch-release cycles to 40% strain. Before rectification of the harvester output (using a Schottky diode full-bridge rectifier) the peak-to-peak OCV was between -0.2 and 0.8 V. The total mass of the harvesters was only 2.3 mg.

Rather than directly charging the capacitor using the rectified harvester output, as shown in Figure S54c, it is faster and more efficient to use a self-powered booster circuit (LTC 3108) to increase the voltage of the capacitor to 3.3 V (Figure S54d). Using the booster circuit meant that the capacitor could be charged to 0.6 V using only about 3 stretch-release cycles, while 30 cycles were required to charge the capacitor to this voltage without the booster circuit. Using this circuit, 21 stretch-release cycles charged the capacitor to 3.3 V. The 2.3 mg of harvester and relatively small number of stretch-release cycles was able to charge the capacitor to 5.45 mJ of electric energy, which was used to power five 2.75 V, 55 mW blue LEDs for 1 minutes before the LEDs stop emitting light. This capacitor-stored energy, from a 2.3 mg of twistron harvesters, can be also used to power various sensors. For example, this same energy as used to power five LEDs was used to power a temperature and relative humidity display device (having a 4.5 by 5.5 cm liquid-crystal-display) for 2.5 minutes. If the 2.3 mg harvester array was stretched by 40% 4 times every second, continuous operation of the temperature/humidity display device was maintained.

Figures
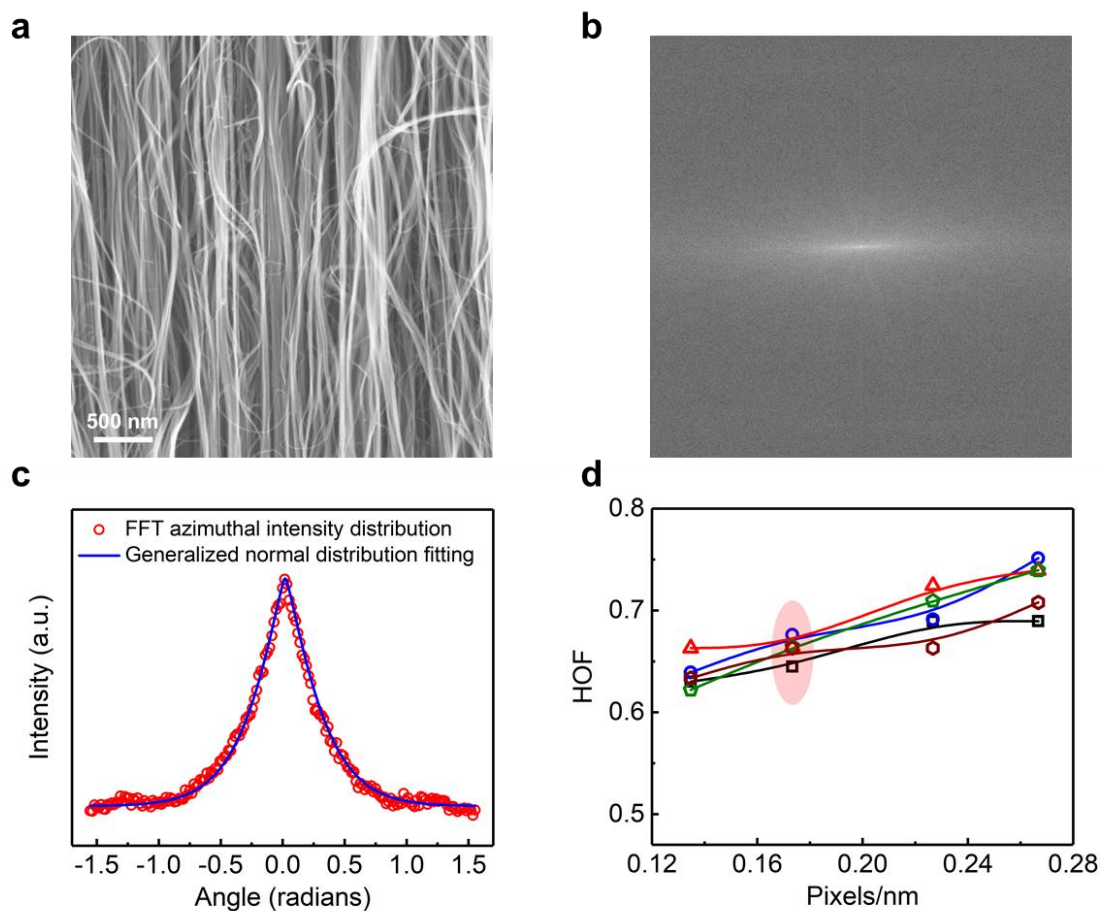
Figure S1. The analysis used for determining the Herman's orientation factor (HOF). a. Secondary electron SEM image at ×20 K magnification. **b.** The FFT power spectrum of (a). **c.** The azimuthal orientation distribution function from (**b**). **d.** The HOF calculated for four magnifications (expressed as pixels/nm) and five randomly selected areas in a forest-drawn CNT sheet. A magnification of 0.173 pixels/nm provides the best agreement in HOF for the randomly selected areas.
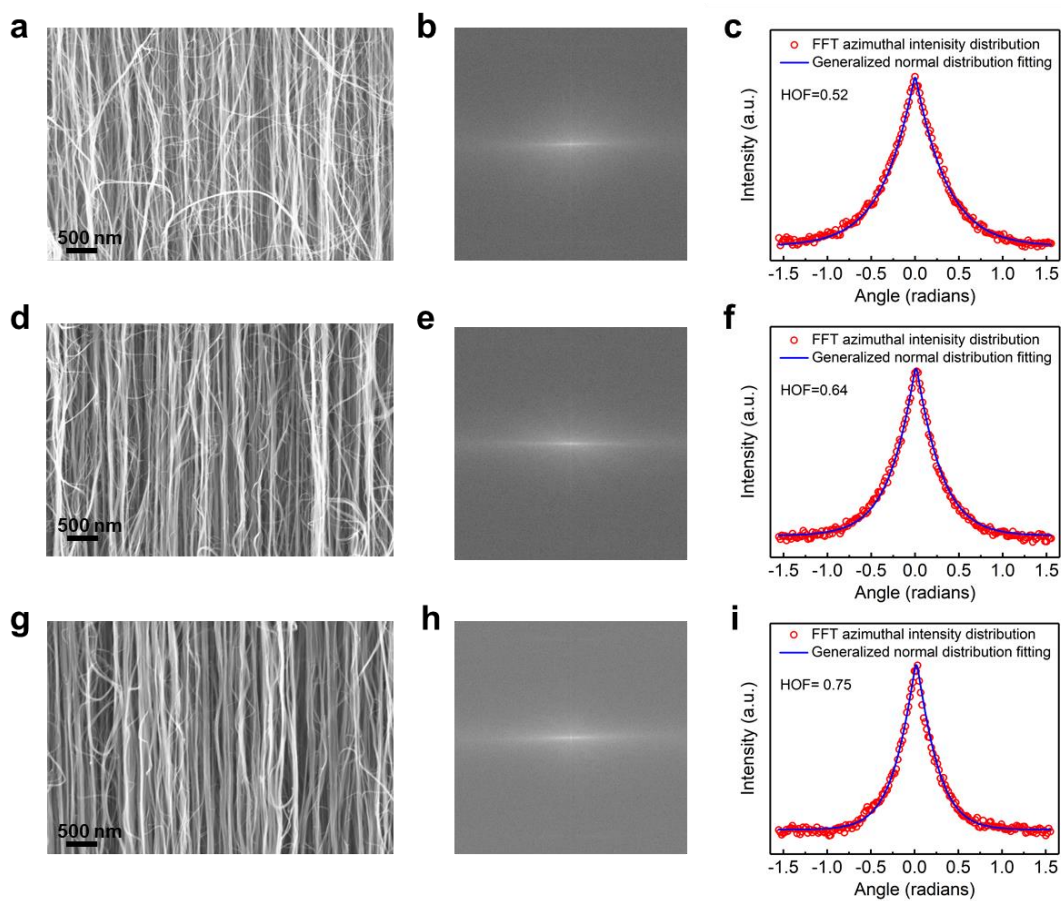
Figure S2. a-i. The SEM images, FFT power spectrums, and azimuthal orientation distribution functions for forest-drawn CNT sheets having a HOF of 0.52 (a-c), 0.64 (d-f), and 0.71 (g-i).
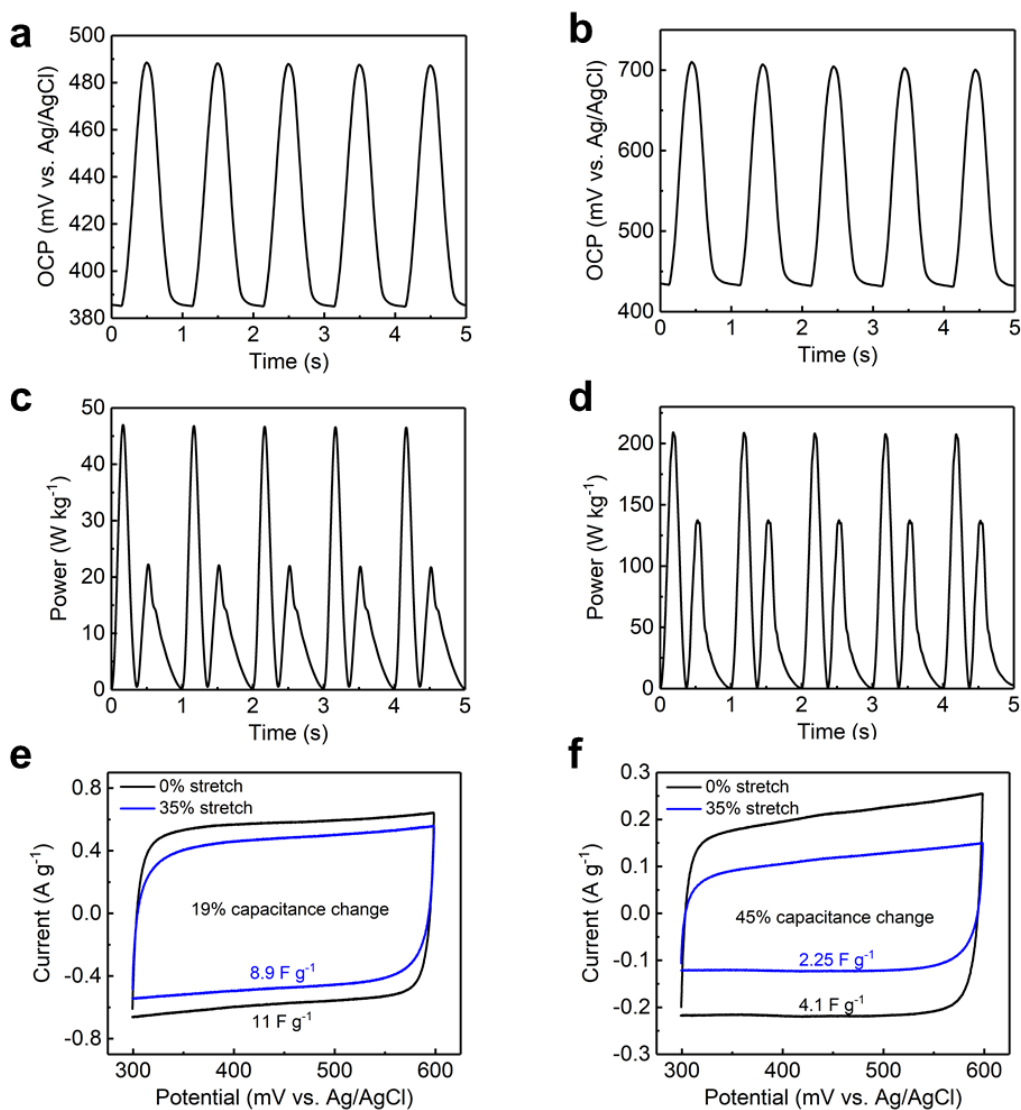
Figure S3. a-b. The time dependencies of the open circuit potential during a 1 Hz, 35% stretch for coiled CNT harvesters fabricated from precursor sheets having a HOF of 0.49 (a) and 0.64 (b). **c-d.** The time dependencies of power output during a 1 Hz, 35% stretch for coiled CNT harvesters fabricated from precursor sheets having a HOF of 0.49 (c) and 0.64 (d). **e-f.** CV measurements showing the capacitance change for 35% stretch for coiled CNT harvesters fabricated from precursor sheets having a HOF of 0.49 (e), and 0.64 (f).
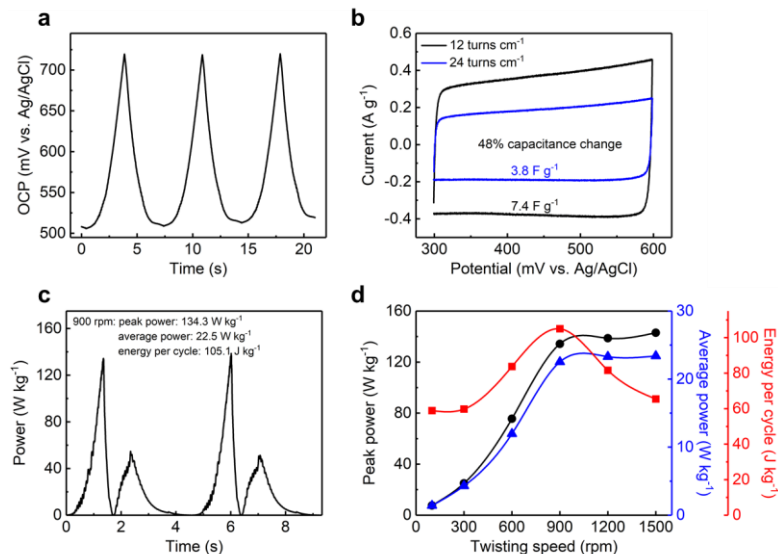
Figure S4. Energy harvesting by isometric twist and untwist for yarns made from forest-drawn CNT sheets having a HOF of 0.64, which are in the performance plot of Fig. 1e. a. OCP versus time during twist and untwist between a twist density of 12 turns cm^{-1} and 24 turns cm^{-1}. **b.** CV curves and corresponding capacitances for twistron having a twist density of 12 turns cm^{-1} and 24 turns cm^{-1}. **c.** Power output during twist insertion and twist release at 900 rpm. **d.** The dependence of peak power, average power and energy per cycle on twist speed. Supplementary Figs. 5 and 6 provide corresponding results for precursor sheets having HOFs of 0.58 and 0.52, respectively.
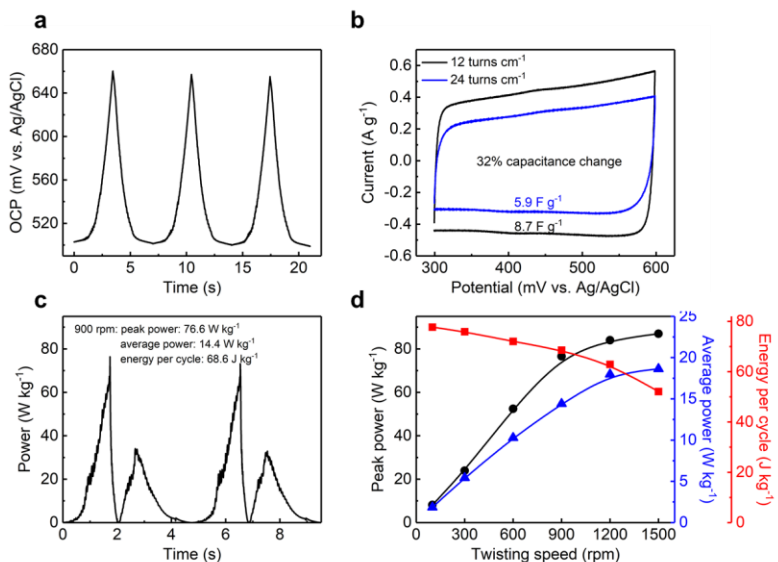
Figure S5. Energy harvesting by isometric twist and untwist for yarns made from forest-drawn CNT sheets having a HOF of 0.58, which are in the performance plot of Fig. 1e. a. OCP versus time during twist and untwist between a twist density of 12 turns cm^{-1} and 24 turns cm^{-1}. **b.** CV curves and corresponding capacitances for twistron having a twist density of 12 turns cm^{-1} and 24 turns cm^{-1}. **c.** Power output during twist insertion and twist release at 900 rpm. **d.** The dependence of peak power, average power and energy per cycle on twist speed.
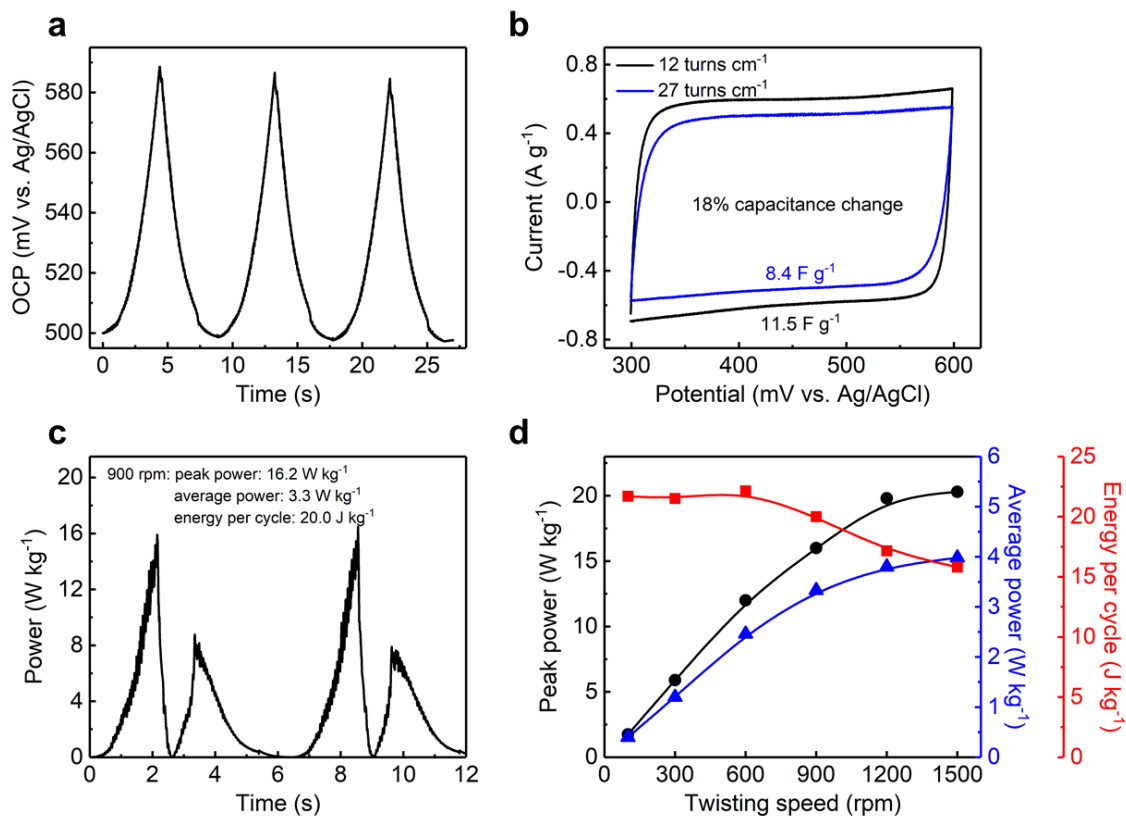
Figure S6. Energy harvesting by isometric twist and untwist for yarns made from forest-drawn CNT sheets having a HOF of 0.52, which are in the performance plot of Fig. 1e. a. OCP versus time during twist and untwist between a twist density of 12 turns cm^{-1} and 27 turns cm^{-1}. **b.** CV curves and corresponding capacitances for twistron having a twist density of 12 turns cm^{-1} and 27 turns cm^{-1}. **c.** Power output during twist insertion and twist release at 900 rpm. **d.** The dependence of peak power, average power and energy per cycle on twist speed.
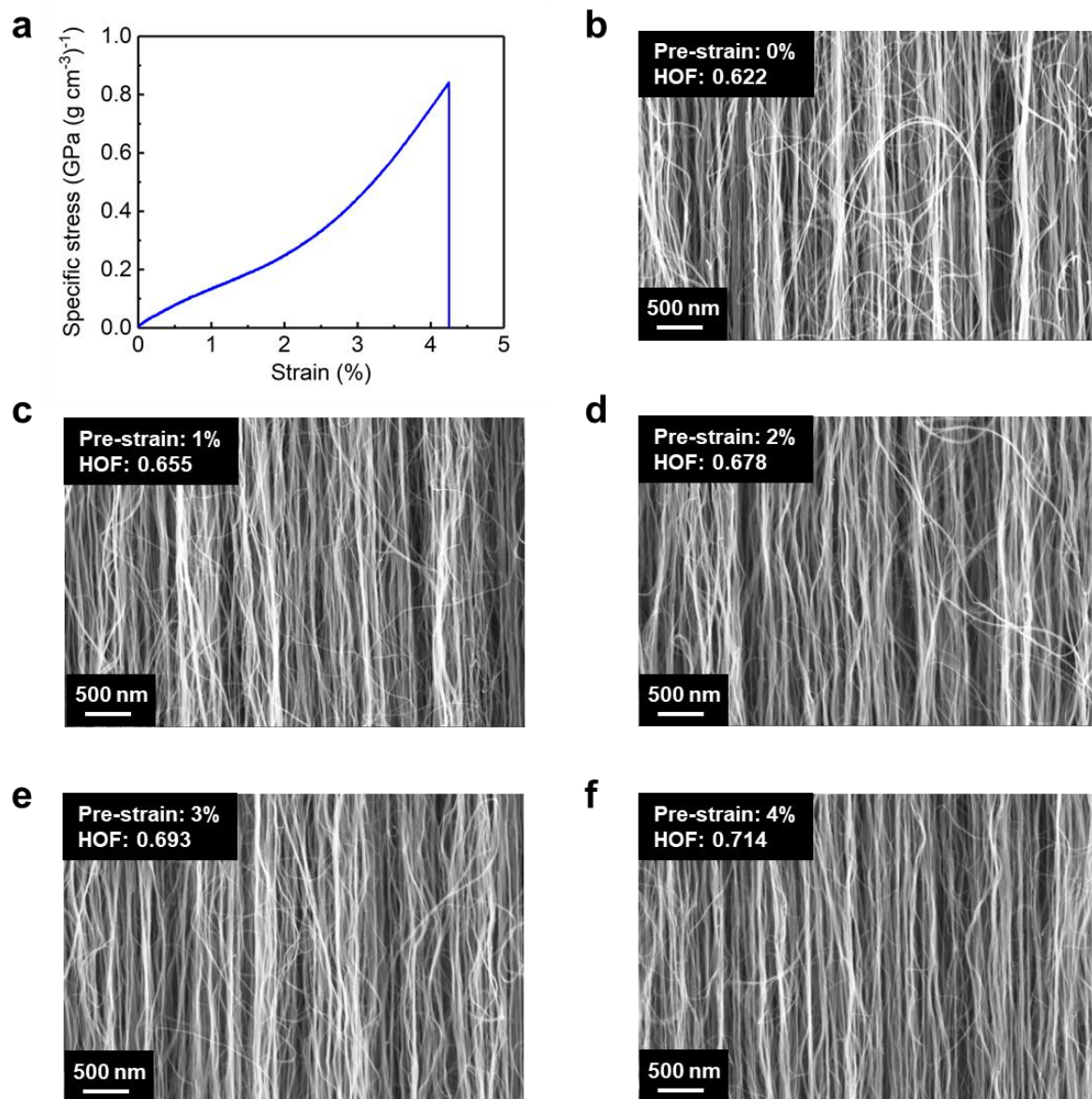
Figure S7. a. A density normalized stress-strain curve in air for a twisted CNT yarn (with bias angle of 22˚). **b-f.** SEM micrographs showing the increase in CNT alignment on the surface of twisted yarns as a function of the irreversible component of applied pre-strain.
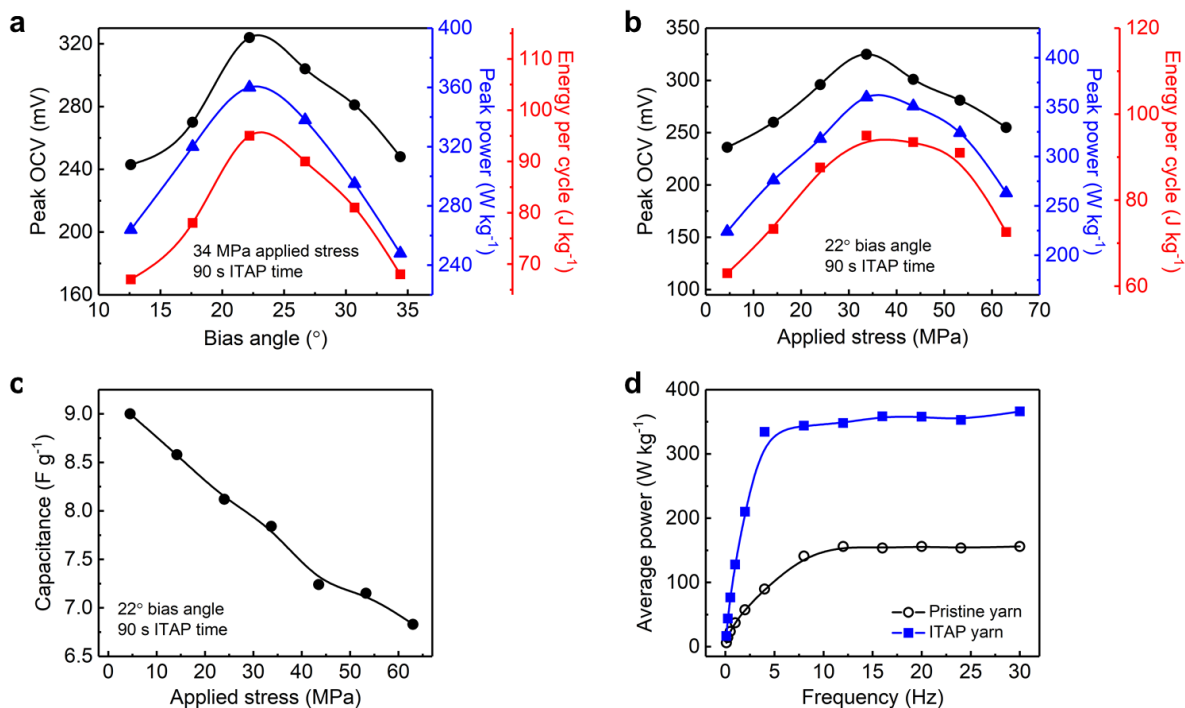
Figure S8. The performance of coiled CNT harvesters in 0.1 M aqueous HCl electrolyte as a function of the yarn's bias angle and the applied stress during ITAP. a. The dependencies of peak OCV, peak power, and energy per cycle on yarn bias angle during ITAP for a 1 Hz, 45% stretch of coiled harvesters. **b.** The dependencies of peak OCV, peak power, and energy per cycle on the applied stress during ITAP for a 1 Hz, 45% stretch of coiled harvesters. **c.** The dependence of the capacitance of fabricated coiled twistron yarn on the stress applied during ITAP to the twisted yarn. **d.** The frequency dependence of average power for CNT twistron harvesters before and after ITAP.
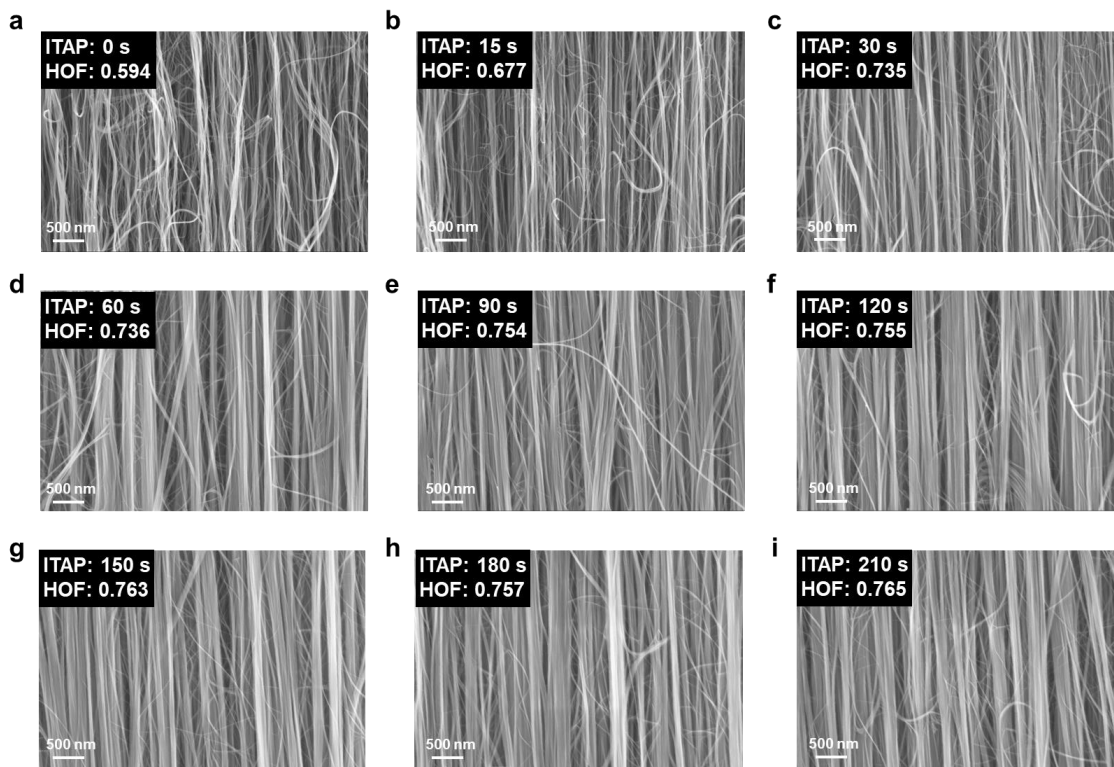
Figure S9. SEM micrographs showing the evolution of structure as a function of ITAP annealing time for a twisted yarn (with an initial bias angle of 22˚) when annealed under 34 MPa stress. The vertical direction for these micrographs is approximately the average alignment direction, and not the axial direction of the twisted yarn.
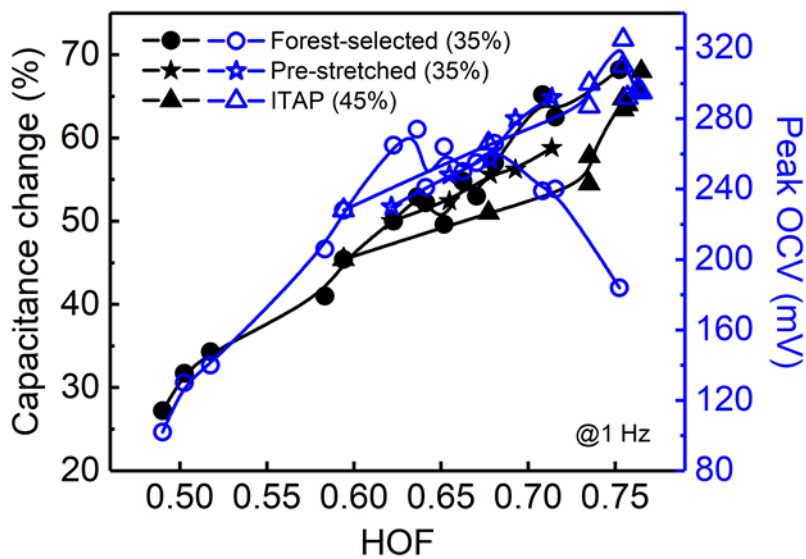
Figure S10. The HOF dependencies of capacitance change and peak OCV for three differently processed twistron yarns.
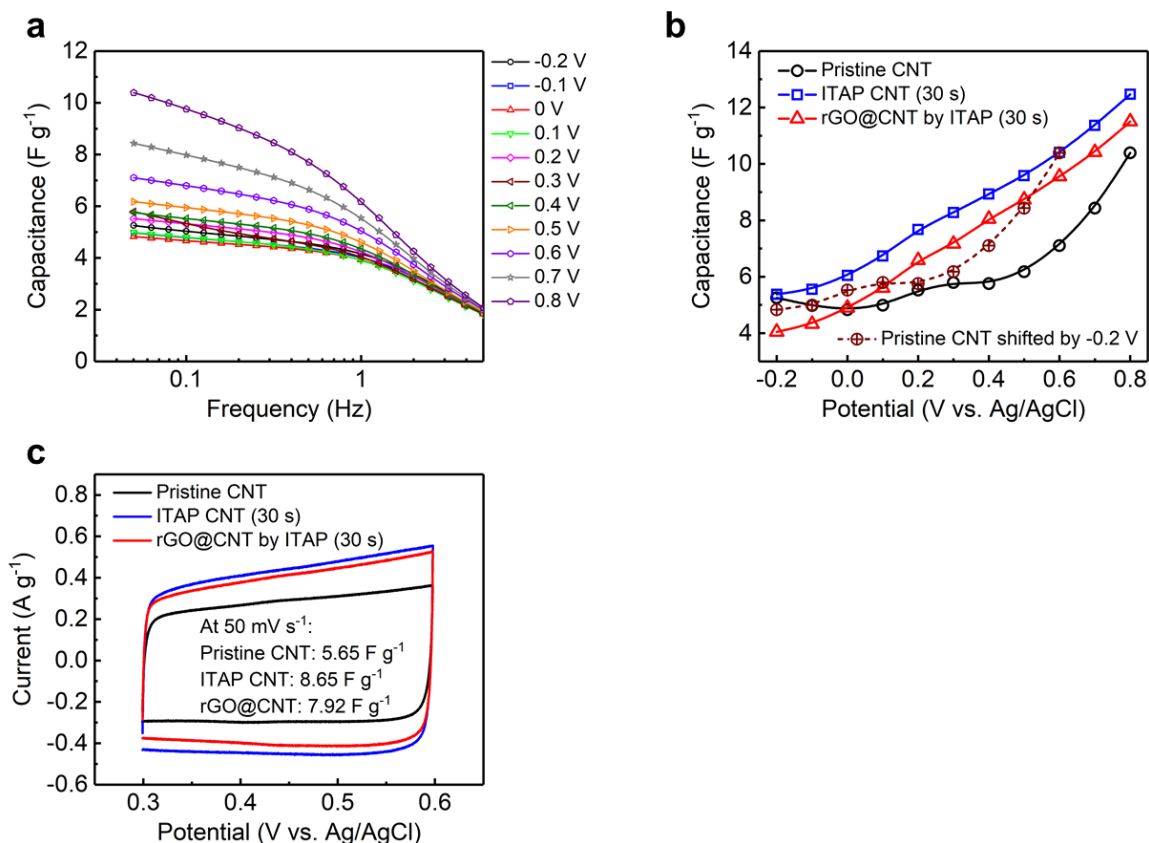
Figure S11. Electrochemical impedance spectroscopy (EIS) for self-coiled twistrons. a. Capacitance versus frequency for different twistron potentials (versus Ag/AgCl) for a pristine coiled CNT twistron. **b.** The dependence of twistron capacitance on applied potential (at a frequency of 50 mHz) for a pristine CNT yarn, ITAP CNT yarn, and rGO@CNT biscrolled yarn. For the results of (a) and (b), the EIS measurements were conducted at different applied potentials (versus an Ag/AgCl reference electrode), by using a potential amplitude of 10 mV and a frequency range of 50 mHz to 100 kHz. Prior to starting the frequency scan, the yarn was pre-conditioned at the applied potential until the current was below 0.5 µA. **c.** CV curves and corresponding capacitances for a pristine CNT yarn, ITAP CNT yarn, and rGO@CNT biscrolled yarn for a potential range of 0.3-0.6 V and a scan rate of 50 mV s⁻¹.
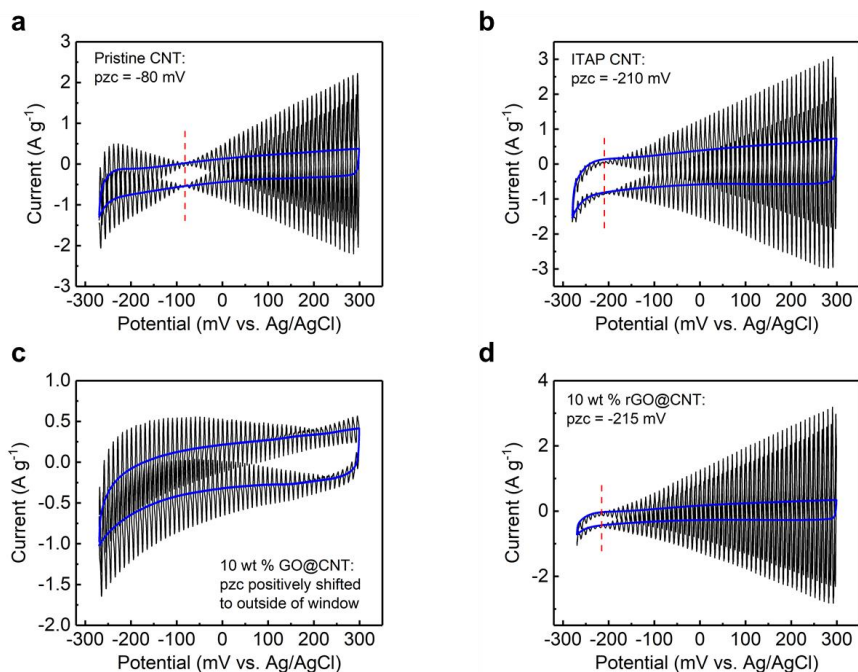
Figure S12. Piezoelectrochemical spectroscopy (PECS) measurements for (a) pristine CNT coiled yarn, (b) ITAP CNT coiled yarn, (c) 10 wt % GO@CNT coiled yarn, and (d) A coiled ITAP thermally reduced 10 wt % rGO@CNT yarn. The ITAP treatment time was 90 s. These PECS measurements are for a potential scan rate of 50 mV s^{-1} and a sinusoidal strain of 10% at 5 Hz (black). The blue curves are for a CV scan without an applied deformation.
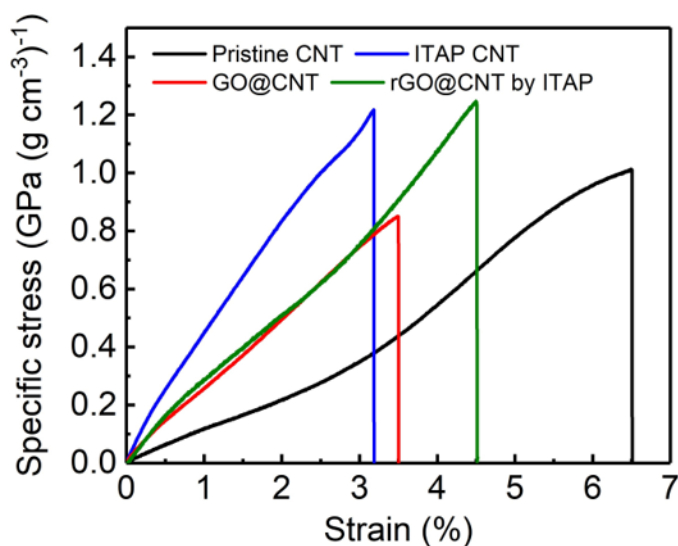
Figure S13. Density normalized stress-strain curves for a twisted pristine CNT yarn (with a bias angle of 22˚), a twisted CNT yarn after ITAP (for 90 seconds under 34 MPa load), a twisted 29 wt % GO@CNT yarn (with a bias angle of 22˚), and a twisted reduced rGO@CNT yarn obtained by ITAP (for 90 seconds under 34 MPa load). These measurements are for a gauge length of 13 mm and a strain rate of 0.1 mm min^{-1}.

31
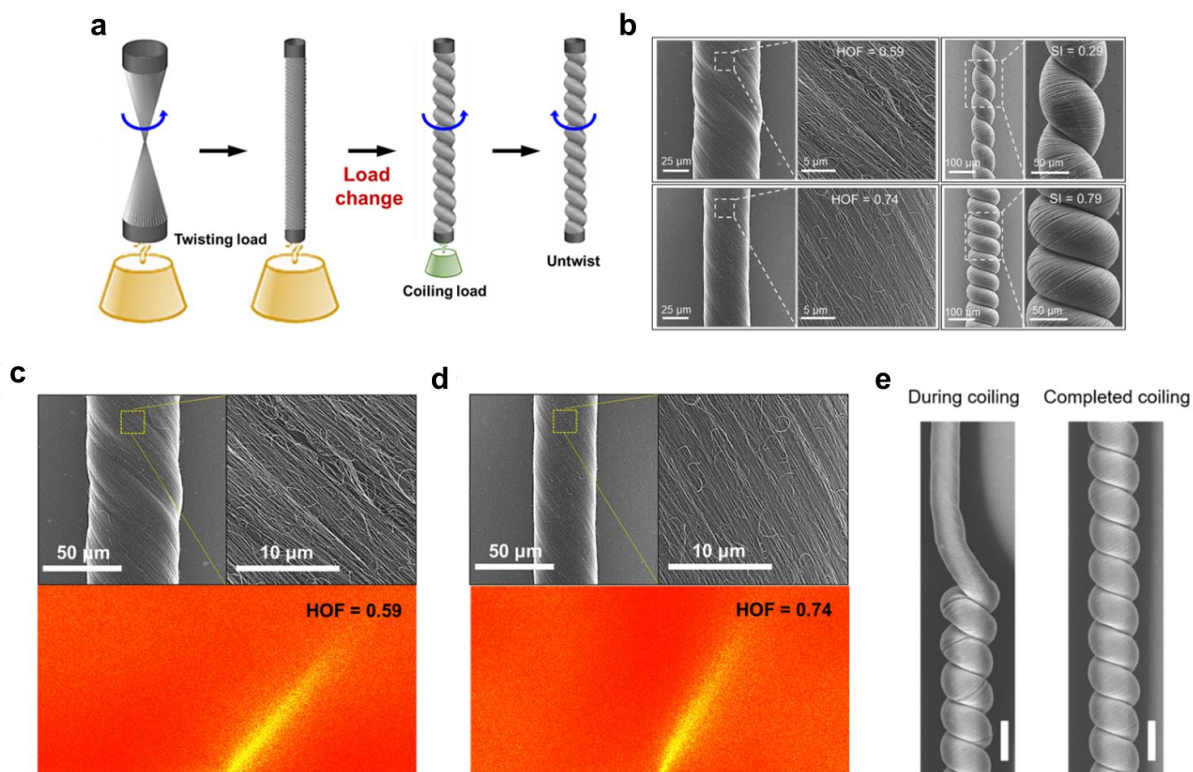
Figure S14. a. Illustration of the tension optimization process (TOP) for fabricating twisted, coiled CNT yarns from forest-drawn CNT sheets. **b.** SEM micrographs showing the structural differences between fully twisted CNT yarns that were twisted under a load of 3.3 MPa (top left) and 191.2 MPa (bottom left), a fully coiled yarn that was twisted under a 140.7 MPa load and coiled under a 95 MPa load (top right), and a fully coiled yarn that was twisted under a 140.7 MPa load and then coiled under a 3.2 MPa load (bottom right). The high load applied during the initial twisting part of TOP results in the pictured high degree of CNT alignment and the low load applied during the coiling part of TOP results in the pictured high spring index. **c-d.** SEM images and corresponding Fast Fourier Transform (FFT) images for a twisted yarn fabricated using a stress of 3.3 MPa (which has a CNT HOF of 0.59) (c), and a twisted yarn fabricated using a stress of 191.2 MPa (which has a CNT HOF of 0.74) (d). **e.** SEM images of a CNT yarn during coiling (left) and upon completion of coiling (right) (scale bar: 100 μm) during preparation of a TOP yarn. The load during twisting was 125 MPa and the load during coiling was 4 MPa. The spring index for the fully coiled yarn was 0.73.
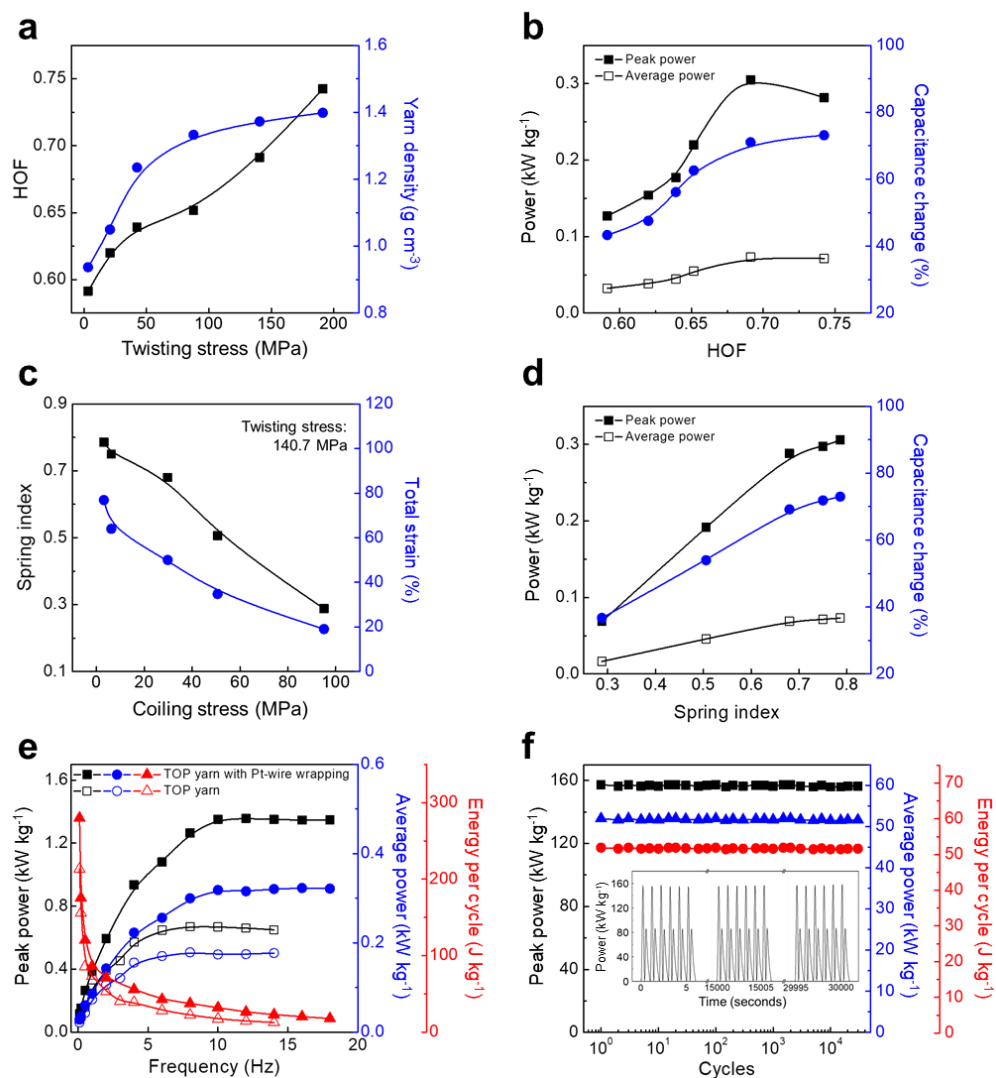
Figure S15. The tension optimization process (TOP) and the performance of TOP twistron harvesters in 0.1 M aqueous HCl. a. The yarn's Herman's orientation factor (HOF) and density as a function of the applied stress during twisting. **b.** For a 77% sinusoidal stretch at 1 Hz, the peak power (black solid squares), average power (black open squares), and maximum measured capacitance change (blue circles) of the coiled yarn as a function of the HOF for the fully twisted yarn. All coiled yarns of (b) were fabricated from the twisted yarns using a coiling stress of 3.2 MPa. **c.** The spring index and total strain as a function of the isobaric stress applied during coiling, when the stress during twist was 140.7 MPa. **d.** For the maximum strain of each spring index from (c) at 1 Hz, the peak power (black solid squares), average power (black open squares), and maximum measured capacitance change (blue circles) as a function of the spring index. **e.** The frequency dependencies of peak power (black squares), average power (blue circles) and energy per cycle (red triangles) for a 65% stretch, before (open symbols) and after (solid symbols) incorporating a Pt wire into a coiled TOP twistron that was fabricated using a 140.7 MPa stress during twist and a 3.2 MPa stress during coiling. **f.** The peak power, average power, and electrical energy per cycle during 30,000 stretch-and-release cycles to 60% total strain at 1 Hz for the above twistron yarn. (Inset) Output power versus time during typical cycles.

33
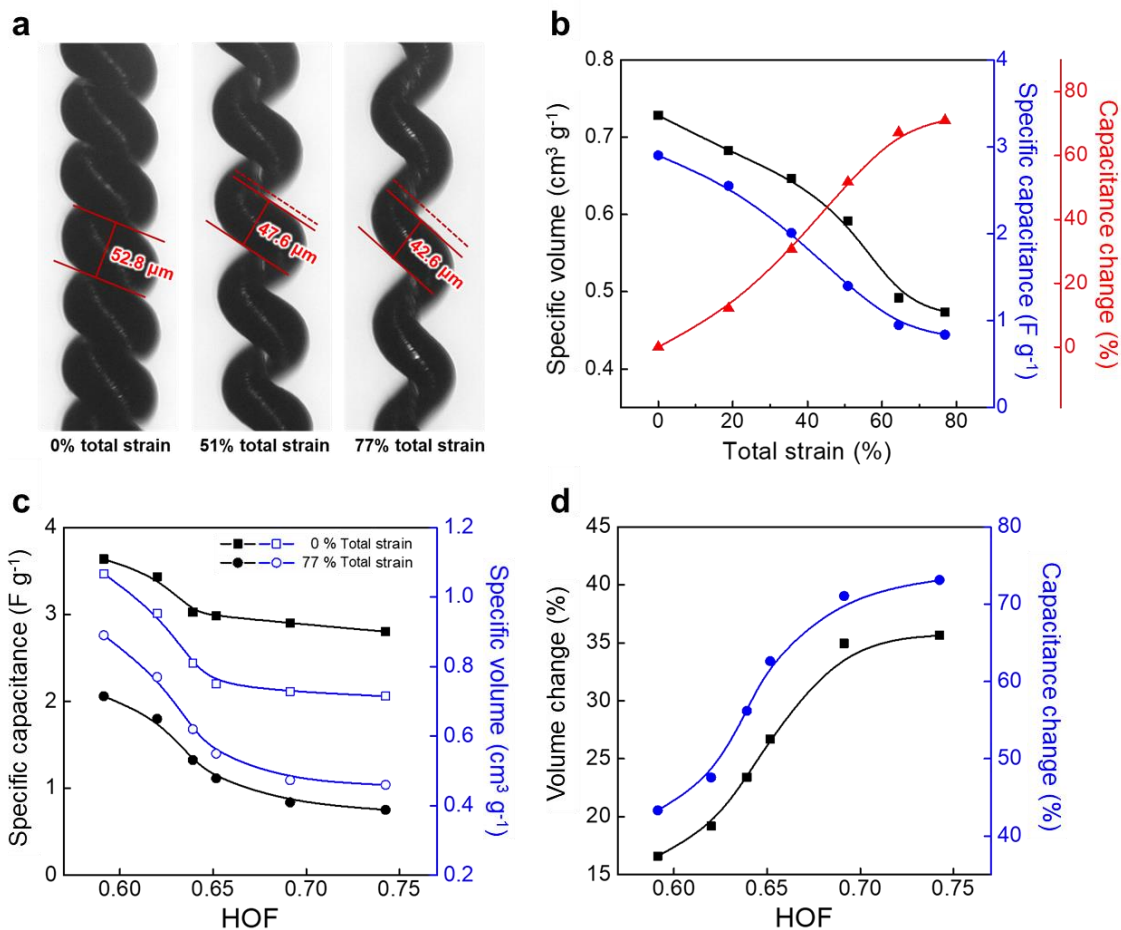
Figure S16. Relationships between total strain, volume change, and capacitance change for TOP CNT twistrons. a. Optical images of a twistron harvester that is stretched by 0, 51, and 77%. **b.** The strain dependence of yarn specific volume (calculated from optical images), specific capacitance, and capacitance change. (a) and (b) were obtained for a TOP CNT twistron that used applied stresses of 140.7 and 3.2 MPa during twist insertion and coiling. **c-d.** The specific capacitance and specific volume of a coiled yarn as a function of the HOF calculated from surface images of the fully-twisted yarn just before coiling (c), and the percent change in volume and capacitance for these yarns as a function of HOF (d). The progressively increasing HOFs in (c) and (d) were obtained for TOP CNT twistrons that used progressively increasing applied stresses of 3.3, 20.8, 42.5, 87.7, 140.7, and 191.2 MPa during twist insertion. The same 3.2 MPa stress was used during coiling for all twistrons.
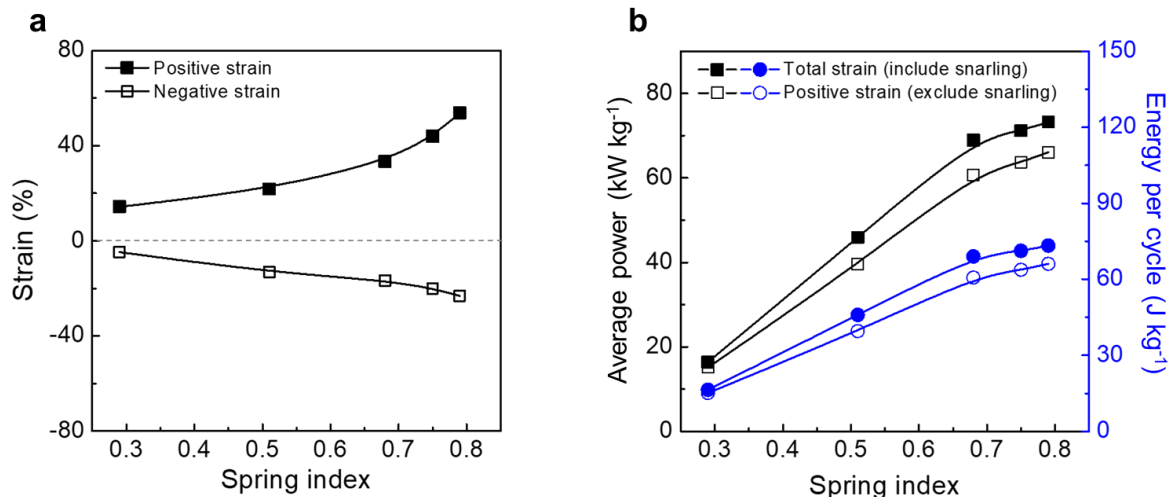
Figure S17. The effect of snarling for TOP CNT twistrons. a. The positive and negative strains (for non-snarled and snarled strain regions, respectively) for coiled yarns as a function of the spring index. **b.** The spring index dependencies of the average power and energy per cycle for a stretch that uses the total strain and only the snarling-free strain. The generated power and energy were obtained in 0.1 M HCl aqueous electrolyte for a 1 Hz stretch.
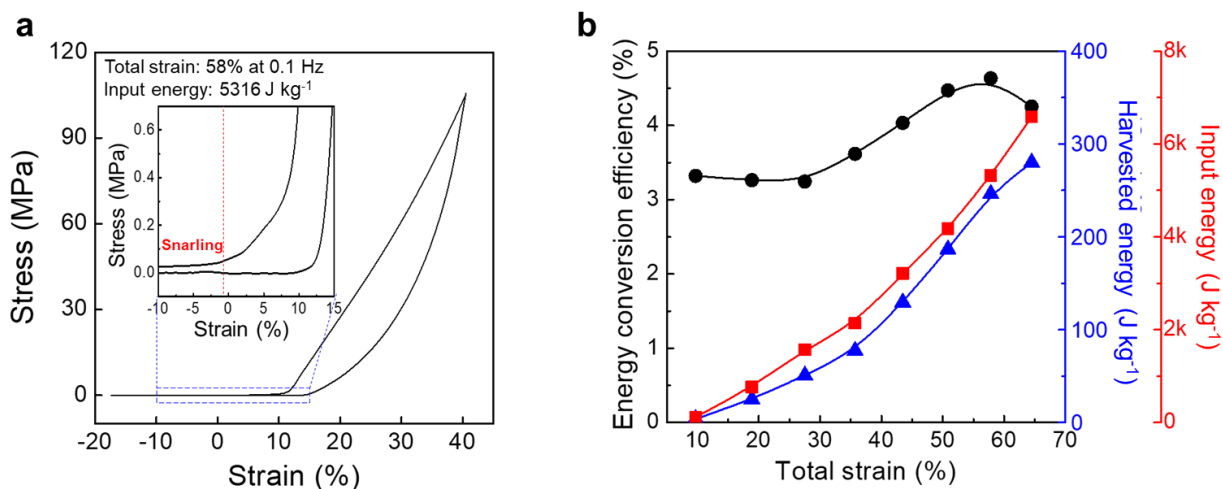

Figure S18. The tensile energy conversion efficiency of a TOP CNT twistron. a. Stress-strain curves (during stretch and stretch release), which is used for calculating the input mechanical energy for a TOP twistron yarn during a mechanical cycle to-and-from a total strain of 58%. The stretch-release cycle was at 0.1 Hz for a twistron whose performance was stabilized before the pictured 10th stress-strain cycle. (Inset: Expanded stress scale, so that the effect of snarling can be better seen.) **b.** The dependencies of energy conversion efficiency, harvested energy, and input energy on total strain for a Pt-wire-wrapped TOP yarn during cycling at 0.1 Hz. The TOP CNT twistron was fabricated by applying a 140.7 MPa stress during twist insertion and a 3.2 MPa stress during coiling.
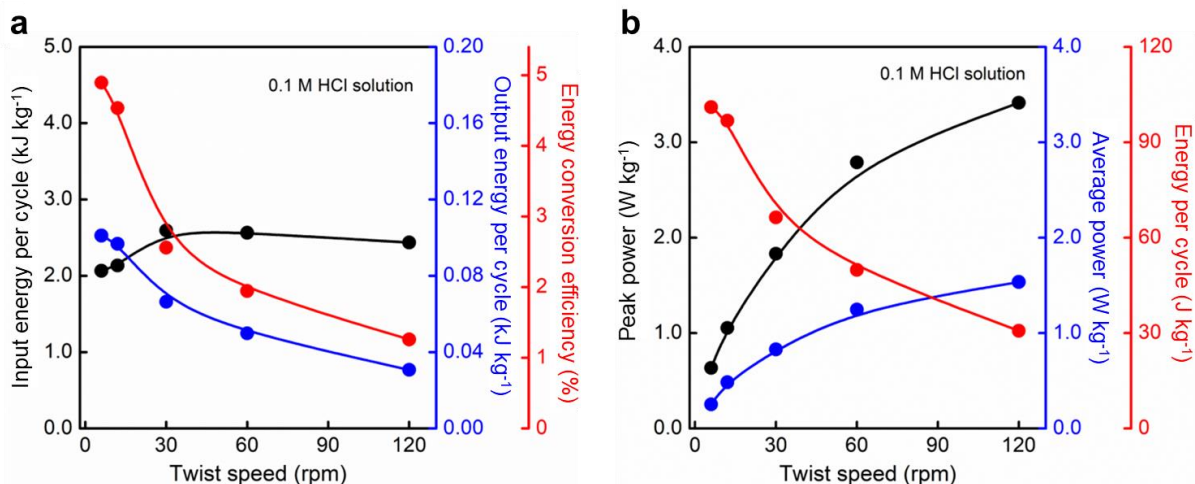
Figure S19. Energy harvesting in 0.1 M aqueous HCl electrolyte by inserting and removing twist from the coiled TOP yarn of Supplementary Fig. 14e without changing the number of coils. a. The twist speed dependencies of input mechanical energy per cycle, output electrical energy per cycle, and torsional energy conversion efficiency for a fully coiled TOP twistron during isometric twist insertion and removal. When normalized to the length of the coiled yarn (18.1 mm), the change in twist density (with respect to the initial fully coiled yarn) was a twist increase of 11 turns cm^{-1}. **b.** The twist speed dependencies of peak power, average power and energy per cycle for this fully coiled TOP twistron.
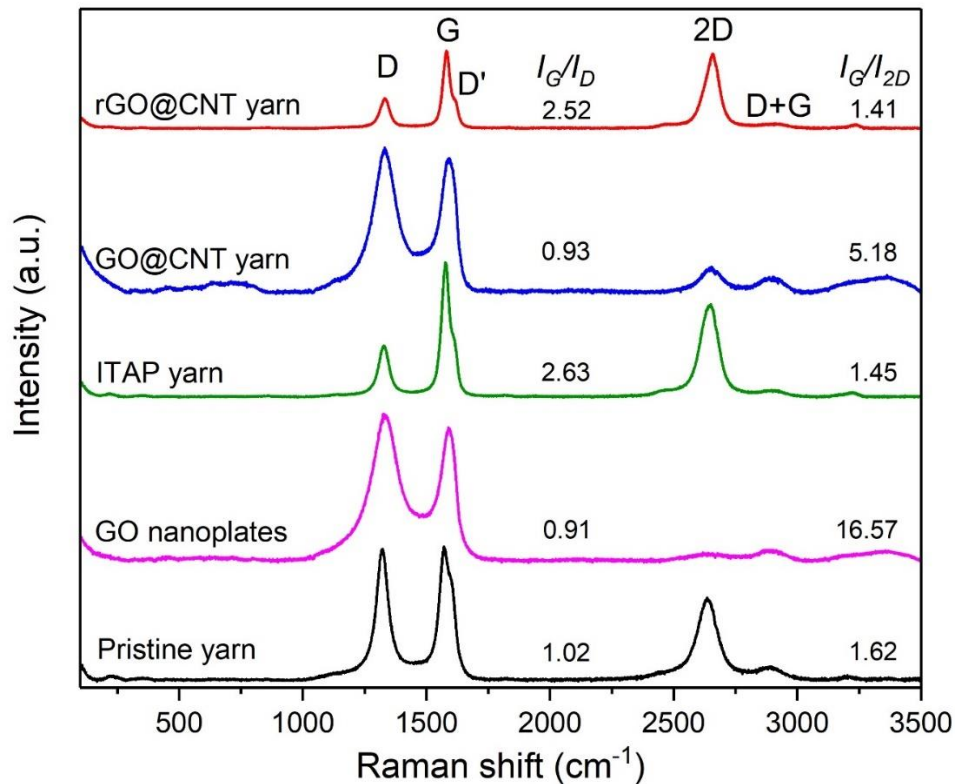
Figure S20. Comparison of the Raman spectra (for 632.8 nm excitation) of twisted pristine CNT yarn, 30 s ITAP-treated CNT yarn, GO nanoplates, GO@CNT yarn, and 30 s ITAP-treated rGO@CNT yarn.
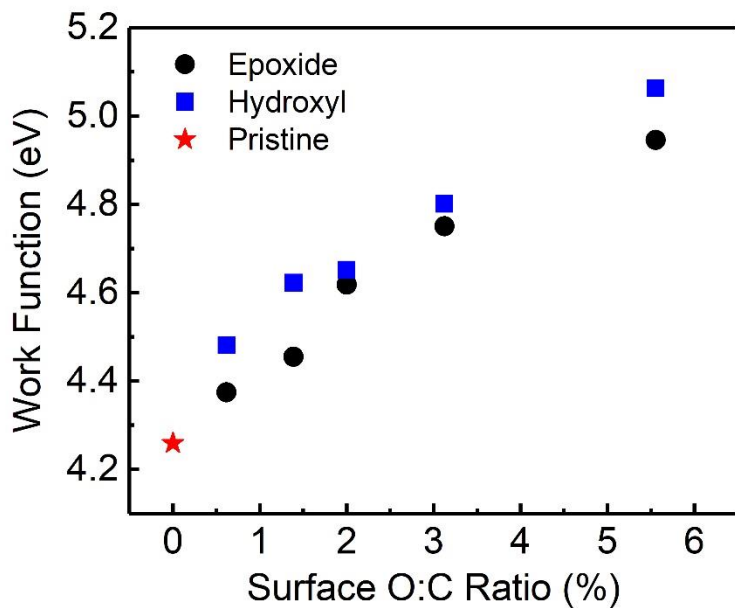

Figure S21. The calculated work function of the graphene bilayer for varying concentrations of epoxide and hydroxyl oxygen surface groups.
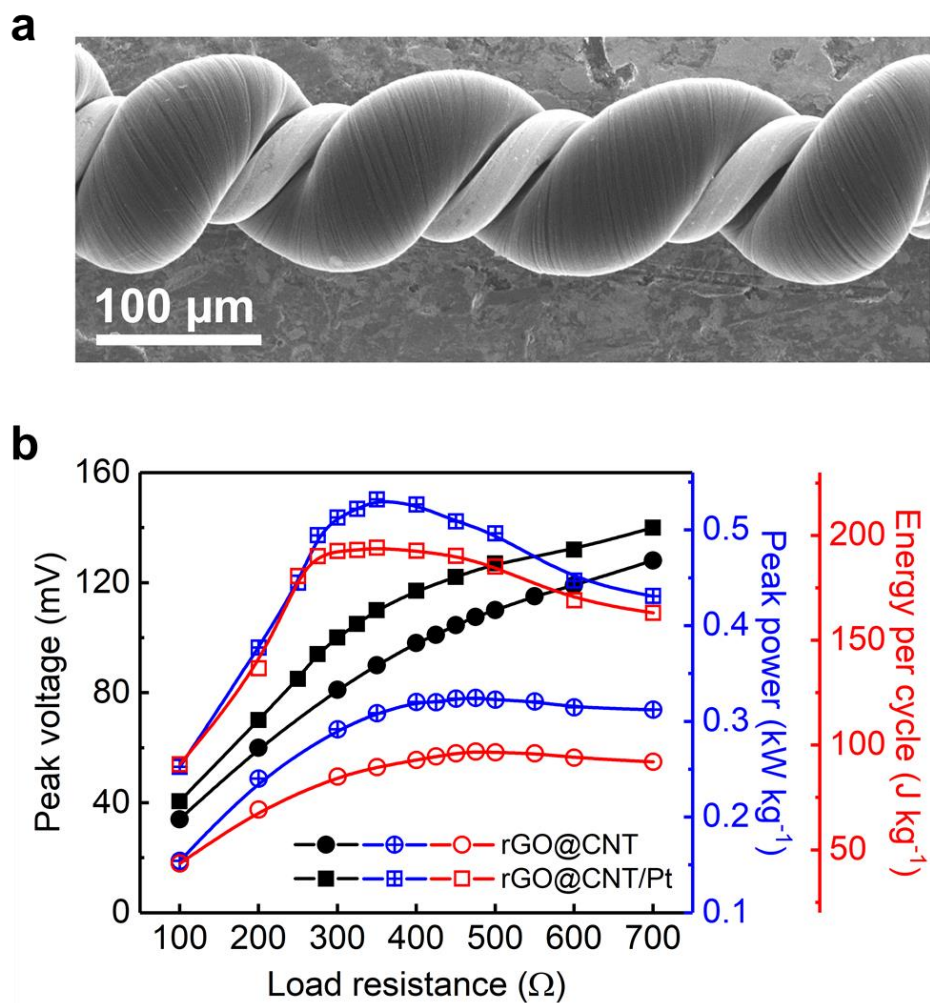
Figure S22. a. Scanning electron microscopy image of a Pt-wire wrapped rGO@CNT twistron. **b.** The load resistance dependencies of peak voltage, peak power, and energy per cycle for this stretch of a rGO@CNT twistron, before and after incorporating a Pt wire current collector.
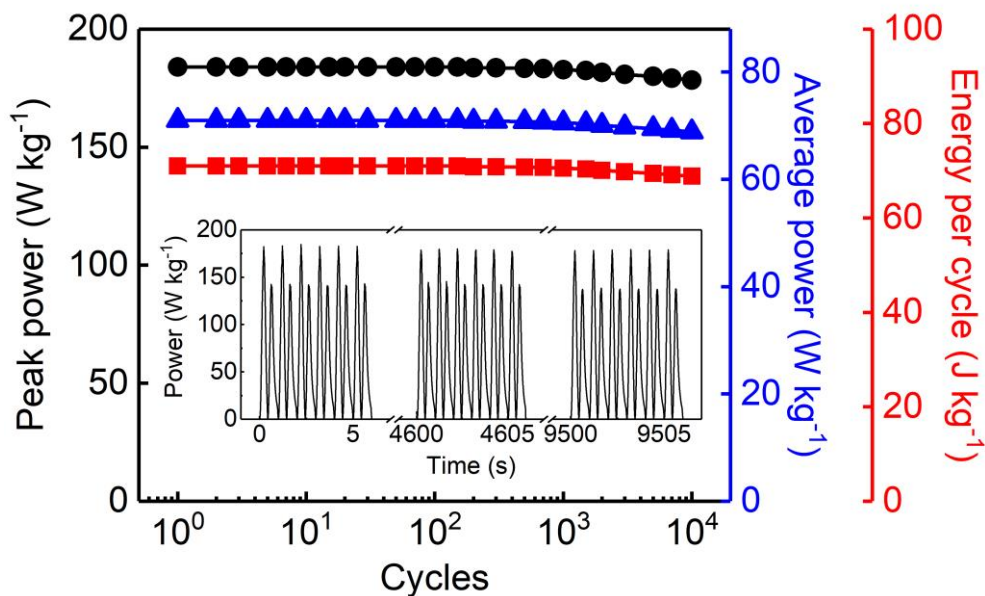
Figure S23. The peak power, average power and electrical energy per cycle during 10,000 stretch-and-release cycles to 27% strain at 1 Hz for a rGO@CNT twistron. (Inset) Output power versus time during different time intervals.
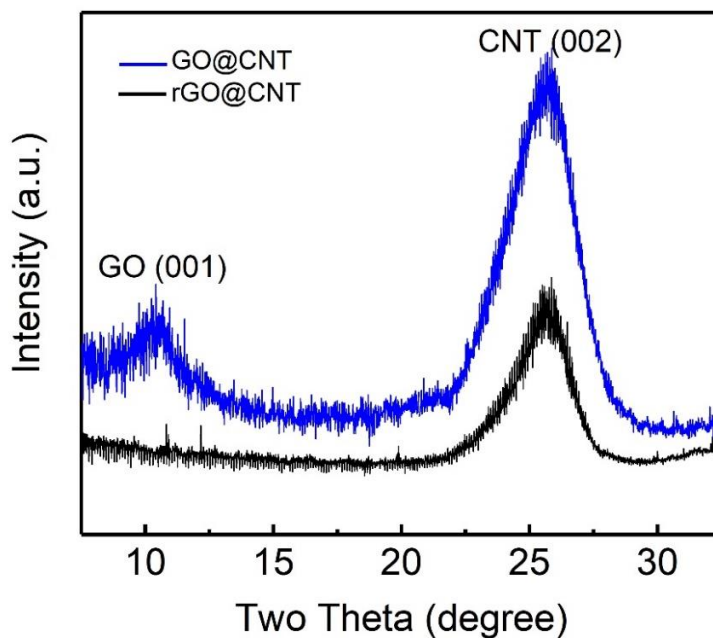

Figure S24. The equatorial direction diffraction intensity as a function of diffraction 2θ angle for GO@CNT yarn and rGO@CNT yarn.
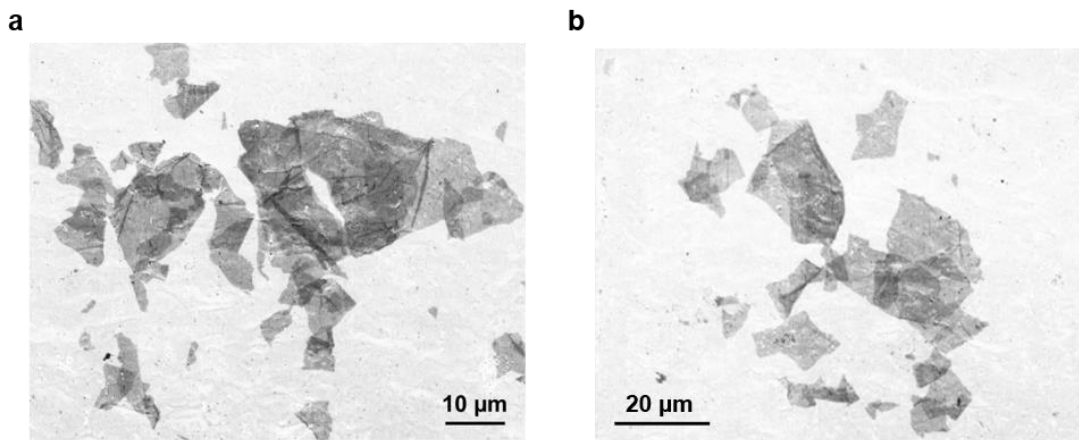
Figure S25. a-b. SEM micrographs of the graphene oxide (GO) nanoplates used for biscrolling. These nanoplates have a lateral size range of 10-25 µm.
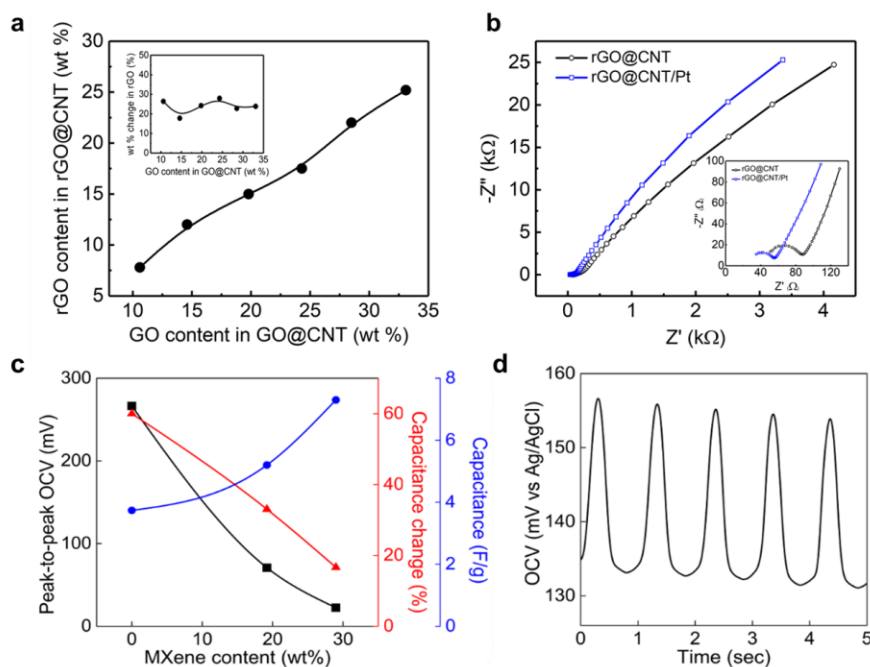

Figure S26. a. GO and rGO content in biscrolled yarns before and after ITAP reduction. The rGO contents in rGO@CNT were calculated assuming that ITAP resulted in the same weight percent change in CNT weight as for the pristine yarn. The inset shows the thereby calculated wt % change in rGO during ITAP as a function of the GO content in GO@CNT yarns. **b.** Electrochemical impedance spectroscopy results for coiled rGO@CNT twistron yarns before and after plying a 25-µm diameter Pt wire current collector. The inset shows a magnified view of the high-frequency region. These yarns were used for the harvester measurements of Fig. 3d. **c.** The dependence of peak-to-peak OCV, capacitance change, and specific capacitance on MXene content in a MXene@CNT yarn. **d.** The time dependence of OCV change for a 30 wt% MXene@CNT yarn during a 1 Hz, 45% sinusoidal deformation.
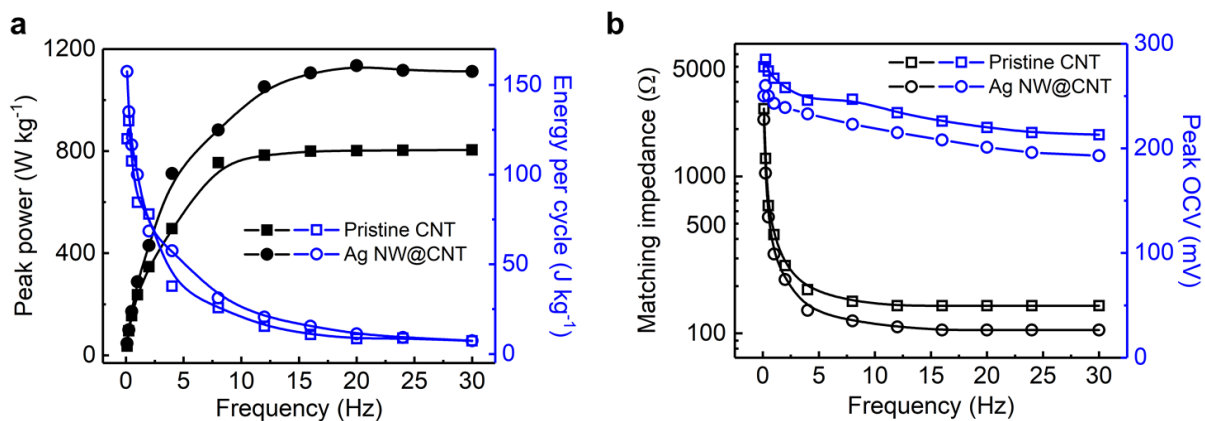
Figure S27. Electrochemical measurements in 0.1 M aqueous HCl before and after biscrolling about 15 wt % of silver nanowires into a CNT yarn. a. The frequency dependencies of peak power and energy per cycle before and after biscrolling the silver nanowires. **b.** The frequency dependencies of matching impedance and peak OCV before and after biscrolling the silver nanowires.
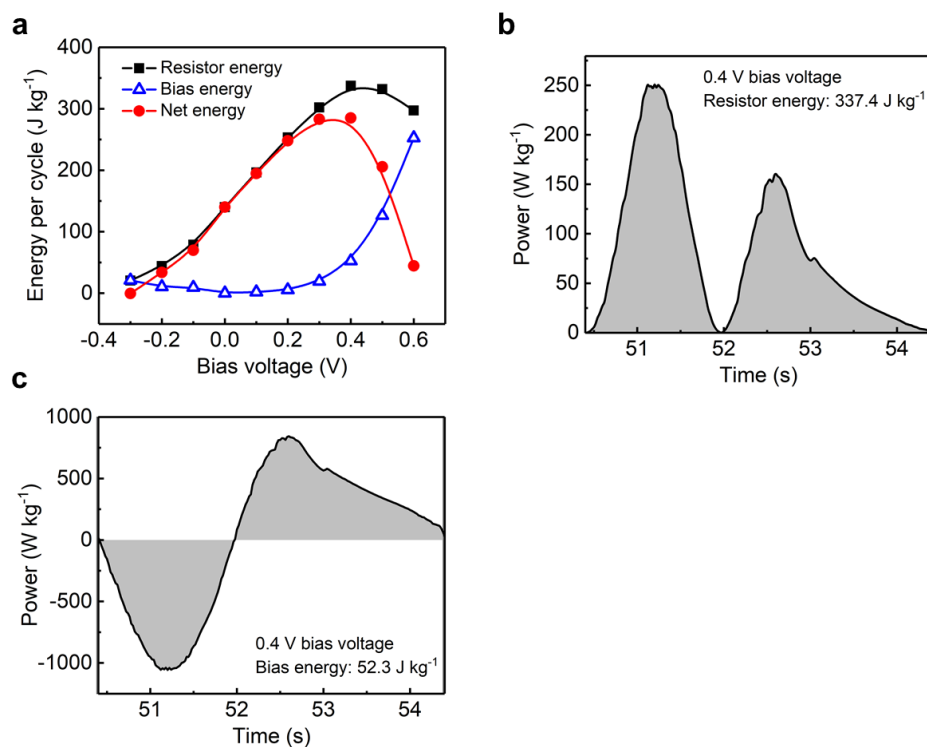

Figure S28. The effect of an externally applied bias voltage on tensile energy harvesting for a rGO@CNT twistron harvester that is undergoing a 46% stretch at 0.25 Hz in 0.1 M HCl. a. The energy delivered to an external resistive load (black squares), the energy consumed in providing the external bias voltage (blue hollow triangles), and the net energy harvested (red circles) as a function of the externally applied bias voltage. **b-c.** The energy delivered to an external resistive load (b) and the energy consumed in providing the external bias voltage (c) for an applied bias voltage of 0.4 V.

41
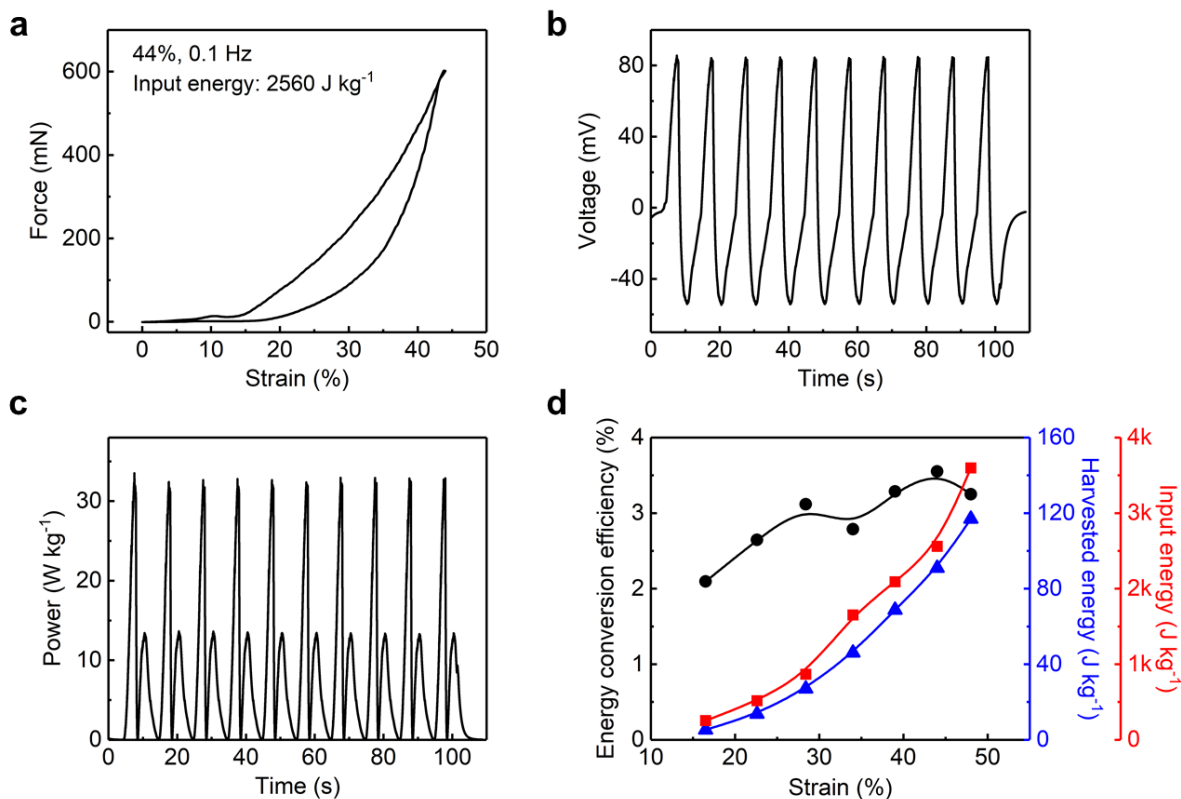
Figure S29. The energy conversion efficiency of a coiled ITAP rGO@CNT yarn harvester in 0.1 M aqueous HCl. a. The force-strain curve of an 8.6-mm-long coiled yarn when linearly stretched to 44% strain at 0.1 Hz. The mechanical energy lost between stretch and release during one cycle was 2560 Joules per kg of yarn. **b.** The voltage generated on a 1400-ohm load during the stretching cycle in (a). **c.** The instantaneous generated power during the cyclic stretching in (a). The electrical energy generated per cycle was 91 J kg^{-1}, corresponding to an energy conversion efficiency of 3.55%. **d.** The dependencies of energy conversion efficiency, harvested energy, and input mechanical energy on the applied strain during a 0.1 Hz stretch.
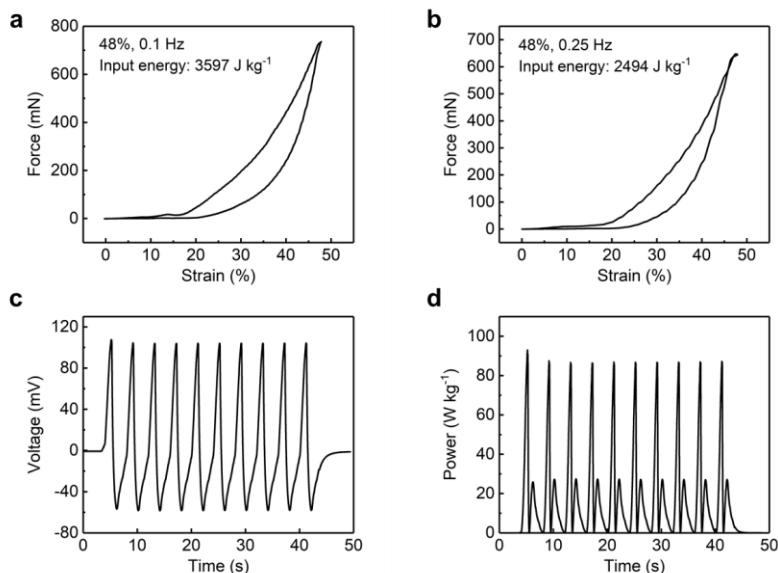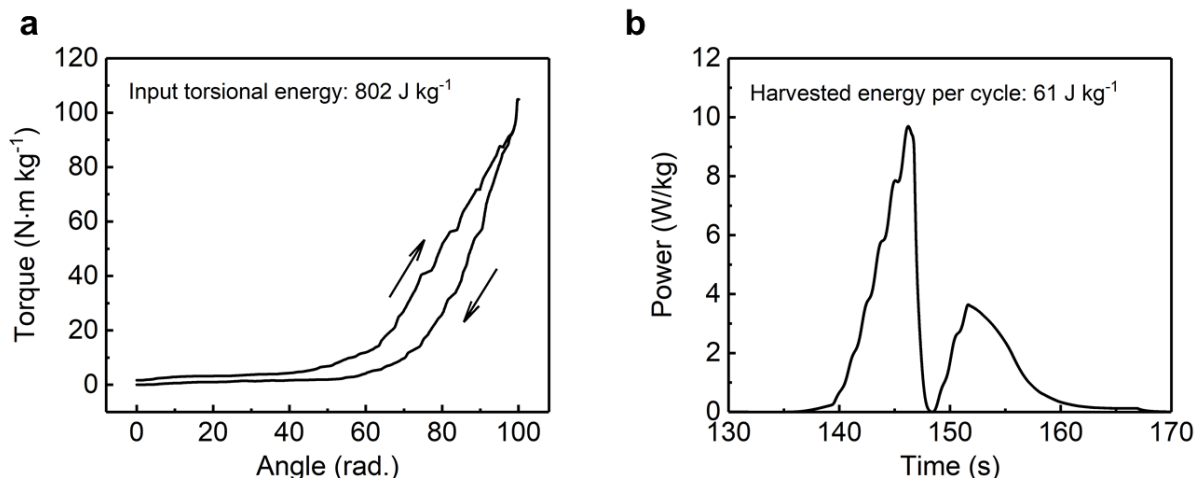
Figure S30. Optimizing the energy conversion efficiency of a coiled ITAP rGO@CNT yarn harvester in 0.1 M aqueous HCl electrolyte. a. The force-strain curve of an 8.6-mm-long coiled yarn when linearly stretched to 48% strain at 0.1 Hz in the electrolyte. The mechanical energy lost between stretch and release during one cycle was 3597 Joules per kg of yarn. **b.** When the same yarn was stretched to 48% strain at 0.25 Hz, the mechanical energy lost during a cycle decreased to 2494 Joules per kg of yarn. **c.** The voltage generated on an 800-ohm load during the cyclic stretching of (b). **d.** The time dependence of generated power during the cyclic stretching of (b). The electrical energy generated per cycle was 97 J kg^{-1}, corresponding to an energy conversion efficiency of 3.89%. Further increase of the stretching frequency increased the hysteresis in the force-strain curve, and correspondingly resulted in an increased energy loss and a decreased efficiency.
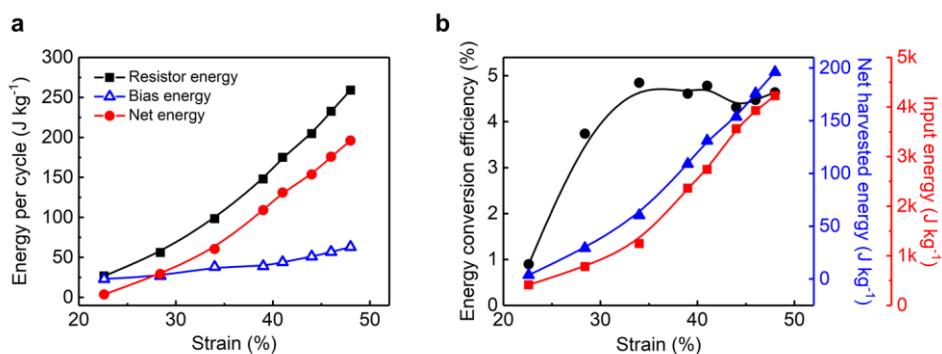

Figure S31. The energy conversion efficiency for a ITAP rGO@CNT harvester under a 0.4 V bias voltage in 0.1 M aqueous HCl electrolyte when using a 0.25 Hz stretch frequency. a. The energy delivered to an external resistive load (black squares), the energy consumed in providing the external bias voltage (blue hollow triangles), and the net energy harvested (red circles) as a function of the applied tensile strain. **b.** The dependencies of energy conversion efficiency, harvested energy and input mechanical energy on the applied tensile strain. A maximum energy conversion efficiency of 4.85% was obtained for a 34% strain, and then the efficiency reached a plateau with further increase of the applied strain.

43
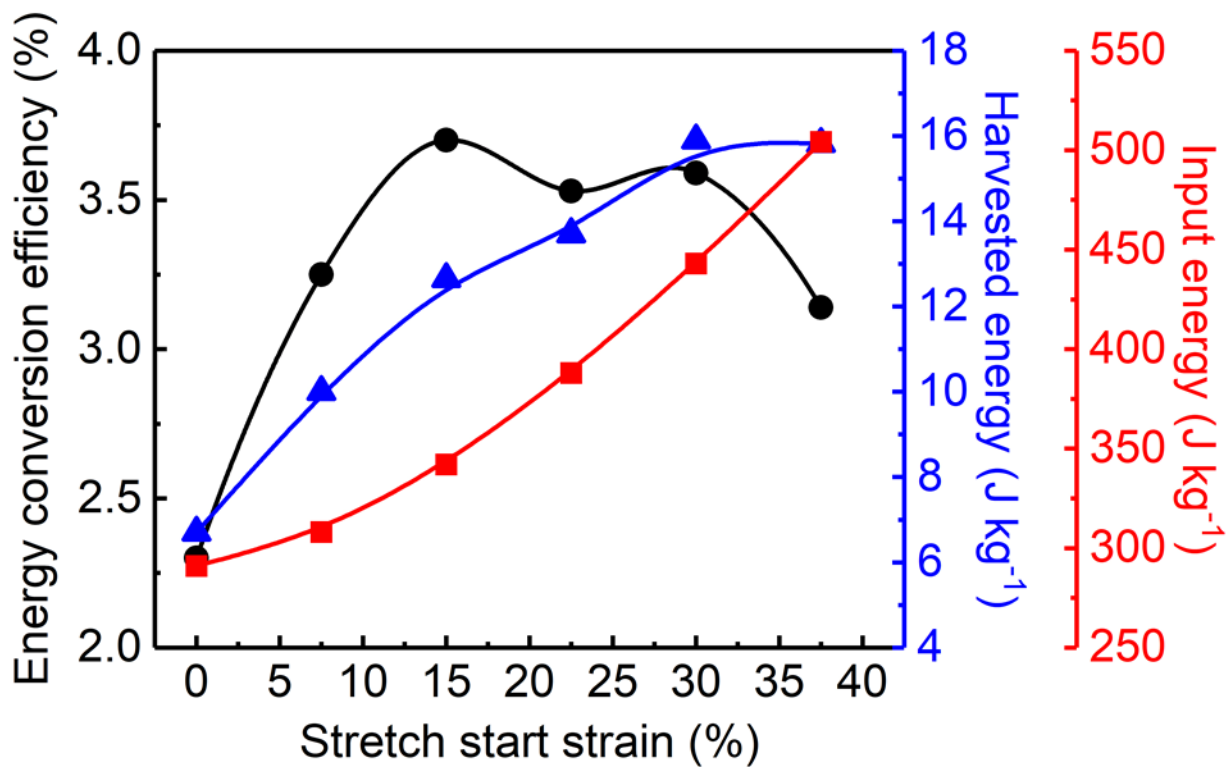
Figure S32. The effect of tuning the initial strain on the energy conversion efficiency, harvested energy, and input mechanical energy for a fixed percent stretch (7.5%) during harvesting at 0.25 Hz for a rGO@CNT twistron.

Figure S33. The energy conversion efficiency for a ITAP rGO@CNT twisted, non-coiled torsional harvester yarn in 0.1 M aqueous HCl electrolyte when using a 24 rpm rotation speed. a. Torque versus rotation angle curve for an ~5-cm-long twisted, non-coiled yarn under isometric twist insertion and removal. The mechanical energy lost between twist insertion and removal during one cycle was 802 Joules per kg of yarn. **b.** The instantaneous generated power during the cyclic twist insertion and removal in (a). The electrical energy generated per cycle was 61 J kg^{-1}, corresponding to an energy conversion efficiency of 7.6%.
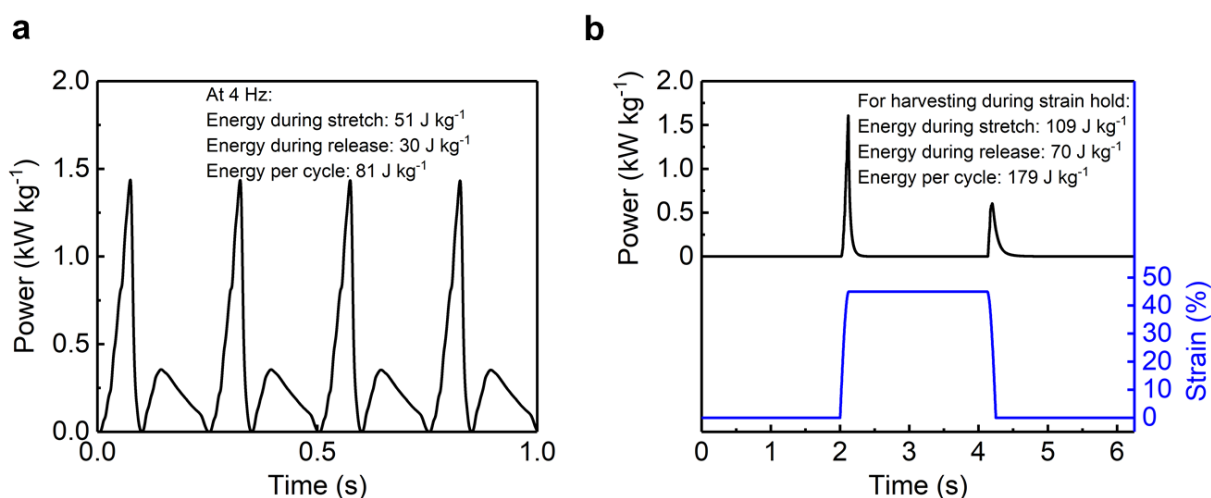
Figure S34. Comparison of energy generation by continuous sinusoidal stretch and release of a twistron at 4 Hz and that obtained by additionally allowing energy harvesting for an extra 2 s between the end of stretch and the beginning of release and between the end of release and the beginning of stretch in 0.1 M aqueous HCl. a. The time dependence of power output during 4 Hz continuous sinusoidal deformation of a rGO@CNT twistron. **b.** The time dependence of total harvested energy when an extra 2 s of harvesting time is inserted after both stretch and release processes.

45
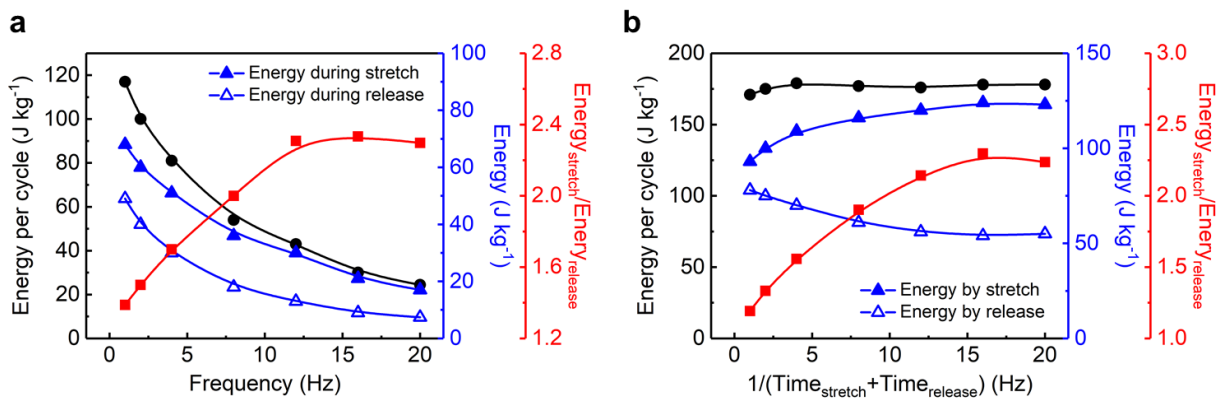
Figure S35. a. The frequency dependencies of energy per cycle, energy during stretch, energy during release, and their ratio for continuous sinusoidal deformation of a twistron. **b.** The frequency dependencies of energy per cycle, energy by stretch, energy by release, and their ratio for the process of Supplementary Fig. 34b, in which an extra 2 s of harvesting time is inserted after stretch and stretch release.
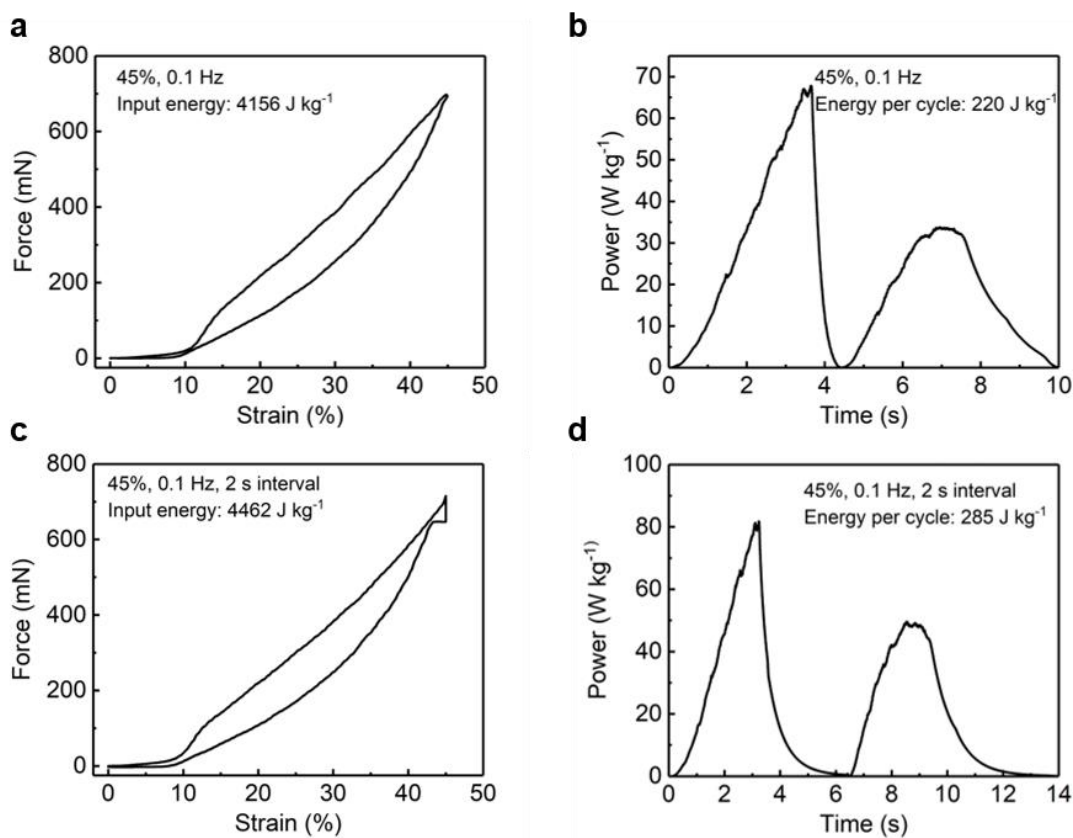
Figure S36. Stress-strain (a, c) and power generation curves (b, d) for a Pt-wire-wrapped rGO@CNT twistron, which enable calculation of the effect of 2 s time delays between stretch and stretch-release on the energy conversion efficiency for 45%, 0.1 Hz sinusoidal wave harvesting.
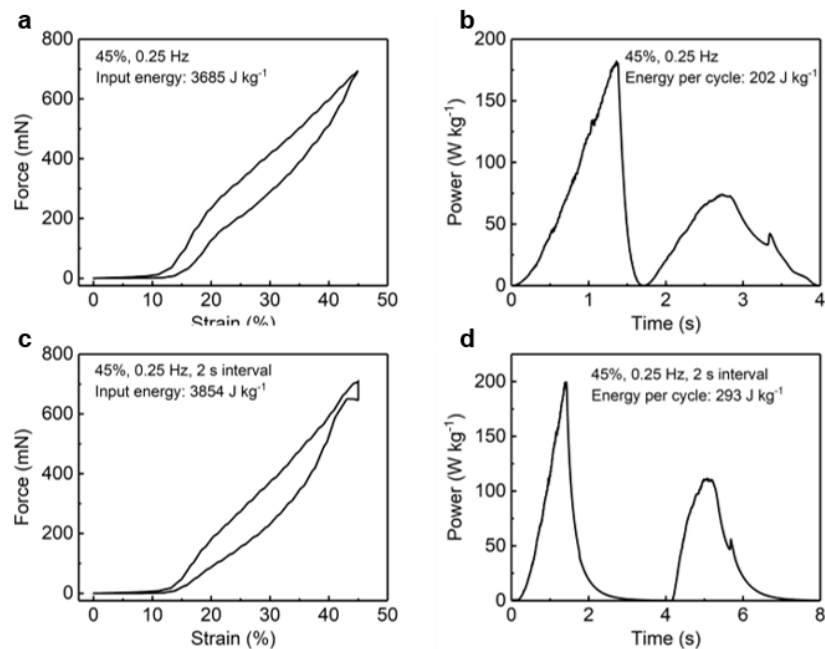
Figure S37. Stress-strain (a, c) and power generation curves (b, d) for a Pt-wire-wrapped rGO@CNT twistron, which enable calculation of the effect of 2 s time delays between stretch and stretch-release on the energy conversion efficiency for 45%, 0.25 Hz sinusoidal wave harvesting.
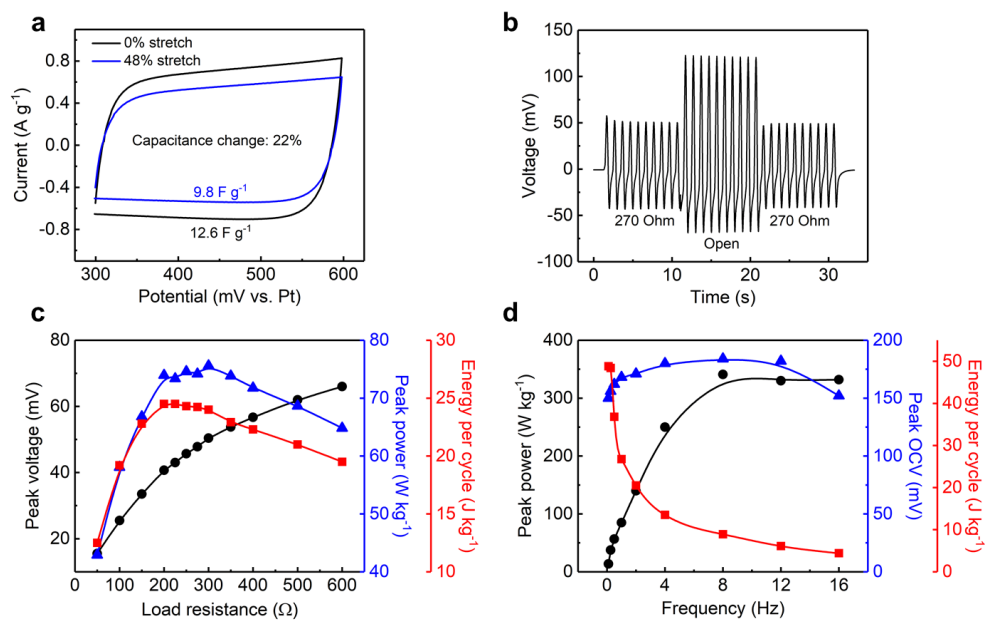
Figure S38. The performance of a rGO@CNT twistron harvester in an organic electrolyte (0.1 M LiBF₄ in acetonitrile). a. CV curves (at 50 mV s^{-1} scan rate) providing the capacitance and capacitance change for 48% stretch. **b.** The open-circuit voltage and the voltage across a 270 ohm load resistor for 48% stretch at 1 Hz. **c.** The load resistance dependencies of peak voltage, peak power, and energy per cycle for a 1 Hz, 48% stretch. **d.** The frequency dependencies of peak power, peak OCV, and energy per cycle for a 48% stretch.

47
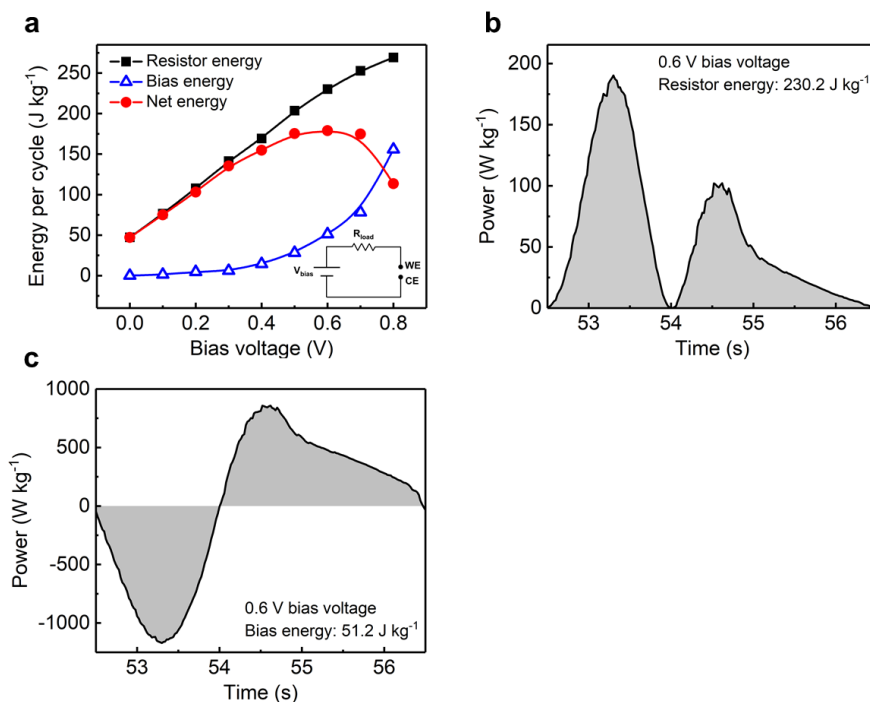
Figure S39. The effect of an externally applied bias voltage on tensile energy harvesting by a rGO@CNT twistron harvester when using a 48% sinusoidal stretch at 0.25 Hz and an electrolyte comprising 0.1 M LiBF₄ in acetonitrile. a. The energy delivered to an external resistive load (black squares), the energy consumed in providing the external bias voltage (blue hollow triangles), and the net energy harvested (red circles) as a function of the externally applied bias voltage. **b-c.** Plots showing (shaded areas) the energy delivered to an external resistive load (b), and the energy consumed in providing the external bias voltage (c), for an applied bias voltage of 0.6 V.
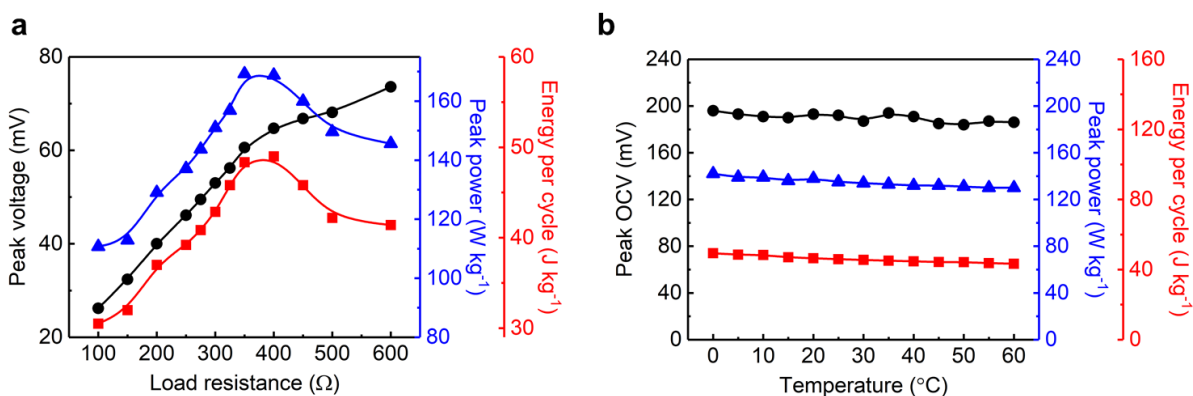
Figure S40. The performance of an ITAP rGO@CNT twistron harvester in 0.6 M NaCl aqueous electrolyte. a. The load resistance dependencies of peak voltage, peak power, and energy per cycle for a coiled rGO@CNT twistron yarn during a 1 Hz, 48% sinusoidal stretch. **b.** The effects of temperature on peak OCV (black circles), peak power (blue triangles), and harvested energy per cycle (red squares) for a coiled rGO@CNT twistron yarn during a 1 Hz, 48% sinusoidal stretch.

48
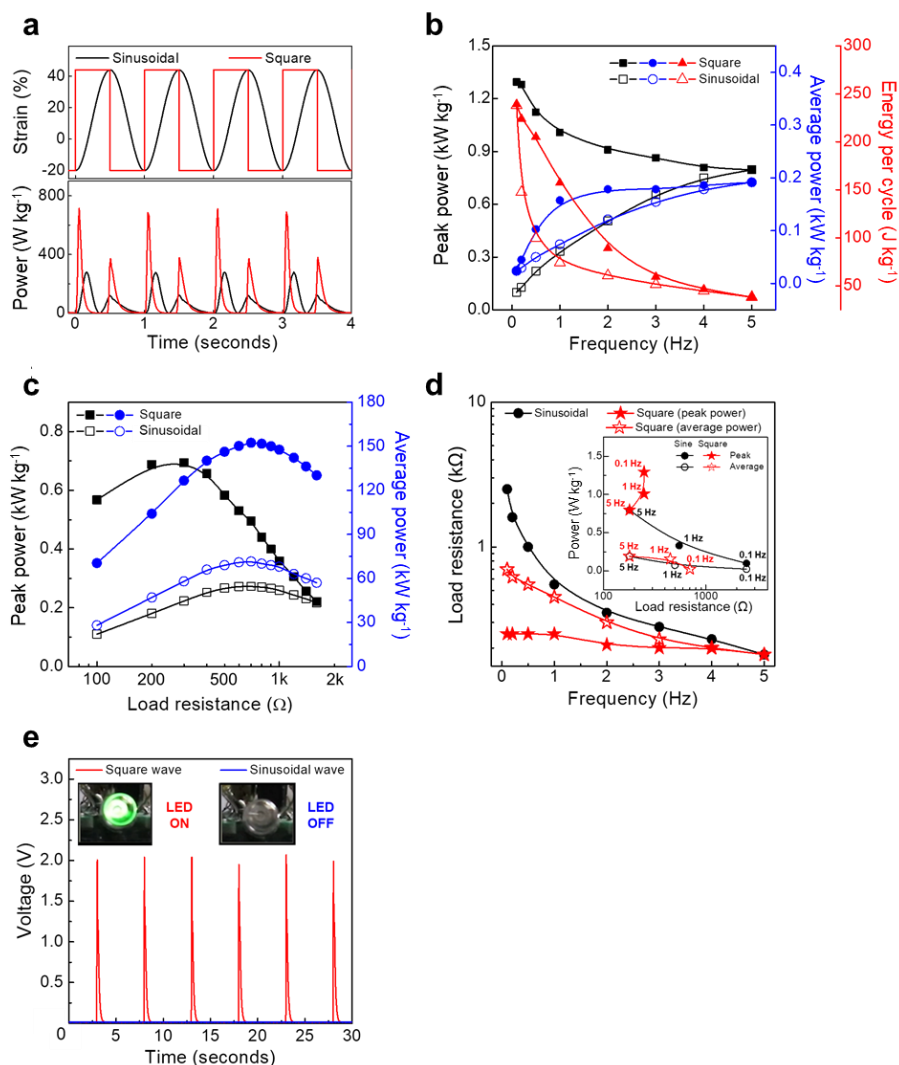
Figure S41. Performance comparison for square-wave and sinusoidal-wave energy harvesting by coiled TOP twistrons in 0.1 M aqueous HCl. a. The time dependence of the applied strain (top) and the produced output power (bottom) for 1 Hz square-wave and sinusoidal applied strains. **b.** The peak power, average power, and energy per cycle for a 65% stretch as a function of the frequency of the applied sinusoidal and square-wave strains for a Pt-wire-wrapped TOP coiled yarn. **c.** Peak power and average power versus load resistance for a 1 Hz, 65% total strain by sinusoidal and square-wave deformations for a TOP harvester. **d.** The frequency dependencies of peak-power-optimizing and average-power-optimizing load resistances for sinusoidal and square-wave applied strains for a Pt-wire-wrapped TOP harvester. (Inset) The load resistance that provides maximum peak power and average power for square-wave and sinusoidal deformation at different frequencies. **e.** The time dependence of the output voltage of a twistron-powered boost-converter circuit that was used for lighting an LED, when powered by stretching a TOP twistron yarn by 20%, using a square-wave (red) and sinusoidal (blue) strain. The insets show that the LED emits light only when powered by the square-wave. An LTC-3108 was used for the boost-converter.

49
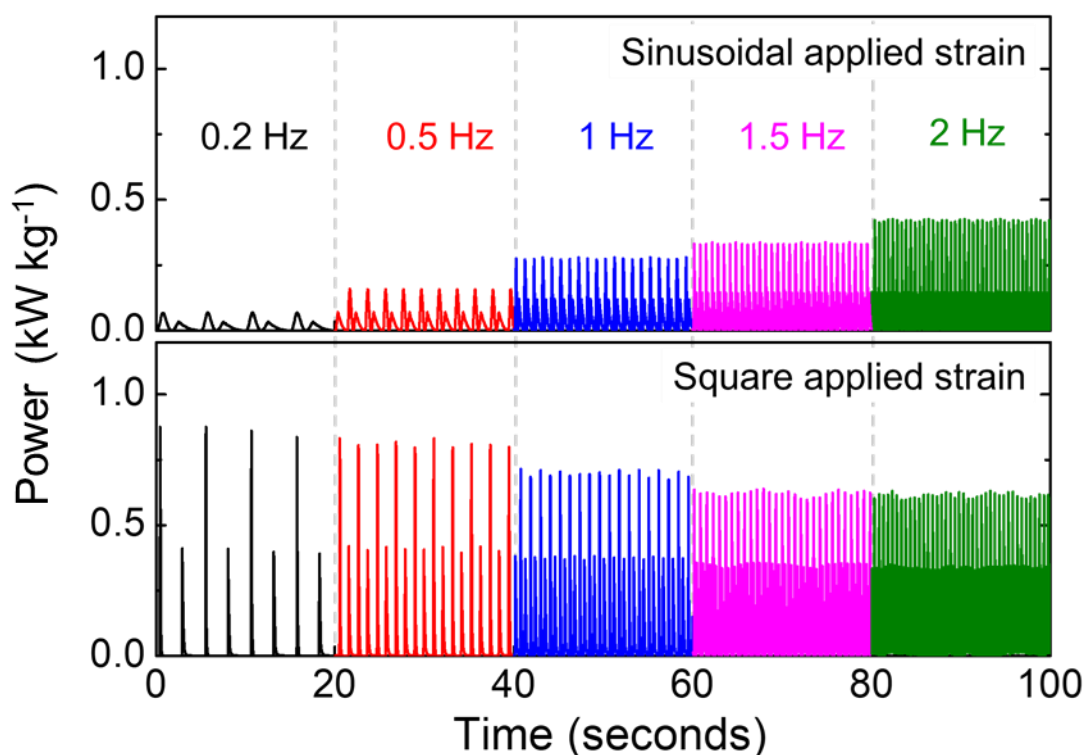
Figure S42. The output power of a TOP twistron (for load impedances that maximizes peak power) for sinusoidal and square-wave tensile strains of 64%, and for stretch frequencies from 0.2 to 2 Hz.
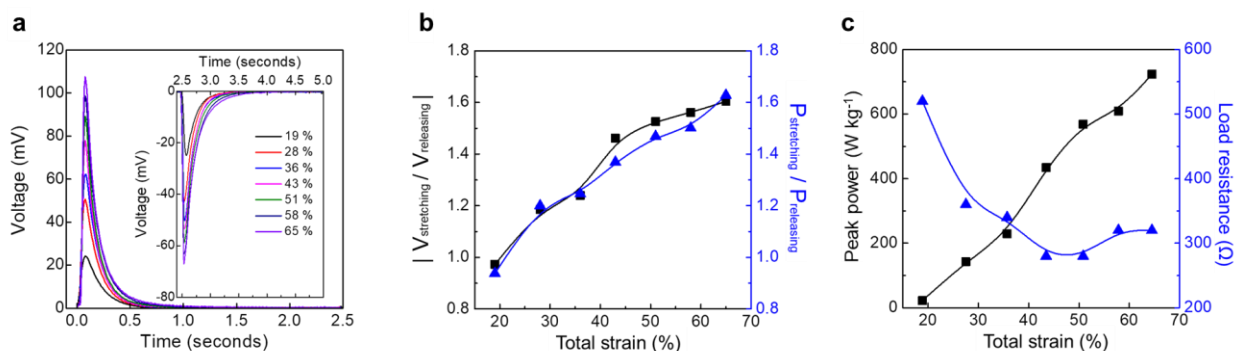
Figure S43. TOP harvester output for 0.2 Hz square-wave strains in 0.1 M HCl aqueous electrolyte. a. The time dependence of output voltage during stretch (main figure) and stretch release (inset) for a load resistance that maximizes the peak power for square-wave strains between 19% and 65%. **b.** The ratio of the peak voltage on stretching to the peak voltage on stretch-release and the ratio of the average power output on stretching to the average power output on stretch-release as a function of strain for the data in (a). **c.** The peak power and peak power optimizing load resistance for a square-wave stretch.
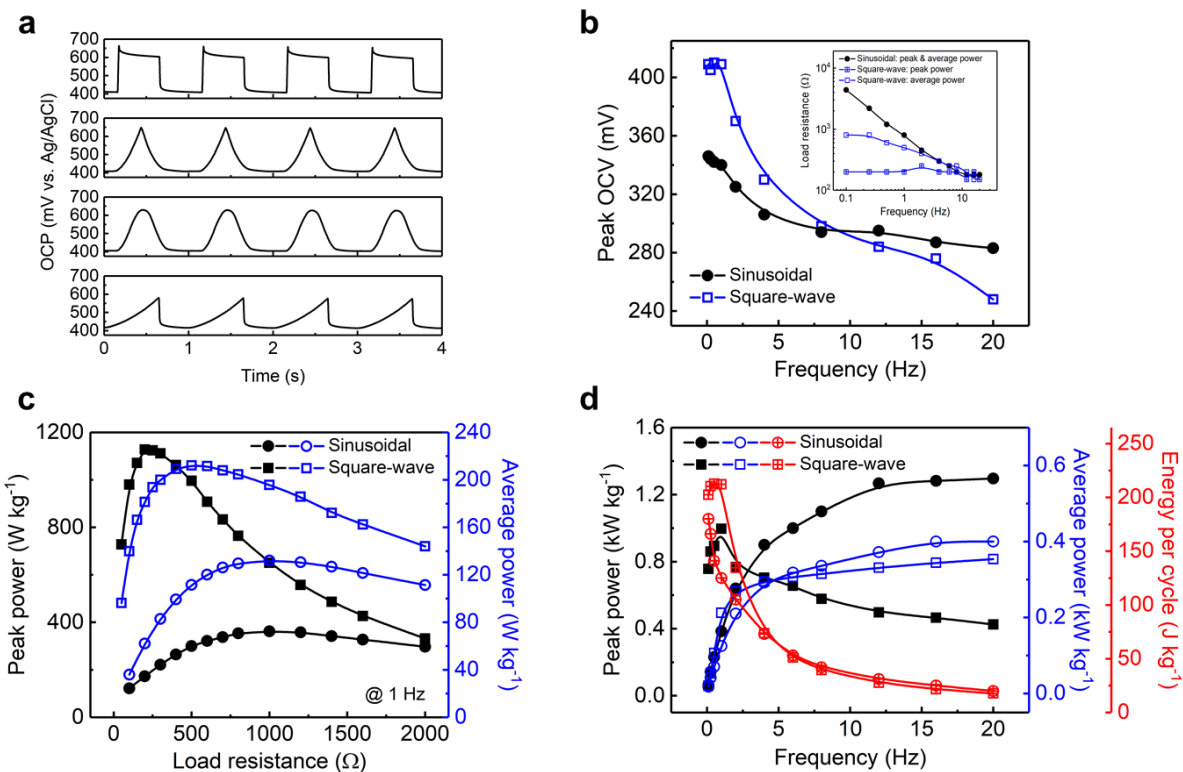
Figure S44. Performance comparison for sinusoidal and square-wave energy harvesting by rGO@CNT twistrons in 0.1 M aqueous HCl. a. The time dependence of the open circuit potential for square-wave, triangle, sinusoidal, and sawtooth applied strains to 38% at 1 Hz. **b.** The dependence of peak OCV on frequency for square-wave and sinusoidal deformations (inset: the dependence of performance optimizing load resistances, which optimizes either peak or average power, on frequency for square-wave and sinusoidal deformations). **c.** Peak power and average power versus load resistance for a 1 Hz, 48% strain by sinusoidal and square-waves. **d.** Peak power, average power, and energy per cycle for a 48% stretch as a function of the frequency of the applied sinusoidal and square-wave strains for the load resistance that maximizes these quantities.

51
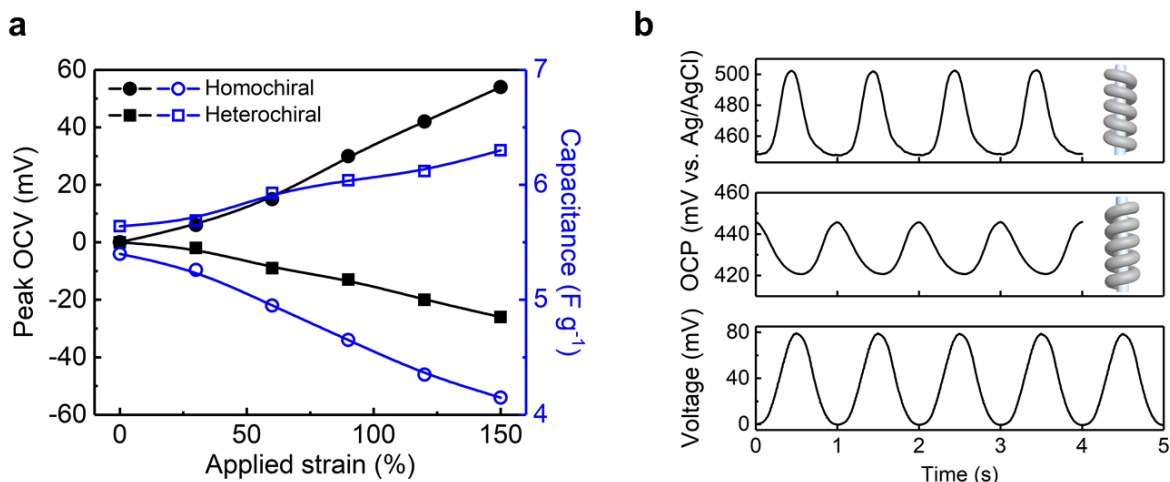
Figure S45. a. Peak OCV and capacitance versus applied strain for the homochiral and heterochiral harvesters. **b.** OCP versus time during 150% stretch in 0.1 M aqueous HCl for homochiral (top) and heterochiral (middle) yarns, produced by mandrel coiling on a 200% elongated, 1-mm-diameter rubber core, showing opposite stretch-induced voltages. The bottom plot shows the voltage output obtained by using the above homochiral and heterochiral yarns as both electrodes.
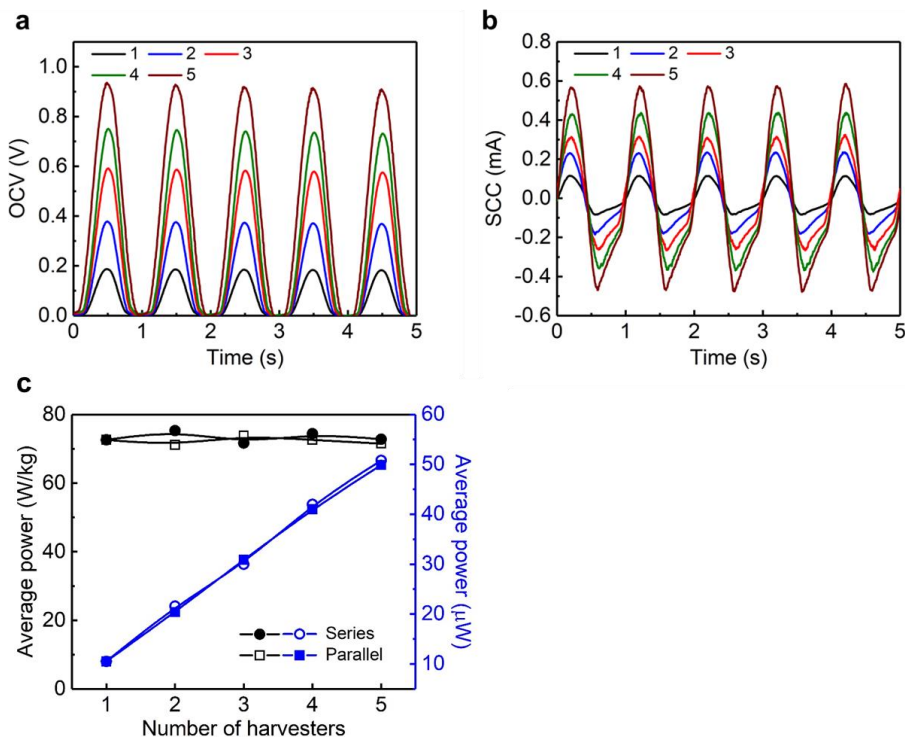
Figure S46. OCV and SCC for series (a) and parallel (b) connected solid-state harvesters of Fig. 4f, where the number labels correspond to the number of identical twistrons that are connected either in series or in parallel. **c.** The gravimetric and net average power output for a 1 Hz, 40% sinusoidal strain when ITAP-treated CNT yarn harvesters are connected in series or in parallel.
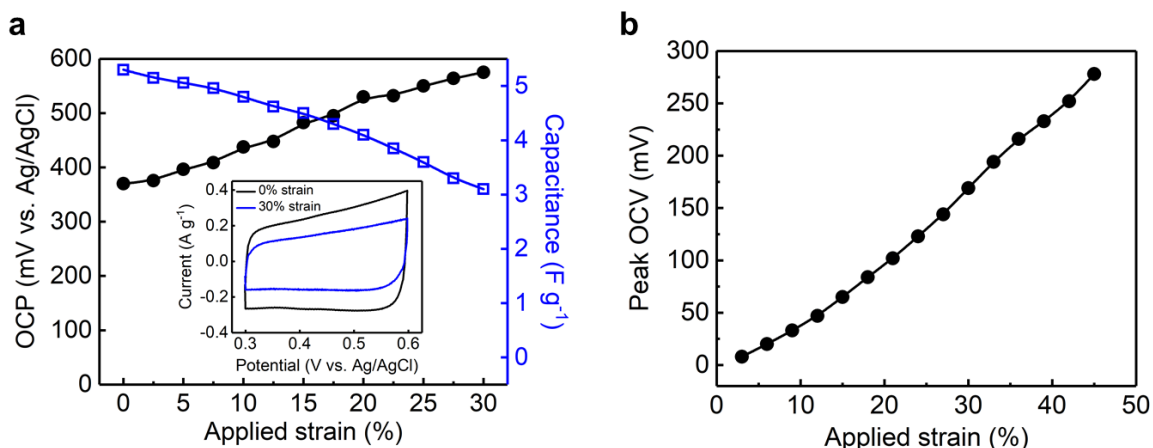
Figure S47. a. Capacitance and OCP versus applied strain for the rGO@CNT harvester of Fig. 3d. (Inset) Cyclic voltammetry curves for 0 and 30% strain. **b.** The dependence of OCV on the applied strain for the dual-electrode solid-state harvester of Fig. 4f and Supplementary Fig. 48.
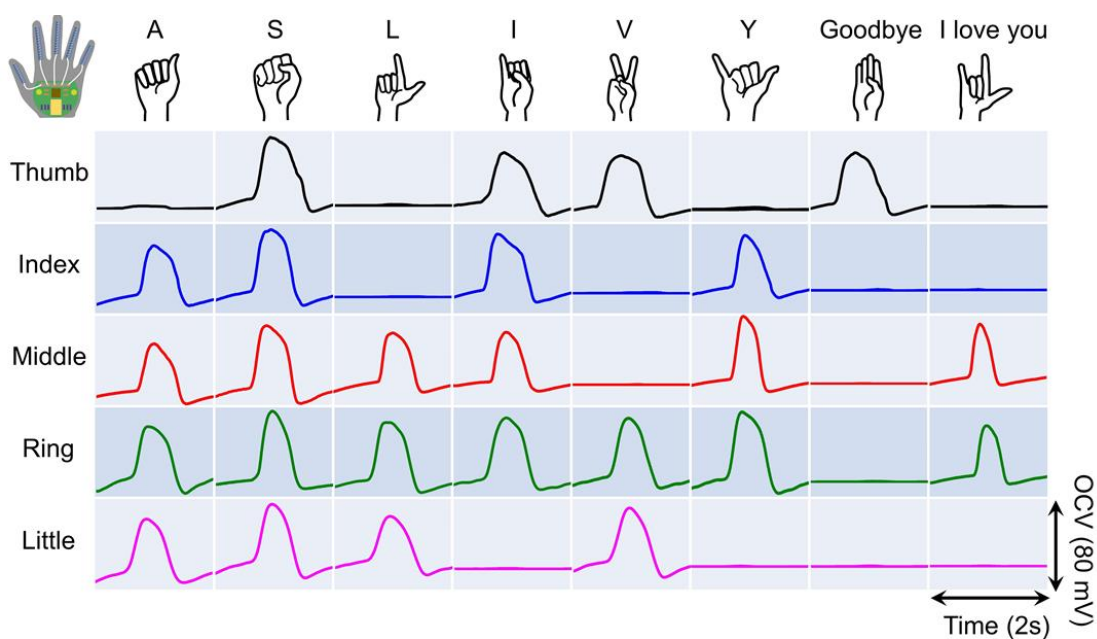
Figure S48. Illustrations of American Sign Language hand gestures, and the corresponding OCV profiles generated when the solid-state harvesters were woven into a glove.
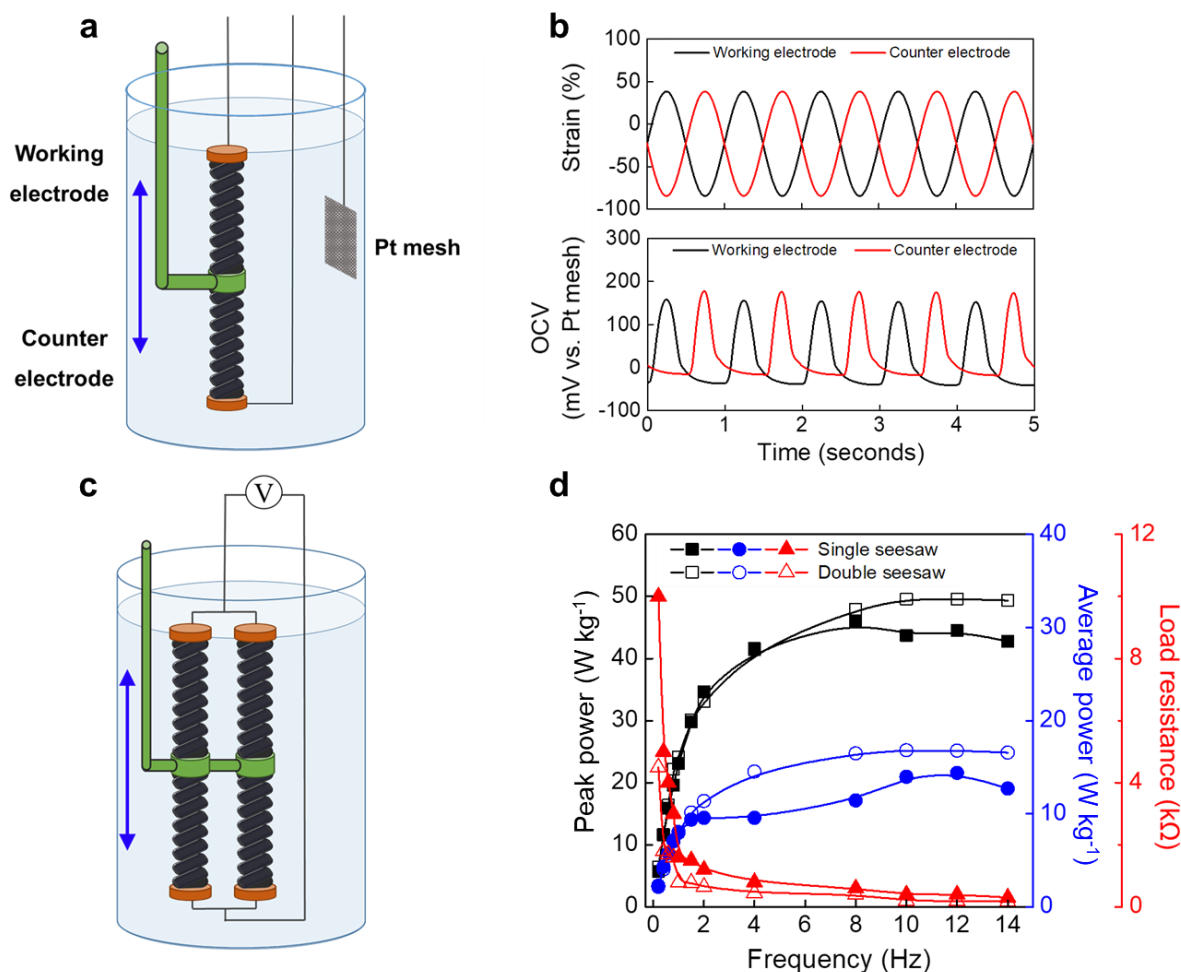
Figure S49. Dual-electrode, one-body harvester using a seesaw structure that is operated in 0.1 M aqueous HCl. a. Illustration of a one-stretched-body, two-electrode harvester that uses a seesaw structure to increase the output voltage compared to that for a harvester in which only one electrode is stretched. The weight of each of the pictured CNT electrodes was 101 μg and the length of each electrode was 10 mm. The Pt mesh electrode is used only for OCV measurements and not as an electrode for energy harvesting. **b.** The time dependence of applied strain and OCV (relative to the Pt mesh electrode) when the working electrode and the counter electrode are sinusoidally stretched 180° out-of-phase by using the seesaw structure. A total strain of 123% was applied. **c.** Illustration of two one-stretched-body harvesters that are operated in parallel using the seesaw structure. The two harvesters in the double seesaw structure are separated by 1 cm. **d.** The peak power, average power, and load resistance that maximizes the average power versus frequency for the single seesaw structure of (a) and the double seesaw structure of (c). A total strain of 61% was applied during harvesting for both structures.
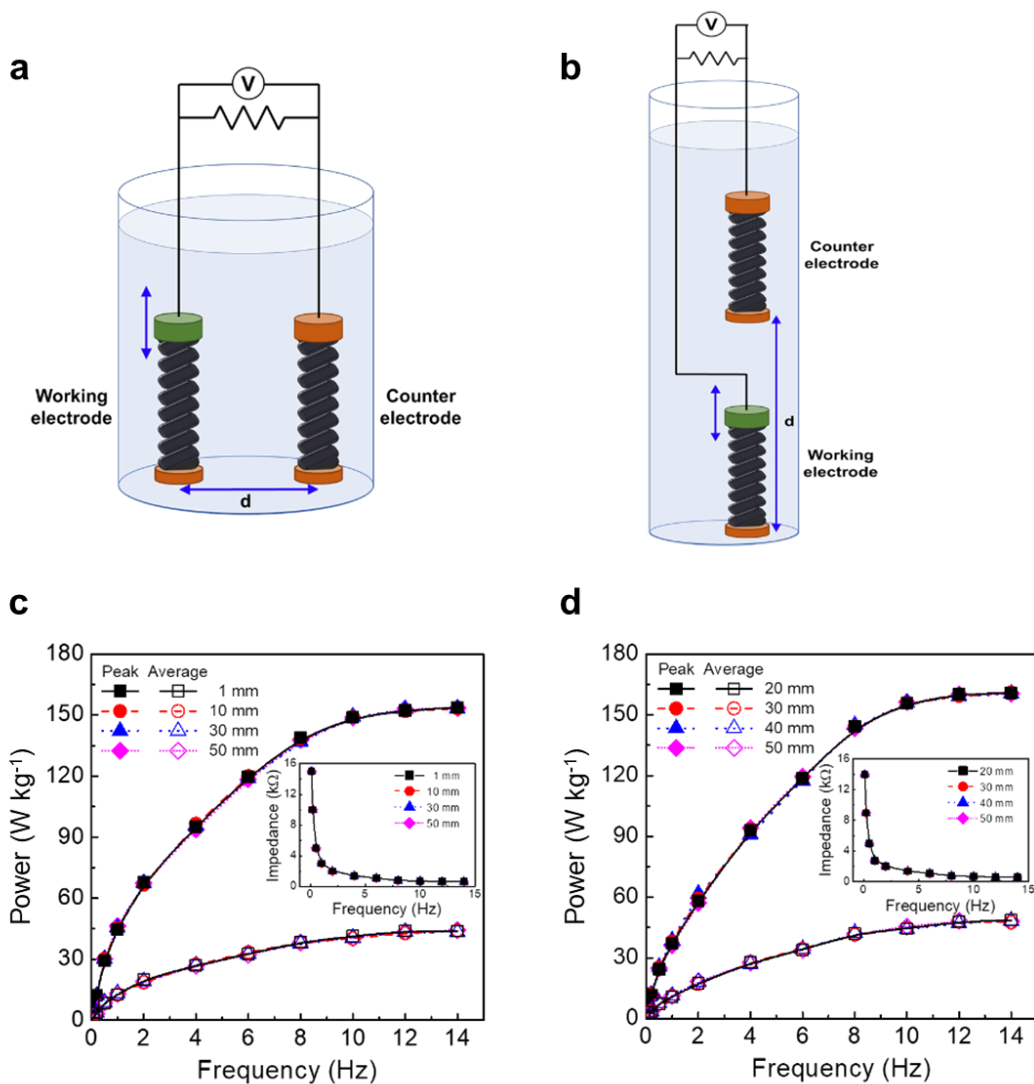
Figure S50. a-b. Illustration of the experiment for evaluating the possible dependence of the load-resistance-optimized peak and average power on the lateral (a) and longitudinal (b) separation between twistron working electrode and twistron counter electrode. These coiled TOP twistrons had identical structures, lengths (10 mm) and weights (66 µg) before only the working electrode was sinusoidally stretched to generate electrical energy. **c-d.** The frequency dependencies of the peak power (solid symbols) and the average power (open symbols) for a stretch to a total strain of 60% for different center-to-center lateral (c) and longitudinal (d) separations between the stretched twistron working electrode and the non-stretched twistron counter electrode. As indicated by the pictured superposition of data points for separations between 1 and 50 mm (lateral), and between 20 and 50 mm (longitudinal), identical values of peak power and average power were obtained at each frequency, independent of the separation between working and counter electrodes.
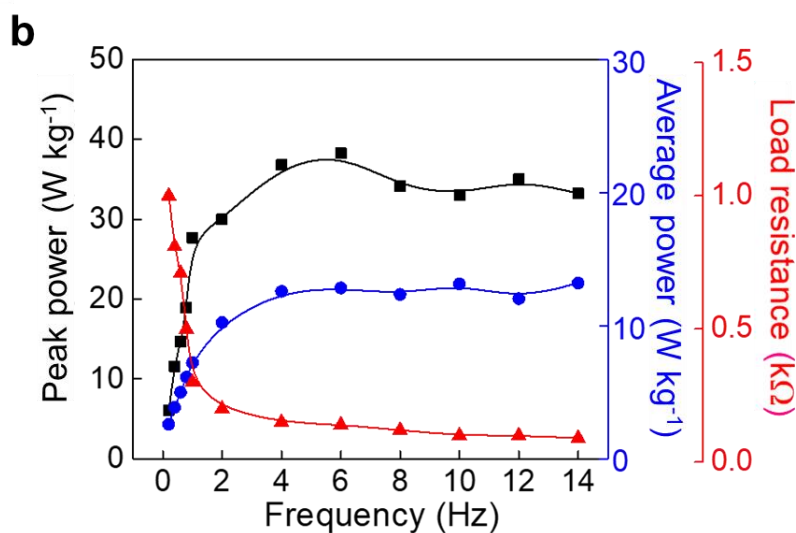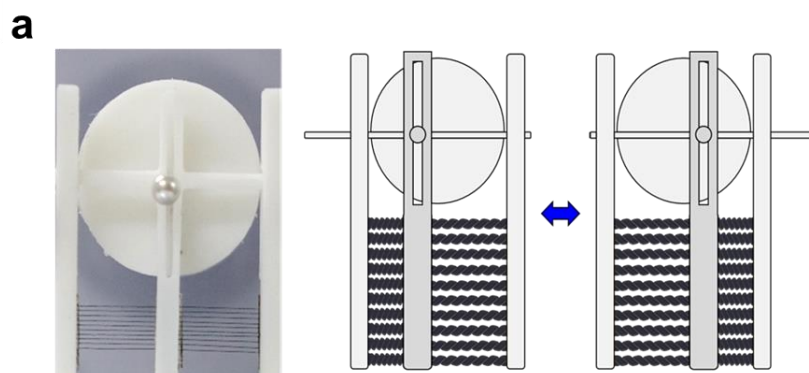
Figure S51. Use of a Scotch yoke structure for converting input rotational mechanical energy to the seesaw stretch of TOP twistrons in 0.1 M aqueous HCl. a. Photograph of a Scotch yoke structure and attached twistron electrodes that undergo seesaw-like tensile deformation during harvesting (left), and illustration of the extreme deformation states during a rotation (right). Ten equivalent, parallel-connected TOP twistrons were used for each electrode. The weight of each of single yarn in a CNT electrode was 42 μg and its length was 12 mm, so the total twistron weight in the harvester was 0.84 mg. **b.** The peak power, average power, and load resistance versus frequency for the harvester of (a) when a 20% tensile strain change was applied by the Scotch yoke structure.
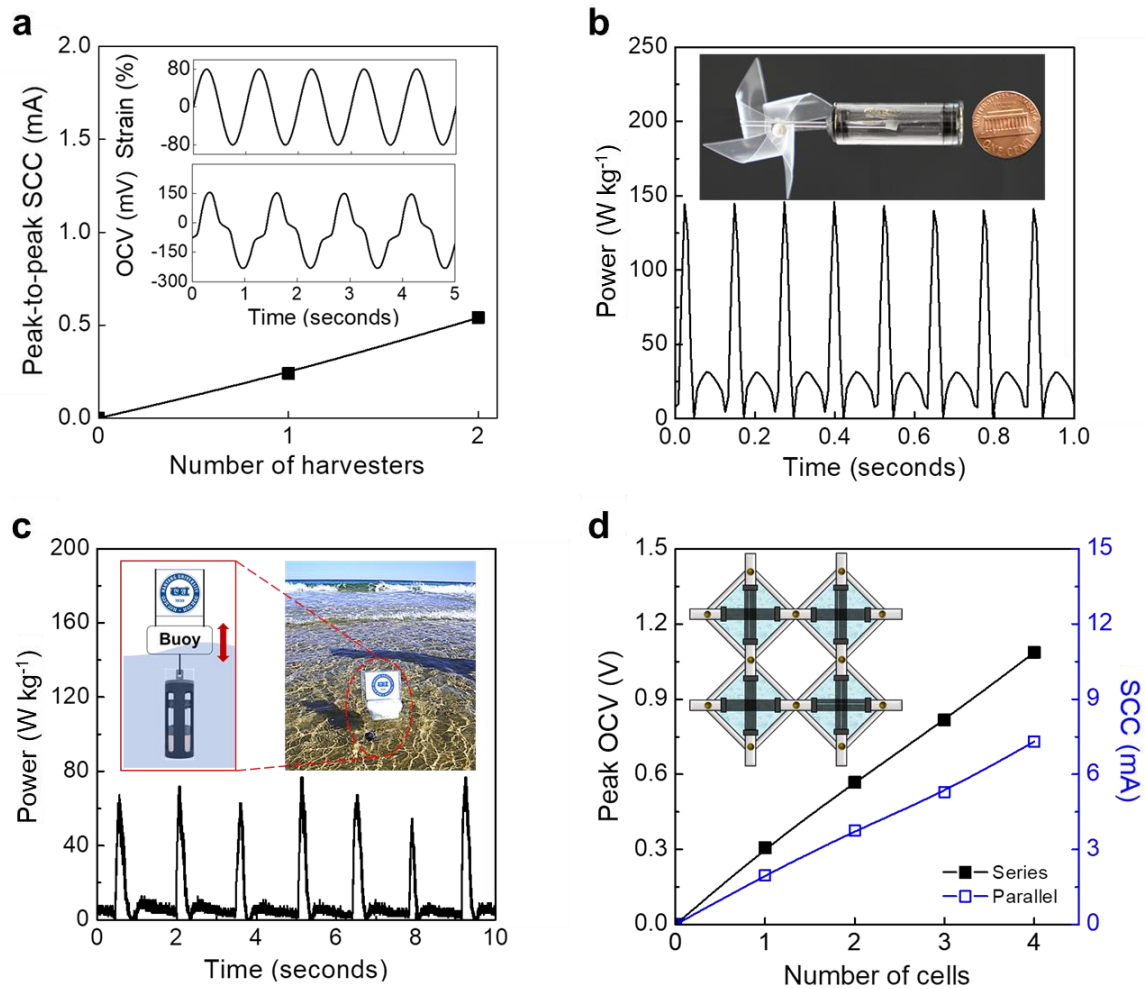
Figure S52. Application demonstrations for TOP CNT twistrons. a. The peak-to-peak SCC for a 1 Hz, ±80% strain for two parallel connected seesaw harvester yarns operated in 0.1 M aqueous HCl electrolyte. The inset shows the time dependence of the applied strain and the OCV of the interelectrode voltage of a one-body seesaw harvester. **b.** The time dependence of the gravimetric power generated by a wind-driven seesaw-structure CNT harvester that operated at 8 Hz in 0.1 M aqueous HCl, which is shown in the inset. **c.** The time dependence of the gravimetric power output of a 0.58-mg TOP coiled yarn, when operated as an ocean-wave harvester for ocean-wave frequencies of 0.5 to 1 Hz. The maximum stretch is mechanically limited to 50% in sea-water, which is the electrolyte for the twistrons. (Insets) A schematic illustration of the harvester and a photograph of it being used in shallow ocean water. **d.** The peak OCV and SCC during a 1 Hz, 35% sinusoidal strain for series (black squares) and parallel (blue open squares) connected wine-rack frame harvester cells. The wine-rack cells contain 0.1 M aqueous HCl electrolyte. (Inset) Illustration of wine-rack frame harvesters. Ten 1.7-cm-long twistrons, each weighting 80 μg, were placed parallel in the negative and positive compressibility directions of each of the four wine rack cells. The initial tensile strain for each twistron in the square configuration was 17.5%.
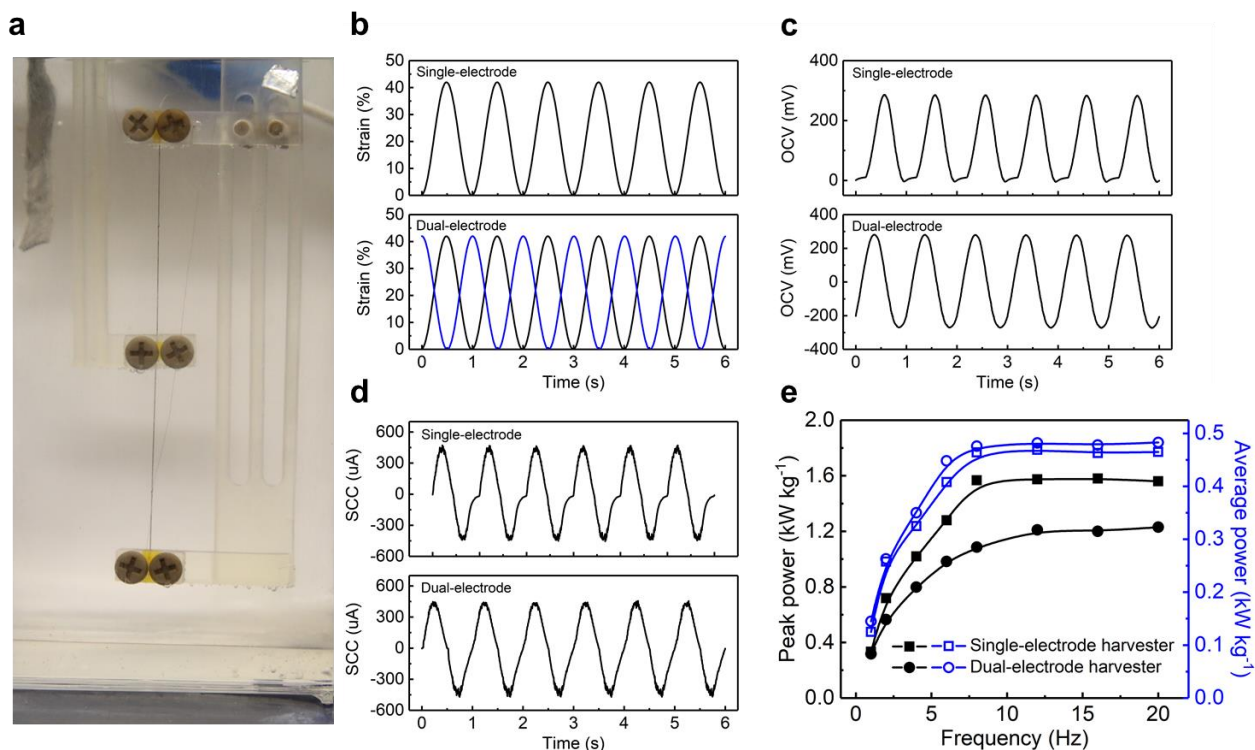
Figure S53. Comparison of energy harvesting in 0.1 M aqueous HCl by a rGO@CNT single-stretched-electrode twistron harvester with that for a dual-stretched-electrode harvester that uses a seesaw structure. a. An optical image of a dual-stretched-electrode harvester using the seesaw structure. The top harvester was pre-strained by 42%. The top and bottom twistrons were insulated, but mechanically connected in the center. Moving the center of the one-body harvester causes one twistron electrode to contract in length, while the other twistron yarn expands. **b-d.** The time dependencies of applied strain (b), generated OCV (c), and SCC (d) for the single-stretched-electrode and the dual-stretched-electrode harvesters. A non-deformed CNT-wrapped Pt mesh counter electrode was used for the single-stretched-electrode harvester, and the working electrode and counter electrode are sinusoidally stretched 180° out-of-phase by using the seesaw structure for dual-stretched-electrode harvester. **e.** The frequency dependencies of peak power and average power for the single-stretched-electrode harvester and for the dual-stretched-electrode harvester.
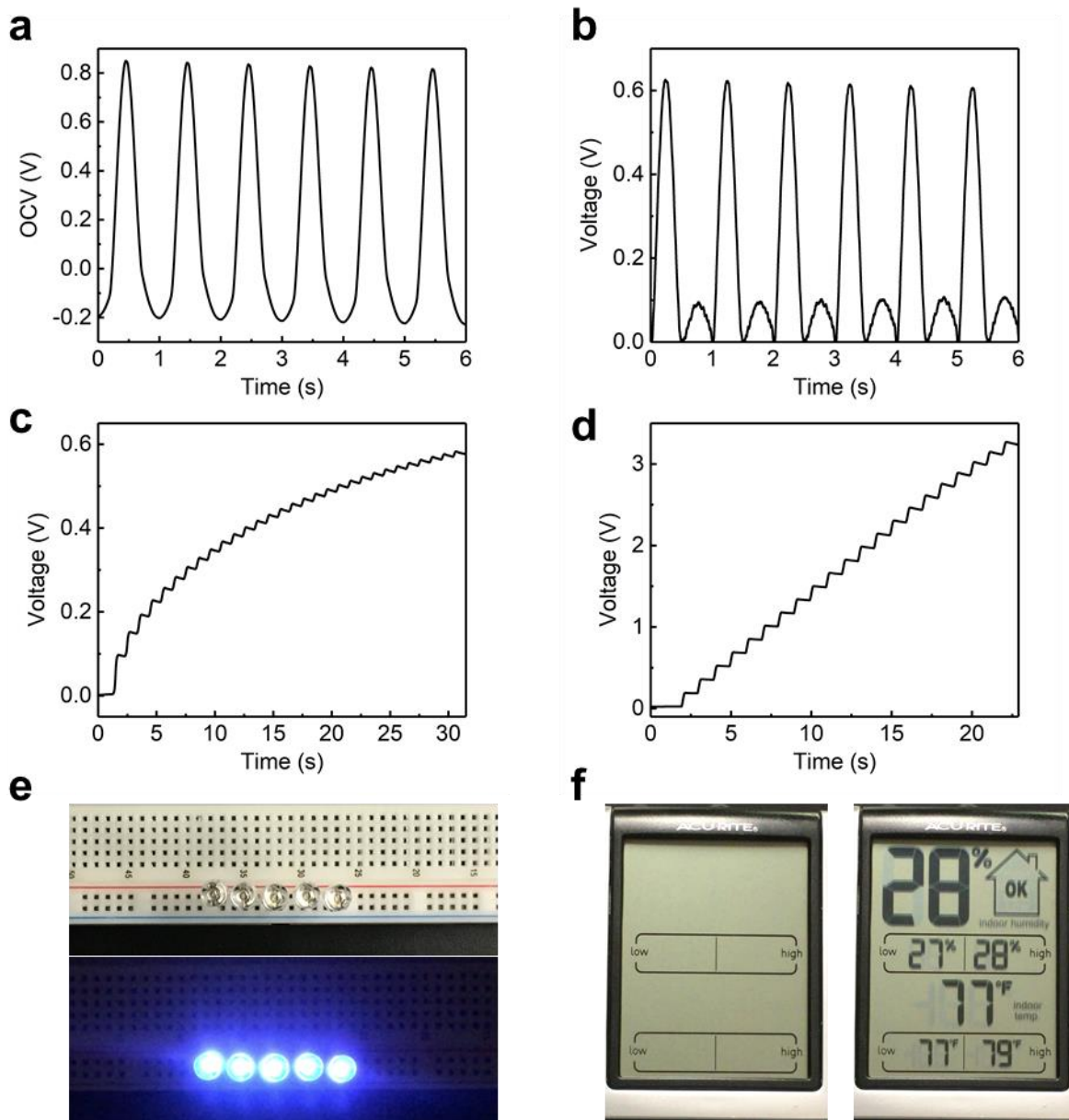
Figure S54. a. The time dependence of open-circuit voltage during a 1 Hz, 40% stretch for 4-series-connected coiled ITAP CNT harvesters. **b.** Rectified voltage output of (a) by using a Schottky diode full bridge rectifier. **c.** Charging a 220 µF capacitor to 0.6 V using the rectified voltage output in (b). **d.** Charging a 220 µF capacitor to 3.3 V by connecting the rectified voltage output in (b) to a self-powered LTC 3108 boost converter. **e-f.** Charged capacitors (1 mF, 3.3 V) were used to power LEDs (e) and temperature and humidity sensors (f).

Table S1.

Comparison of the performance of the present twistrons with that for prior-art twistrons and other solid-state mechanical energy harvesters. Peak power values for other mechanical energy harvesters were obtained directly from the references or calculated from presented data. When power is reported without indication of whether it is peak power or average power, it was assumed to be peak power. Literature references more frequently report peak power than average power. If peak power was not reported in the literature, we approximated in our previous table[2] that the peak power was two times the reported average power, which introduces considerable error.

Ref.	Harvester type	Harvester weight	Frequency	Peak power	Peak power/frequency
		(kg)	(Hz)	$(W\ kg^{-1})$	$(J\ kg^{-1}/cycle)$
This work	Twistron-rGO@CNT	$1.50\ 10^{-7}$	0.1	74	740
This work	Twistron-rGO@CNT	$1.50\ 10^{-7}$	0.25	196	784
This work	Twistron-rGO@CNT	$1.50\ 10^{-7}$	0.5	367	734
This work	Twistron-rGO@CNT	$1.50\ 10^{-7}$	1	730	730
This work	Twistron-rGO@CNT	$1.50\ 10^{-7}$	2	1050	525
This work	Twistron-rGO@CNT	$1.50\ 10^{-7}$	4	1441	360.25
This work	Twistron-rGO@CNT	$1.50\ 10^{-7}$	8	2105	263.13
This work	Twistron-rGO@CNT	$1.50\ 10^{-7}$	12	2431	202.58
This work	Twistron-rGO@CNT	$1.50\ 10^{-7}$	16	2990	186.88
This work	Twistron-rGO@CNT	$1.50\ 10^{-7}$	20	3218	160.9
This work	Twistron-rGO@CNT	$1.50\ 10^{-7}$	24	3154	131.42
This work	Twistron-rGO@CNT	$1.50\ 10^{-7}$	30	3195	106.5

2	Twistron-CNT	$2.00 \ 10^{-7}$	1.25	50	40
2	Twistron-CNT	$2.00 \ 10^{-7}$	6	150	25
2	Twistron-CNT	$2.00 \ 10^{-7}$	10	200	20
2	Twistron-CNT	$2.00 \ 10^{-7}$	30	250	8.33
17	Piezoelectric	$1.95 \ 10^{-5}$	0.3	60.9	203
18	Piezoelectric	$1.27 \ 10^{-14}$	0.5	4.37	8.74
19	Piezoelectric	$2.71 \ 10^{-2}$	30	1.94	$6.46 \ 10^{-2}$
20	Piezoelectric	$5.00 \ 10^{-4}$	0.4	0.5	1.25
21	Piezoelectric	$4.00 \ 10^{-3}$	600	0.23	$3.83 \ 10^{-4}$
22	Piezoelectric	$9.52 \ 10^{-3}$	30	$9.5 \ 10^{-2}$	$3.15 \ 10^{-3}$
23	Piezoelectric	$9.56 \ 10^{-4}$	0.3	$1.5 \ 10^{-2}$	$5.00 \ 10^{-2}$
24	Piezoelectric	$1.98 \ 10^{-16}$	0.7	$1.25 \ 10^{-2}$	$1.78 \ 10^{-2}$
25	Piezoelectric	$4.00 \ 10^{-3}$	147	1.42	$9.63 \ 10^{-3}$
26	Piezoelectric	$1.04 \ 10^{-2}$	52	0.97	$1.86 \ 10^{-2}$
27	Piezoelectric	$5.92 \ 10^{-7}$	3	11.4	3.80
28	Piezoelectric	$2.60 \ 10^{-5}$	263	$5.77 \ 10^{-3}$	$2.19 \ 10^{-5}$
28	Piezoelectric	$2.17 \ 10^{-4}$	80.1	$3.59 \ 10^{-3}$	$4.49 \ 10^{-5}$
29	Piezoelectric	$1.00 \ 10^{-6}$	461.2	2.15	$4.66 \ 10^{-3}$
30	Piezoelectric	$4.60 \ 10^{-3}$	10	$2.2 \ 10^{-2}$	$2.20 \ 10^{-3}$
31	Piezoelectric	$2.30 \ 10^{-5}$	36	$3.91 \ 10^{-3}$	$1.09 \ 10^{-4}$
32	Piezoelectric	$1.17 \ 10^{-2}$	398	$4.52 \ 10^{-3}$	$1.14 \ 10^{-5}$
33	Piezoelectric	$4.22 \ 10^{-4}$	1	33.18	33.18
34	Piezoelectric	$1.81 \ 10^{-4}$	60	53.6	0.89
35	Piezoelectric		13	$6.18 \ 10^{-2}$	$4.75 \ 10^{-3}$

36	Electrostatic	$1.04 \ 10^{-1}$	50	$1.01 \ 10^{-2}$	$2.02 \ 10^{-4}$
37	Electrostatic	$5.80 \ 10^{-3}$	2	$6.90 \ 10^{-3}$	$3.45 \ 10^{-3}$
38	Electrostatic	$1.92 \ 10^{-6}$	0.2	$2.82 \ 10^{-4}$	$1.41 \ 10^{-3}$
39	Electrostatic	$6.60 \ 10^{-5}$	150	$3.3 \ 10^{-2}$	$2.22 \ 10^{-4}$
40	Electrostatic	$6.60 \ 10^{-5}$	109	$1.97 \ 10^{-2}$	$1.81 \ 10^{-4}$
41	Electrostatic	$1.00 \ 10^{-4}$	63	$1.00 \ 10^{-2}$	$1.59 \ 10^{-4}$
42	Electrostatic	$5.00 \ 10^{-4}$	28	$3.00 \ 10^{-3}$	$1.07 \ 10^{-4}$
43	Electrostatic	$2.00 \ 10^{-5}$	95	$4.75 \ 10^{-2}$	$5.00 \ 10^{-4}$
44	Electrostatic	$8.80 \ 10^{-5}$	139	0.61	$4.41 \ 10^{-3}$
45	Electrostatic	$1.04 \ 10^{-4}$	136	$5.35 \ 10^{-2}$	$3.93 \ 10^{-4}$
46	Triboelectric	$8.80 \ 10^{-4}$	1	265	265
47	Triboelectric	$2.60 \ 10^{-4}$	0.33	7.44	22.60
48	Triboelectric	$7.00 \ 10^{-3}$	10	0.6	0.006
49	Triboelectric	$6.51 \ 10^{-4}$	3	0.35	0.12
50	Triboelectric	$5.33 \ 10^{-2}$	10	$2.63 \ 10^{-3}$	$2.63 \ 10^{-4}$
51	Triboelectric	$1.00 \ 10^{-4}$	5	0.28	$5.60 \ 10^{-2}$
52	Triboelectric	$2.54 \ 10^{-2}$	4	1.86	0.47
53	Triboelectric	$5.59 \ 10^{-4}$	0.5	8.94	17.88
54	Triboelectric	$2.69 \ 10^{-4}$	1.5	0.16	0.11
55	Triboelectric	0.05	1.25	0.24	0.192
56	Triboelectric		3.3	2.21	0.67
57	Triboelectric	$3.85 \ 10^{-3}$	1.5	1.17	0.78
58	Triboelectric	$8.78 \ 10^{-5}$	4.5	42.02	9.34
59	Triboelectric	$1.27 \ 10^{-1}$	1	0.131	0.131

60	Triboelectric	8.50×10^{-2}	3.83	5.67×10^{-2}	1.48×10^{-2}
61	Triboelectric	1.44×10^{-3}	1.43	11.64	8.14
62	Triboelectric	4.06×10^{-1}	30	1.6×10^{-2}	5.33×10^{-4}
63	Triboelectric	1.29×10^{-2}	10	1.55×10^{-2}	1.55×10^{-3}
64	Triboelectric	3.20×10^{-3}	34	0.84	2.47×10^{-2}
65	Triboelectric	0.20	1	0.18	0.18
66	Triboelectric	1.94×10^{-3}	6.67	8.08	1.21
67	Triboelectric	6.02×10^{-1}	1	1.83×10^{-2}	1.83×10^{-2}
68	Triboelectric	3.70×10^{-2}	2	1.07×10^{-2}	5.37×10^{-3}
69	Triboelectric	1.57×10^{-2}	2.5	5.17	2.068
70	Dielectric Elastomer	4.00×10^{-2}	0.3	40.5	135
71	Dielectric Elastomer	3.20×10^{-4}	1.6	11.3	7.06
72	Dielectric Elastomer		2	0.78	0.39
73	Dielectric Elastomer	4.40×10^{-3}	0.7	197	281.43
74	Dielectric Elastomer		0.1	13	130
75	Dielectric Elastomer		0.25	16.3	65.2

Table S2.

Comparison of the performance of the present twistrons with that for prior-art twistrons and other solid-state mechanical energy harvesters. Average power values for other mechanical energy harvesters were obtained directly from the references or calculated from presented data.

Ref.	Harvester type	Harvester weight (kg)	Frequency (Hz)	Average power (W kg^{-1})	Average power/frequency (J kg^{-1}/cycle)
This work	Twistron-rGO@CNT	$1.50\ 10^{-7}$	0.1	30	300
This work	Twistron-rGO@CNT	$1.50\ 10^{-7}$	0.25	76	304
This work	Twistron-rGO@CNT	$1.50\ 10^{-7}$	0.5	142	284
This work	Twistron-rGO@CNT	$1.50\ 10^{-7}$	1	270	270
This work	Twistron-rGO@CNT	$1.50\ 10^{-7}$	2	370.5	185.25
This work	Twistron-rGO@CNT	$1.50\ 10^{-7}$	4	503	125.75
This work	Twistron-rGO@CNT	$1.50\ 10^{-7}$	8	642	80.25
This work	Twistron-rGO@CNT	$1.50\ 10^{-7}$	12	724	60.33
This work	Twistron-rGO@CNT	$1.50\ 10^{-7}$	16	847	53
This work	Twistron-rGO@CNT	$1.50\ 10^{-7}$	20	850	42.5
This work	Twistron-rGO@CNT	$1.50\ 10^{-7}$	24	859	35.8
This work	Twistron-rGO@CNT	$1.50\ 10^{-7}$	30	858	28.6
2	Twistron-CNT	$2.00\ 10^{-7}$	1.25	16.25	13
2	Twistron-CNT	$2.00\ 10^{-7}$	6	36	6.0
2	Twistron-CNT	$2.00\ 10^{-7}$	10	50	5.0
2	Twistron-CNT	$2.00\ 10^{-7}$	30	60	2.0
76	Piezoelectric	$7.71\ 10^{-2}$	9	0.115	$1.28\ 10^{-2}$
77	Piezoelectric	$3.39\ 10^{-3}$	68.1	$1.7\ 10^{-2}$	$2.49\ 10^{-4}$
78	Piezoelectric	$3.53\ 10^{-16}$	1	$1.21\ 10^{-4}$	$1.21\ 10^{-4}$

79	Electrostatic	$5.00 \ 10^{-3}$	50	$0.71 \ 10^{-2}$	$1.42 \ 10^{-4}$
80	Electrostatic	$6.00 \ 10^{-5}$	180	$2.71 \ 10^{-4}$	$1.51 \ 10^{-6}$
81	Triboelectric	$1.58 \ 10^{-3}$	5	29.5	11.70
82	Triboelectric		5	$7.00 \ 10^{-2}$	$1.40 \ 10^{-2}$
82	Triboelectric		3	$5.70 \ 10^{-2}$	$1.90 \ 10^{-2}$
82	Triboelectric		2	$5.50 \ 10^{-2}$	$2.75 \ 10^{-2}$
82	Triboelectric		1.5	$4.00 \ 10^{-2}$	$2.67 \ 10^{-2}$
82	Triboelectric		1	$3.70 \ 10^{-2}$	$3.70 \ 10^{-2}$
82	Triboelectric		0.8	$3.00 \ 10^{-2}$	$3.75 \ 10^{-2}$
82	Triboelectric		0.5	$1.8 \ 10^{-2}$	$3.60 \ 10^{-2}$
82	Triboelectric		0.3	$1.06 \ 10^{-2}$	$3.53 \ 10^{-2}$
82	Triboelectric		0.1	$3.00 \ 10^{-3}$	$3.00 \ 10^{-2}$
83	Triboelectric		3	$1.1 \ 10^{-2}$	$3.67 \ 10^{-3}$
84	Dielectric Elastomer	$6.00 \ 10^{-4}$	0.5	280	560
85	Dielectric Elastomer	$6.00 \ 10^{-4}$	0.22	170	772.73
86	Dielectric Elastomer	$3.50 \ 10^{-4}$	3	18.9	12.6
87	Dielectric Elastomer	$4.83 \ 10^{-5}$	1	6	6
71	Dielectric Elastomer	$3.20 \ 10^{-4}$	1.6	5.65	3.53
88	Dielectric Elastomer	$1.53 \ 10^{-3}$	0.17	17	102
89	Dielectric Elastomer		0.54	200	370

References

1. Zhang, M. et al. Strong, transparent, multifunctional, carbon nanotube sheets. *Science* **309**, 1215-1219 (2005).
2. Kim, S. H. et al. Harvesting electrical energy from carbon nanotube yarn twist. *Science* **357**, 773-778 (2017).
3. Di, J. et al. Strong, twist-stable carbon nanotube yarns and muscles by tension annealing at extreme temperatures. *Adv. Mater.* **28**, 6598-6605 (2016).
4. Lima, M. D. et al. Biscrolling nanotube sheets and functional guests into yarns. *Science* **331**, 51-55 (2011).
5. Martinez, P. M. et al. Silver nanowires on carbon nanotube aerogel sheets for flexible, transparent electrodes. *ACS Appl. Mater. Interfaces* **11**, 32235-32243 (2019).
6. Jalili, R. et al. Scalable one-step wet-spinning of graphene fibers and yarns from liquid crystalline dispersions of graphene oxide: towards multifunctional textiles. *Adv. Funct. Mater.* **23**, 5345-5354 (2013).
7. Ilavsky, J. *Nika*: software for two-dimensional data reduction. *J. Appl. Cryst.* **45**, 324-328 (2012).
8. Toby, B. H. & Von Dreele, R. B. *GSAS-II*: the genesis of a modern open-source all purpose crystallography software package. *J. Appl. Cryst.* **46**, 544-549 (2013).
9. Bandley, E., Greenhalgh, E., Shaffer, M. & Li. Q. Mapping carbon nanotube orientation by fast Fourier transform of scanning electron micrographs. *Carbon* **137**, 78-87 (2018).
10. Vainio, U. et al. Orientation distribution of vertically aligned multiwalled carbon nanotubes. *J. Phys. Chem. C* **118**, 9507-9513 (2014).
11. Qiao, J. et al. Large-stroke electrochemical carbon nanotube/graphene hybrid yarn muscles. *Small* **14**, 1801883 (2018).
12. Malik, R. et al. *Nanotube Superfiber Materials Ch. 13* (William Andrew Publishing, 2014).
13. Shan, B. & Cho, K. First-principles study of work functions of double-wall carbon nanotubes. *Phys. Rev. B* **73**, 081401 (2006).
14. Chu, H. et al. Unipolar-stroke, electroosmotic-pump carbon nanotube yarn muscles. *Science* **371**, 494-498 (2021).
15. Salto, Y., Yoshikawa, T. , Bandow, S., Tomita, M. & Hayashi, T. Interlayer spacings in carbon nanotubes. *Phys. Rev. B* **48**, 1907 (1993).
16. Grimme, S., Antony, J., Ehrlich, S. & Krieg, H. A consistent and accurate *ab initio* parametrization of density functional dispersion correction (DFT-D) for the 94 elements H-Pu. *J. Chem. Phys.* **132**, 154104 (2010).
17. Hwang, G. T. et al. Self-powered cardiac pacemaker enabled by flexible single crystalline PMN-PT piezoelectric energy harvester. *Adv. Mater.* **26**, 4880-4887 (2014).
18. Wu, W. et al. Piezoelectricity of single-atomic-layer MoS2 for energy conversion and Piezotronics. *Nature* **514**, 470-474 (2014).
19. Cho, K. H. et al. Structure–performance relationships for cantilever-type piezoelectric energy harvesters. *J. Appl. Phys.* **115**, 204108 (2014).
20. Hwang, G. T. et al. Self-powered wireless sensor node enabled by an aerosol-deposited pzt flexible energy harvester. *Adv. Energy Mater.* **6**, 1600237 (2016).
21. https://www.cornestech.co.jp/images/uploads/file/products/pdf/bolt.pdf.
22. Sodano, H. A., Park, G. & Inman, D. J. Estimation of electric charge output for piezoelectric

energy harvesting. *Strain* **40**, 49-58 (2004).

23. Jeong, C. K. et al. Nanogenerators: large-area and flexible lead-free nanocomposite generator using alkaline niobate particles and metal nanorod filler. *Adv. Funct. Mater.* **24**, 2620-2629 (2014).

24. Hu, Y. et al. A nanogenerator for energy harvesting from a rotating tire and its application as a self-powered pressure/speed sensor. *Adv. Mater.* **23**, 4068-4071 (2011).

25. http://info.mide.com/piezo-products/download-piezo-products-datasheets.

26. www.piezo.com/catalog8.pdf%20files/Cat8.20&21.pdf.

27. Siddiqui, S. et al. High-performance flexible lead-free nanocomposite piezoelectric nanogenerator for biomechanical energy harvesting and storage. *Nano Energy* **15**, 177-185 (2015).

28. Aktakka, E. E., Peterson, R. L. & Najafi, K. A CMOS-compatible piezoelectric vibration energy scavenger based on the integration of bulk PZT films on silicon. in *2010 International Electron Devices Meeting* (IEEE 2010), pp. 31-5.

29. Shen, D. et al. The design, fabrication and evaluation of a MEMS PZT cantilever with an integrated Si proof mass for vibration energy harvesting. *J. Micromech. Microeng.* **18**, 055017 (2008).

30. Tang, Q. C., Yang, Y. L. & Li, X. Bi-stable frequency up-conversion piezoelectric energy harvester driven by non-contact magnetic repulsion. *Smart Mater. Struct.* **20**, 125011 (2011).

31. Liu, H. et al. Piezoelectric mems energy harvester for low-frequency vibrations with wideband operation range and steadily increased output power. *J. Microelectromech. Syst.* **20**, 1131-1142 (2011).

32. Aktakka, E. E. & Najafi, K. Three-axis piezoelectric vibration energy harvester. in *2015 28th IEEE International Conference on Micro Electro Mechanical Systems (MEMS)* (IEEE, 2015), pp. 1141-1144.

33. Gao, X. et al. Giant piezoelectric coefficients in relaxor piezoelectric ceramic PNN-PZT for vibration energy harvesting. *Adv. Funct. Mater.* **28**, 1706895 (2018).

34. Kang, M. G. et al. High power magnetic field energy harvesting through amplified magneto-mechanical vibration. *Adv. Energy Mater.* **8**, 1703313 (2018).

35. Fu, J. et al. Flexible piezoelectric energy harvester with extremely high power generation capability by sandwich structure design strategy. *ACS Appl. Mater. Interfaces* **12**, 9766-9774 (2020).

36. Basrour, S. et al. Fabrication and characterization of high damping electrostatic micro devices for vibration energy scavenging. in *Symposium on Design, Test, Integration and Packaging of MEMS and MOEMS*, 386-390 (2015).

37. Naruse, Y. et al. Electrostatic micro power generation from low-frequency vibration such as human motion. *J. Micromech. Microeng.* **19**, 094002 (2009).

38. Yu, X. et al. A novel photoelectric conversion yarn by integrating photomechanical actuation and the electrostatic effect. *Adv. Mater.* **28**, 10744-10749 (2016).

39. Guilllemet, R. et al. Wideband MEMS electrostatic vibration energy harvesters based on gap-closing interdigited combs with a trapezoidal cross section. in *2013 IEEE 26th International Conference on Micro Electro Mechanical Systems (MEMS)* (IEEE 2013), pp. 817-820.

40. Cottone, F. et al. Non-linear MEMS electrostatic kinetic energy harvester with a tunable multistable potential for stochastic vibrations. in *2013 Transducers & Eurosensors XXVII: The 17th International Conference on Solid-State Sensors, Actuators and Microsystems*

(TRANSDUCERS & EUROSENSORS XXVII) (IEEE 2013), pp. 1336-1339.

41. Suzuki, Y. et al. A MEMS electret generator with electrostatic levitation for vibration-driven energy-harvesting applications. *J. Micromech. Microeng.* **20**, 104002 (2010).

42. Minakawa, Y., Chen, R. & Suzuki, Y. X-shaped-spring enhanced MEMS electret generator for energy harvesting. in *2013 Transducers & Eurosensors XXVII: The 17th International Conference on Solid-State Sensors, Actuators and Microsystems (TRANSDUCERS & EUROSENSORS XXVII)* (IEEE 2013), pp. 2241-2244.

43. Tao, K. Out-of-plane electret-based MEMS energy harvester with the combined nonlinear effect from electrostatic force and a mechanical elastic stopper. *J. Micromech. Microeng.* **25**, 104014 (2015).

44. Asanuma, H. et al. Nonlinear restoring force of spring with stopper for ferroelectric dipole electret-based electrostatic vibration energy harvesters. *AIP Adv.* **6**, 075206 (2016).

45. Zhang, Y. et al. Micro electrostatic energy harvester with both broad bandwidth and high normalized power density. *Appl. Energy* **212**, 362-371 (2018).

46. Kim, D. et al. High-performance nanopattern triboelectric generator by block copolymer lithography. *Nano Energy* **12**, 331-338 (2015).

47. Fan, F. R., Tian, Z. Q. & Wang, Z. L. Flexible triboelectric generator. *Nano Energy* **1**, 328-334 (2012).

48. Bai, P. et al. Integrated multilayered triboelectric nanogenerator for harvesting biomechanical energy from human motions. *ACS Nano* **7**, 3713-3719 (2013).

49. Zhong, J. et al. Finger typing driven triboelectric nanogenerator and its use for instantaneously lighting up LEDs. *Nano Energy* **2**, 491-497 (2013).

50. Zhang, C. et al. Theoretical comparison, equivalent transformation, and conjunction operations of electromagnetic induction generator and triboelectric nanogenerator for harvesting mechanical energy. *Adv. Mater.* **26**, 3580-3591 (2014).

51. Li, T. et al. Lightweight triboelectric nanogenerator for energy harvesting and sensing tiny mechanical motion. *Adv. Funct. Mater.* **26**, 4370-4376 (2016).

52. Gao, S. et al. Triboelectric nanogenerator powered electrochemical degradation of organic pollutant using Pt-free carbon materials. *ACS Nano* **11**, 3965-3972 (2017).

53. Guo, H. et al. Self-sterilized flexible single-electrode triboelectric nanogenerator for energy harvesting and dynamic force sensing. *ACS Nano* **11**, 856-864 (2017).

54. Pu, X. et al. Ultrastretchable, transparent triboelectric nanogenerator as electronic skin for biomechanical energy harvesting and tactile sensing. *Sci. Adv.* **3**, e1700015 (2017).

55. Zhang, Z. et al. Facile method and novel dielectric material using a nanoparticle-doped thermoplastic elastomer composite fabric for triboelectric nanogenerator applications. *ACS Appl. Mater. Interfaces* **10**, 13082-13091 (2018).

56. Gong, J. et al. Towards truly wearable energy harvesters with full structural integrity of fiber materials. *Nano Energy* **58**, 365-374 (2019).

57. Zhang, Z. et al. Comprehensive dependence of triboelectric nanogenerator on dielectric thickness and external impact for high electric outputs. *J. Appl. Phys.* **124**, 045106 (2018).

58. Salauddin, M. et al. A novel MXene/ecoflex nanocomposite-coated fabric as a highly negative and stable friction layer for high-output triboelectric nanogenerators. *Adv. Energy Mater.* **11**, 2002832 (2021).

59. Liang, X. et al. Spherical triboelectric nanogenerator based on spring-assisted swing structure

for effective water wave energy harvesting. *Nano Energy* **83**, 105836 (2021).

60. Liu, S. et al., Magnetic switch structured triboelectric nanogenerator for continuous and regular harvesting of wind energy. *Nano Energy* **83**, 105851 (2021).
61. Wang, H. L. et al. Boosting the power and lowering the impedance of triboelectric nanogenerators through manipulating the permittivity for wearable energy harvesting. *ACS Nano* **15**, 7513-7521 (2021).
62. Wang, Y. et al. Gravity triboelectric nanogenerator for the steady harvesting of natural wind energy. *Nano Energy* **82**, 105740 (2021).
63. Gao, Y. et al. A robust rolling-mode direct-current triboelectric nanogenerator arising from electrostatic breakdown effect. *Nano Energy* **85**, 106014 (2021).
64. Ye, C. et al. A triboelectric–electromagnetic hybrid nanogenerator with broadband working range for wind energy harvesting and a self-powered wind speed sensor. *ACS Energy Lett.* **6**, 1443-1452 (2021).
65. Zhang, C. et al. Bifilar-pendulum-assisted multilayer-structured triboelectric nanogenerators for wave energy harvesting. *Adv. Energy Mater.* **11**, 2003616 (2021).
66. Jin, L. et al. Free-fixed rotational triboelectric nanogenerator for self-powered real-time wheel monitoring. *Adv. Mater. Technol.* **6**, 2000918 (2021).
67. Yang, Y. et al. Triboelectric nanogenerator with double rocker structure design for ultra-low-frequency wave full-stroke energy harvesting. *Extreme Mech. Lett.* **46**, 101338 (2021).
68. Jiang, B. et al. A stretchable, harsh condition-resistant and ambient-stable hydrogel and its applications in triboelectric nanogenerator. *Nano Energy* **86**, 106086 (2021).
69. Li, Y. et al. Improved output performance of triboelectric nanogenerator by fast accumulation process of surface charges. *Adv. Energy Mater.* **11**, 2100050 (2021).
70. Waki, M. et al Electric power from artificial muscles. in *OCEANS 2008 - MTS/IEEE Kobe Techno-Ocean* (IEEE 2008), pp. 1-3.
71. McKay, T. G. et al. Dielectric elastomer generators that stack up. *Smart Mater. Struct.* **24**, 015014 (2014).
72. Vu-Cong, T., Jean-Mistral, C. & Sylvestre, A. Electrets substituting external bias voltage in dielectric elastomer generators: application to human motion. *Smart Mater. Struct.* **22**, 025012 (2013).
73. Moretti, G. et al. Resonant wave energy harvester based on dielectric elastomer generator. *Smart Mater. Struct.* **27**, 035015 (2018).
74. Jiang, Y. et al. Optimizing energy harvesting performance of cone dielectric elastomer generator based on VHB elastomer. *Nano Energy* **71**, 104606 (2020).
75. Song, Z. Q. et al. Dielectric elastomer generator with diaphragm configuration. *MATEC Web Conf.* **192**, 01032 (2018).
76. Kim, K. B. et al. Performance of unimorph cantilever generator using Cr/Nb doped $Pb(Zr_{0.54}Ti_{0.46})O_3$ thick film for energy harvesting device applications. *J. Eur. Ceram. Soc.* **33**, 305-311(2013).
77. Sharpes, N., Abdelkefi, A. & Priya, S. Two-dimensional concentrated-stress low-frequency piezoelectric vibration energy harvesters. *Appl. Phys. Lett.* **107**, 093901 (2015).
78. Hinchet, R. et al. Performance optimization of vertical nanowire-based piezoelectric nanogenerators. *Adv. Funct. Mater.* **24**, 971-977 (2014).
79. Boisseau, S. et al. Cantilever-based electret energy harvesters. *Smart Mater. Struct.* **20**,

105013 (2011).

80. Crovetto, A., Wang, F. & Hansen, O. An electret-based energy harvesting device with a

    wafer-level fabrication process. *J. Micromech. Microeng.* **23**, 114010 (2013).

81. Jung, W. S. et al. High output piezo/triboelectric hybrid generator. *Sci. Rep.* **5**, 9309 (2015).

82. Zi, Y. et al. Harvesting low-frequency (<5 hz) irregular mechanical energy: a possible killer application of triboelectric nanogenerator. *ACS Nano* **10**, 4797-4805 (2016).

83. Dong, K. et al. Versatile core–sheath yarn for sustainable biomechanical energy harvesting and real-time human-interactive sensing. *Adv. Energy Mater.* **8**, 1801114 (2018).

84. Huang, J. et al. Maximizing the energy density of dielectric elastomer generators using equi-biaxial loading. *Adv. Funct. Mater.* **23**, 5056-5061 (2013).

85. Shian, S. et al. Optimizing the electrical energy conversion cycle of dielectric elastomer generators. *Adv. Mater.* **26**, 6617-6621 (2014).

86. McKay, T. et al. An integrated, self-priming dielectric elastomer generator. *Appl. Phys. Lett.* **97**, 062911 (2010).

87. Jean-Mistral, C., Vu Cong, T. & Sylvestre, A. Advances for dielectric elastomer generators: replacement of high voltage supply by electret. *Appl. Phys. Lett.* **101**, 162901 (2012).

88. Kaltseis, R. et al. Method for measuring energy generation and efficiency of dielectric elastomer generators. *Appl. Phys. Lett.* **99**, 162904 (2011).

89. Kaltseis, R. et al. Natural rubber for sustainable high-power electrical energy generation. *RSC Adv.* **4**, 27905-27913 (2014).